Impedance Spectroscopy Techniques for Condition Monitoring of Polymer Electrolyte Membrane Fuel Cells

Prepared By

FABUSUYI AKINDELE AROGE

Department of Electrical Engineering

University of Cape Town

October 2018

Submitted to the Department of Electrical Engineering at the University of Cape Town in partial fulfilment of the academic requirements for a Master of Science degree in **ELECTRICAL ENGINEERING**

Declaration

I know the meaning of plagiarism and declare that all the work in the document, save for that which is properly acknowledged, is my own. This thesis/dissertation has been submitted to the Turnitin module (or equivalent similarity and originality checking software) and I confirm that my supervisor has seen my report and any concerns revealed by such have been resolved with my supervisor.

FABUSUYI AKINDELE AROGE

Signed by candidate

October 2018

Acknowledgements

I thank the Lord from whom my help comes for making all things possible.

My supervisor was with me every part of the way with useful, timely words of advice and generous support, thank you Prof. Paul Barendse.

Mr. Chris Wozniak and Mr. Philip Titus were there for me many times I needed their help especially with lab activities and to the team at HYSA in the person of Jessica, Nabeel and Tapiwa, I say a very big thank you to them for their patience and support.

I would also like to express my gratitude to my colleagues in the person of Akin, Emmanuel, Kinglsey, Kunle, Linda, Lola, Olufemi, and Sean for being awesome companions throughout the journey.

My dear Toyosi was there with me to share each day's experience with encouraging words to keep me going - thank you.

To my parents and siblings who continue to support me, this thesis is dedicated to them.

APPLICATION FORM

Please Note:
Any person planning to undertake research in the Faculty of Engineering and the Built Environment (EBE) at the University of Cape Town is required to complete this form **before** collecting or analysing data. The objective of submitting this application *prior* to embarking on research is to ensure that the highest ethical standards in research, conducted under the auspices of the EBE Faculty, are met. Please ensure that you have read, and understood the **EBE Ethics in Research Handbook** (available from the UCT EBE, Research Ethics website) prior to completing this application form: http://www.ebe.uct.ac.za/ebe/research/ethics1

APPLICANT'S DETAILS		
Name of principal researcher, student or external applicant		FABUSUYI AKINDELE AROGE
Department		ELECTRICAL ENGINEERING
Preferred email address of applicant:		ARGFAB002@MYUCT.AC.ZA
If Student	Your Degree: e.g., MSc, PhD, etc	MSc
	Credit Value of Research: e.g., 60/120/180/360 etc.	180
	Name of Supervisor (if supervised)	PAUL BARENDSE
If this is a researchcontract, indicate the source of funding/sponsorship		
Project Title		FUEL CELL CONDITION MONITORING

I hereby undertake to carry out my research in such a way that:

- there is no apparent legal objection to the nature or the method of research; and
- the research will not compromise staff or students or the other responsibilities of the University;
- the stated objective will be achieved, and the findings will have a high degree of validity;
- limitations and alternative interpretations will be considered;
- the findings could be subject to peer review and publicly available; and
- I will comply with the conventions of copyright and avoid any practice that would constitute plagiarism.

SIGNED BY	Full name	Signature	Date
Principal Researcher/ Student/External applicant	FABUSUYI A. AROGE	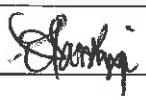	**16 Nov 2017**

APPLICATION APPROVED BY	Full name	Signature	Date
Supervisor (where applicable)	PAUL BARENDSE		**16 Nov 2017**
HOD (or delegated nominee) Final authority for all applicants who have answered NO to all questions in Section1; and for all Undergraduateresearch (Including Honours).			
Chair : Faculty EIR Committee For applicants other than undergraduate students who have answered YES to any of the above questions	R Behrens	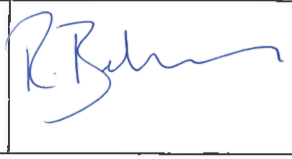	22 Dec 17

Abstract

Energy continues to remain the spine of all human development. As we continue to make advances in various levels, the need for energy in quantity, and even more recently, quality, continues to increase. The fuel cell presents itself as a promising prospect to solve one of mankind's current challenge - clean energy. The fuel cell is essentially an electrochemical conversion system which takes in fuel supply to produce electricity. Some key features make the fuel cell attractive as a power source. Firstly, its efficiency in practical applications is approximately 50% compared to the typical efficiency of 40% for a typical internal combustion engine [1]. Secondly, unlike the systems such as the internal combustion engine that typically releases carbon-monoxide which is a major greenhouse gas, the typical fuel cell system, produces just water and heat, alongside the useful electrical energy. These characteristics make it attractive as a clean energy supply capable of replacing the fossil-based supplies that are currently the mainstay.

Unfortunately, the fuel cell is far cry from an ideal system. Despite significant advantages of the fuel cell as a power supply, various challenges still exist which have hindered its widespread acceptance and deployment. The fuel cell at its core is a highly multi-physics system and its operational intricacies makes it highly prone to a series of fault conditions. This begs the question of durability - an important requirement of a viable power source. Another challenge is the fact that humanity currently struggles with an efficient method of producing hydrogen which is the fuel of choice for the fuel cell. Given the promises of the fuel cell however, research efforts continue to increase to further improve its viability as an

energy source competitive enough to meet mankind's need of clean energy.

This work presents results bordering on efficient diagnostic approaches for the fuel cell, aimed at improving the durability of the fuel cell. Particularly, two techniques targeted at improving the popular Electrochemical Impedance Spectroscopy (EIS) are presented. Conventional EIS takes significant amount of time, rendering it unsuitable for real-time diagnostics. Multi-frequency perturbation signals have been proposed to address this challenge. These however introduces concerns surrounding the accuracy of the resulting impedance measurement. Part of this work addresses some of the challenges with the fuel cell multi-sine impedance spectroscopy, such as measurement accuracy, by defining an optimized signal synthesis formulation. The proposed approach is validated in simulation and compared to the popular exponential frequency distribution approach using the appropriately defined error metric. Secondly, the chirp – as a frequency rich signal, is investigated as an alternative perturbation signal. Consequently, the use of the wavelet transform as an analysis tool of choice is presented. The characteristic nature of the chirp signal makes a broadband frequency sweep over time possible, hence enabling a faster impedance estimation. The resulting decomposition is harnessed for impedance calculation. The approach is tested in simulation and results for equivalent circuits are presented. It is shown that the resulting impedance spectrum well approximates the theoretical values.

To further validate both techniques in practice, a low-cost active load is designed and built. The active load enables the injection of an arbitrary signal using the load modulation technique. The device is tested and benchmarked against commercial frequency response analyzer (FRA) using the conventional single sine EIS technique. Both approaches developed – the improved multi-sine scheme and the chirp signal perturbation are demonstrated with the aid of the active load on a single cell fuel cell station. Outcomes of the experiment show significant accuracy from the two techniques in comparison with results obtained from the FRA equipment which implements the single sine technique. In addition, the two schemes enabled impedance results to be taken in a few seconds, compared to conventional single

sine EIS which takes several minutes.

Impedance measurements are also carried out in the presence of two prominent faulty conditions – flooding and drying, using the developed techniques. This demonstrates the capability of the proposed system to perform real-time diagnostics of the PEMFC using impedance information.

Table of Contents

List of Figures

List of Tables

Abbreviations

AFC Alkaline Fuel Cell

BET Brunauer–Emmett–Teller

BN Bayesian Networks

CF Crest Factor

CFS Co-prime Frequency Sequence

CNLS Complex Non-Linear Least Square

CO Carbon-monoxide

CPE Constant Phase Element

CV Cyclic Voltammetry

DAC Digital to Analog Converter

DAQ Data Acquisition

DC Direct Current

DFT Discrete Fourier Transform

DUT Device Under Test

ECSA Electrochemical Surface Area

EEC Electrical Equivalent Circuit

EIS Electrochemical Impedance Spectroscopy

EMD Empirical Mode Decomposition

FDA Fisher Discriminant Analysis

FFT Fast Fourier Transform

FRA Frequency Response Analyzer

FRA Frequency Response Analyzer

GA Genetic Algorithm

GDL Gas Diffusion Layer

ICE Internal Combustion Engine

MCFC Molten Carbonate Fuel Cell

MEA Membrane Electrode Assembly

MOSFET Metal-Oxide-Semiconductor Field-Effect Transistor

NI National Instruments

OCV Open Circuit Voltage

PAFC Phosphoric Acid Fuel Cell

PCA Principal Component Analysis

PEM Polymer Electrolyte Membrane

PEMFC Polymer Electrolyte Membrane Fuel Cell

RMS Root-Mean-Square

SCADA Supervisory Control And Data Acquisition

SNR Signal to Noise Ratio

SOFC Solid-Oxide Fuel Cell

STFT Short Time Fourier Transform

THD Total Harmonic Distortion

Chapter 1

Introduction

1.1 Background

This thesis details the research work done which focuses on the diagnostics and identification of fault mechanisms in the fuel cell. An initial investigation is first carried out to provide the basis for understanding the normal and critical limits of operational conditions for PEM fuel cells. Relevant conditional parameters are also investigated. Various degradation mechanisms are then investigated with their effect on operational conditions. These involved both analytical and experimental approaches. For the purpose of fault identification, various existing approaches are reviewed. Some issues arising in these are highlighted and discussed. An improved approach for the extraction of diagnostic information is then developed to push further towards an online condition monitoring. To make for a faster measurement, a novel signal injection technique is also developed as an online diagnostic measurement technique. In order to implement this technique, a wideband active load is designed and implemented. The device is then used to implement the new diagnostic technique proposed. The device is also demonstrated for suitability of use with existing methods. The results of this research effort push ahead existing capabilities in the fuel cell diagnostic space especially in terms of accuracy of and time cost of measurements. The methods and equipment developed are therefore useful towards efficient online diagnostics of the fuel cell which ultimately help to

ensure the durability of the fuel cell as an electrical energy source.

1.2 Research Question

The overall focus of this research is to answer the following question:
"How can fuel cell diagnostics be improved to extract information useful for online condition monitoring?"

This research question is pursued in parts by addressing the following questions:

- What are the key characteristic operational behaviours of the fuel cell?
- What are the current approaches to fuel cell diagnostics?
- How can we further improve signal perturbations for better performance of information extraction?
- Can we leverage advanced signals and signal processing techniques to improve measurements towards information extraction?
- How may we implement a system to realize to realize diagnostics online?

1.3 Research Objectives

To answer the questions raised in line with the aim of this research, the following objectives will be pursued:

- Investigate fuel cell characteristics behaviour and operational condition limits.
- Conduct a detailed literature review of the state of the art in terms of fuel cell diagnostic approaches.

- Review fuel cell impedance estimation techniques.
- Investigate approaches used to improve EIS.
- Investigate perturbation signals that may be used for efficient impedance estimation.
- Investigate advanced signal processing techniques for information extraction.
- Develop a low-cost system that may be used to implement EIS in an online scenario to test proposed techniques.

1.4 Research Methodology

The activities in this research involved analytical and experimental methods. Improved techniques for fuel cell diagnostics are developed using analytical approaches. These techniques are implemented using mathematical software packages and simulations carried out for initial validation as necessary. A power electronic device is designed and built using analytical simulation models and experimental tests. Also, experimental tests are carried out to characterise the fuel cell to ascertain its normal behaviour and to derive results used for benchmarking. The device developed is then used to test the developed diagnostic techniques on an experimental fuel cell setup.

1.5 Plan of Development

This work is disseminated in the chapters detailing key aspects of the overall research work as follows:

Chapter 2 provides an overview of the fuel cell, with specific focus given to the Polymer Electrolyte Membrane Fuel Cell (PEMFC). The electrochemical characteristics of the system is reviewed in terms of its thermodynamics and kinetics, to provide a general understanding of the system as well as identifying its operational characteristics. The key operational

conditions are also discussed.

Chapter 3 identifies existing PEMFC diagnostic techniques. Major electrochemical measurement techniques are detailed with a focus on impedance spectroscopy. Various diagnostic approaches developed in literature are reviewed under broad categories. Key underlying ideas of various methods as well as the strengths and limitations are discussed.

Chapter 4 includes the details on the experimental setup, procedures and parameters deployed throughout this the work.

Chapter 5 discusses the design and implementation of the active load device used to realize the load modulation technique. Key design considerations are presented, and results of tests are also shown to elucidate performance for fuel cell impedance measurements.

Chapter 6 presents the proposed scheme for improving the accuracy of impedance measurements using broadband signals. Comparisons are made with existing approaches and the improvement in accuracy is demonstrated. The approach is further deployed towards diagnosis of two major fault conditions of the PEMFC - flooding and drying, and results are presented for implementation using the single-sine on a commercial FRA and the proposed multi-frequency signal synthesis on the active load developed as part of this work.

Towards further reducing the time of impedance measurements, chapter 7 investigates the use of the chirp as a perturbation signal. The wavelet time-frequency analysis technique is also presented. Results are shown for the estimated impedance for simulated circuits and the fuel cell, and compared to those obtained using the commercial FRA.

Conclusions from the research work and recommendations for future research is provided in chapter 8.

1.6 Contributions and Research Outputs

This work contributes towards the diagnostics of the fuel cell with special attention to the Electrochemical Impedance Spectroscopy technique. In so doing, two key ideas were developed - the improvement of accuracy of impedance measurements using a multi-frequency signal as well as the use of the chirp as a perturbation signal to enable faster measurements. To validate the techniques, an active load device was also designed and built as a portable and low-cost alternative to the commercial FRA device, and to afford the necessary flexibility required for the implementation of the proposed techniques. Results from this work could be used to improve the fuel cell diagnostics using the impedance response technique with capability for real-time state of health determination.

Conference Publications

1. F.A Aroge, P.S. Barendse, "Signal Injection by Active Load Modulation for PEM Fuel Cell Diagnostics", IEEE PowerAfrica, Cape Town, South Africa, 2018

2. F.A Aroge, P.S. Barendse, "Time-Frequency Analysis of the Chirp Response for Rapid Electrochemical Impedance Estimation", IEEE Energy Conversion Congress and Expo (ECCE'18), Portland Oregon, 2018.

Chapter 2

Theory and Background (Fuel Cell System Overview)

2.1 Introduction

Energy continues to be a significant factor in human economic development and the need for energy continues to increase. Fossil fuels have catered for this growing energy needs over the years. However, the increase in the consumption of fossil fuels has been identified to have a negative impact on the environment. This has led to the quest for cleaner energy sources. Renewable energy sources such as solar, wind and hydro have become topics in major energy discourse in recent years, and many countries have made effort to integrate these energy sources in their energy mix. The nature of renewable energy sources however poses significant challenges for traditional grid integration. The intermittent nature of these sources creates concerns around grid stability. Electrical storage technologies have also gained traction over the years. They have found use in various applications such as electric vehicles, grid storage and other portable applications. The energy density associated with typical battery technologies is however limited for broader application. This is in addition to the high cost associated with battery technologies. The fuel cell, also an electrochemical system like the battery, has however been the focus of research efforts for some of its advantages.

The fuel cell is essentially as an electrochemical energy conversion system. It transforms chemical energy derived from a supply of fuel to useful energy in form of a direct current electricity. The process typically involves taking in Hydrogen and Oxygen gases as fuel supply and the conversion of this fuel to electricity occurs directly with no moving parts. The fuel cell shares similarity with the combustion engine as an open chemical energy conversion system but produces electricity directly unlike the internal combustion engine (ICE) that undergoes a mechanical phase. Also, as a direct chemical-electrical energy conversion system, the fuel cell shares significant properties with the battery particularly in the conversion process.

Leveraging the attributes of an open system like the ICE with a direct conversion as in the battery is what makes the fuel cell system generally attractive as an energy source [1]. As an open system, the fuel cell will continue to provide energy as long as the fuel supply is ensured. This implies longer supply duration is possible. The characteristic modularity of the fuel cell also allows for independent scaling, an advantage over the battery systems which scales poorly [3]. The direct production of electricity without an intermediate phase also helps to guarantee improved efficiency over the ICE with about 83% efficiency assuming full conversion of the free energy.

Unfortunately, the fuel cell is far cry of an ideal system. Despite significant advantages of the fuel cell as an energy system, various challenges still exist which have hindered its widespread acceptance and deployment. A current challenge of the fuel cell is its current power per unit of system volume and mass. Also, Hydrogen as a fuel for the fuel cell is not readily available in pure forms required. Alternatives to Hydrogen, such as methanol, pose challenges to the system and inherently defeats the purpose of a clean energy source as they have to undergo reformation - an inherently environmental unfriendly process. Pure hydrogen also has a low volumetric energy density and is difficult to store [3]. In addition to these challenges, the fuel cell at its core is a highly multi-physics system and its operational intricacies makes it prone to a series of fault conditions. This begs the question of durability

- an important requirement of a viable power source. Given the promises of the fuel cell however, these challenges are being addressed and are currently the focus of various research efforts to further improve the viability, and in turn, the competitiveness of the fuel cell as an energy conversion system.

Fuel cells are classified according to their distinguishing properties such as operating temperature and material constituents [3], these include:

- Polymer Electrolyte Membrane Fuel Cell (PEMFC)
- Solid-Oxide Fuel Cell (SOFC)
- Phosphoric Acid Fuel Cell (PAFC)
- Alkaline Fuel Cell (AFC)
- Molten Carbonate Fuel Cell (MCFC)

Of the different types, the Polymer Electrolyte Membrane Fuel Cell is the most popular for its distinct advantages in its simplicity and viability [1] and is therefore focus of this research work.

2.2 Fuel Cell as an Electrochemical System

While the end goal of the fuel cell is to produce electricity, this occurs as a result of complex processes within the system. The processes maybe divided into the thermodynamics and the kinetics of the fuel cell. The thermodynamics predicts the theoretical maximum voltage output of the fuel cell [3] as will be shown in a subsequent section. As current is drawn from the cell however, the kinetics of the cell becomes the dominant process resulting in a voltage drop with increased current. These characteristics set the operational output and efficiencies. Studying these processes and their effects will be the focus of this section and subsequent ones.

The key chemical reaction governing the fuel cell electrochemical conversion is the combustion of Hydrogen to give water and energy [2]. This reaction may be expressed as follows (2.1);

$$2\,H_2 + O_2 \longrightarrow 2\,H_2O \tag{2.1}$$

The above could be broken down into two half reactions to show the interactions that result in electron flow as in (2.2) and (2.3).

$$2\,H_2 \longrightarrow 4\,H^+ + 4\,e^- \tag{2.2}$$

$$O_2 + 4\,e^- + 4\,H^+ \longrightarrow 2\,H_2O \tag{2.3}$$

The simple fuel cell assembly consists of two electrodes - the anode and the cathode which are electrically conducting and porous to allow passage of gases. These two electrodes are separated by a membrane layer which would normally conduct proton ions, hence the name proton exchange membrane. Electrons must travel through a separate path to enable the extraction of useful work from the reactions. This path may be provided as an external circuit, allowing electrical current which may then be connected to a load. A simple fuel cell system may be simply represented as shown in Fig. 2.1.

To facilitate the reaction occurring at the interface of the electrodes and electrolyte (or membrane), a layer of catalyst lies between these two. Platinum is often used as the catalyst of choice [1], and the electrochemical reactions occur at the catalyst surface interfacing the electrolyte and electrode. Although various intermediate reactions are involved, the equations in (2.2) and (2.3) summarize the mechanisms by which electrons and protons are formed. Hydrogen is typically fed through the anode as fuel. Each Hydrogen breaks up into its constituent elements - a proton (H+) and an electron (e^-) in an ionization process as given by (2.2). The electron is allowed passage through an external circuitry while protons flow

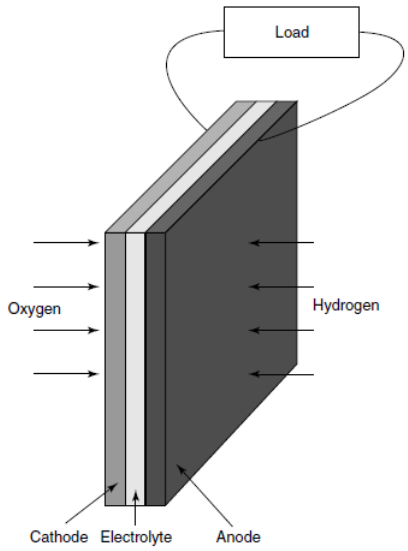

Fig. 2.1: Basic cathode–electrolyte–anode construction of a fuel cell. [2]

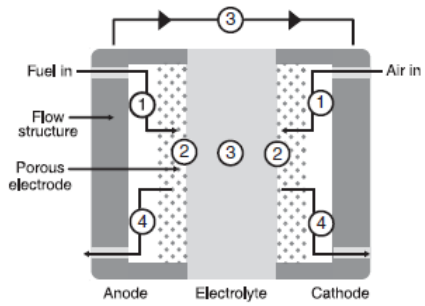

Fig. 2.2: Cross section of fuel cell illustrating major steps in electrochemical generation of electricity: (1) reactant transport, (2) electrochemical reaction, (3) ionic and electronic conduction, (4) product removal. [3]

through the membrane. The electrons upon reaching the cathode, recombine with protons and the oxygen being fed in to produce water as given in (2.3). The cumulation of these steps helps to produce the desired product in form of a direct current output flowing across the external circuit. The sequence of steps is as illustrated in Fig. 2.2.

These key sequences of steps and processes involved in the electricity production are summarized in the following.

The fuel supply

The fuel supply deals with the supply of reactants including the fuel and oxidant. The fuel delivery to reaction points is key to the overall operational performance of the fuel cell. For a typical fuel cell in operation, the fuel supply system is a dynamic process. For normal operation, the required fuel supply is dependent on the operating current among other factors. A starving condition may result when reactants are not adequately provided [7]. It is therefore required to enable control mechanisms to ensure that adequate reactants are provided as required. The supply path ranges from the fuel supply by the mass controllers through channels that help with conditioning processes involving temperature and pressure, through to the flow fields plates. The mass controllers are required for the control of the fuel supply amounts while the flow fields help to provide efficient channels for the transport and distribution of gases over the fuel cell. These flow fields come in various designs such as the serpentine, and parallel flow fields in order to help improve passage of reactants for different cases [7].

The reaction processes

Upon delivery of reactants, electrochemical reactions proceed at the electrodes. These reactions result in the production of ions and electrons. Paths are provided for movement of these ions and electrons from one electrode to the other to maintain a charge balance [3]. The electron is typically provided an external path which may be connected to an external load producing current while the movement of ions is achieved through the membrane. The transport of ions through the membrane is however not an efficient process, posing challenges to the fuel cell system by way of an increase in resistance. Membranes need to be adequately hydrated and made as thin as possible to improve ion passage [7]. The rate at which this electrochemical stage progresses largely determines the generated output of the cell. Catalyst such as platinum are therefore used to speed up this process which in turn improves the

overall performance of the cell.

Waste transport

As described in equation (2.1), water constitutes the waste product of the fuel cell reaction process. It is important that the waste product when generated, be adequately removed. This is needed to prevent blockage and ensure the efficient supply of fuel to reaction sites as waste, such as water, may inhibit the flow of gases which could lead to performance drops. This situation where the waste water prevents normal reactant flow is described as flooding and represents a prominent source of failure in PEMFC operation [7]. Heat is also generated as a by-product of the reactions and may be removed as necessary, by means of cooling mechanisms.

2.3 Fuel Cell Thermodynamics

The fuel cell as a typical thermodynamic system is governed by thermodynamic laws and processes which predicts its operational limits amongst other things. The total energy available from the Hydrogen fuel is given by the enthalpy of the key reactions [7]. This is about 284 kJ for 1 mol. of Hydrogen's higher heating value at room temperature and pressure [1] and may be regarded as the input energy to the cell in the form of fuel supply. The heat transfer process results in a change in entropy within the system which is given as (2.4);

$$ds = \frac{dQ_{rev}}{T} \tag{2.4}$$

where ds is the change in entropy within the system resulting from heat transfer dQ_{rev} for a given temperature, T. The theoretical energy available for electrical work is thus given by

the Gibbs free energy in equation (2.5).

$$\Delta G = \Delta H - T\Delta S \tag{2.5}$$

This gives the theoretical value of the open circuit voltage of a hydrogen fuel cell at room temperature. The variation of this thermodynamic potential with respect to conditional elements such as the temperature and pressure is expressed by the Nernst equation in (2.6) [3].

$$E = E^0 + \frac{\Delta\hat{S}}{nF}(T - T_0) - \frac{RT}{nF}\ln\frac{\prod_{products}^{v_i}}{\prod_{reactants}^{v_i}} \tag{2.6}$$

where E^0 is the standard cell potential, $\Delta\hat{S}$ is the change in entropy, n is the number of electrons transferred in the cell reaction, F is the Faraday constant, R and T are the universal gas constant and temperature (in kelvin) respectively, and v_i is the chemical activity of specie i.

2.4 Fuel Cell Kinetics

While the thermodynamics set the limit of the voltage, the fuel cell kinetics takes over when the fuel cell is in operation. The kinetics of the electrochemical reactions dictate the electron transfer process and understanding this is key to improving the operational behaviour of the fuel cell. Various efforts aimed at improving the overall performance of the system, target specific mechanisms involved in the electron-transfer process. Particularly the production of electric current is a direct result of the kinetics of the fuel cell as it affects the rate of the electrochemical reaction.

The rest of this section will outline the various kinetic characteristics as derived from the electrochemical kinetics and the relationship to the fuel cell electrical output will be discussed in line with the characteristic $i - v$ curve.

2.4.1 Kinetics at the Electrode

The electrochemical reactions that take place at the triple phase boundary consisting of the electrolyte, electrode and gaseous fuel interface result in the production of free electrons. The rate at which this occurs determines the electrical current. The relationship may be expressed from Faraday's law as in equation (2.7);

$$i = \frac{dQ}{dt} = \frac{d(nFN)}{dt} = \frac{nFdN}{dt} \tag{2.7}$$

where $\frac{dN}{dt}$ represents the reaction rate, n is the number of electrons and F is the Faraday constant. The equation expresses the direct relationship between the current and the rate of consumption of reactants. The current i here gives the total current resulting from the surface reactions. Thus, an increase in the system area will translate to an increase in the current. To however understand the relationship between the reaction rates and the current produced, it is important to decouple the area in the quantity of measure. This is achieved by normalizing the current from (2.7) as shown below (2.8) to current density. Where A is the interfacial area.

$$j = \frac{i}{a} \tag{2.8}$$

For reactions to proceed into products, an energy barrier known as the activation energy, must be overcome [3]. The rate at which the reaction proceeds is dependent on this since only the reactants in the activated state can transform to become products. The probability that a species is found in the activated state is given in equation (2.9). The reaction rate may then be expressed as in (2.10).

$$P_{act} = e^{-\frac{\Delta G_1}{RT}} \tag{2.9}$$

$$J = C_R^* f^* P_{act} \tag{2.10}$$

$$j_1 = j_0 e^{\frac{\alpha n F \eta}{RT}} \tag{2.11}$$

$$j_2 = j_0 e^{-(1-\alpha)\frac{nF\eta}{RT}} \tag{2.12}$$

Where;

i $= arg\min(|f_j - P|)$

P_{act} is the probability of finding a reactant in activated state

ΔG_1 is the size of energy barrier existing between reactant and activated states

R is the gas constant

T is the Temperature in Kelvin

J_1 is the forward reaction rate

C_R^* is the reactant surface concentration in mol/cm2

f_1 is the decay rate to products

j_0 is the exchange current density

α is the charge transfer coefficient

η is the overvoltage

n is the number of electrons transferred in the reaction

F is the Faraday's constant

$j_1 \& j_2$ are forward and reverse current densities respectively.

Equation (2.10) gives the reaction rate for the formation of products from reactants. In order to effect an increased rate of the desired forward reaction, some portion of the full potential as given by the open circuit voltage (OCV) is sacrificed. This helps to reduce the

forward activation barrier while increasing that of the reverse by the reduction of the Galvani potential [3]. The forward and the reverse current densities considering the changes in the activation barrier may then be given as in equations (2.11) and (2.12). The two reactions result in release and consumption of electrons and the resultant of the forward and the net current is given as (2.13),

$$j = j_0(e^{\frac{\alpha nF\eta}{RT}} - e^{-(1-\alpha)\frac{nF\eta}{RT}}) \tag{2.13}$$

which is known as the Butler-Volmer equation. This represents the non-linear relationship between the current and the sacrificed voltage, where an exponential increase in current results from an increasing potential drop. This sacrificial voltage represents a loss due to the activation barrier and is known as activation overvoltage [3]. At equilibrium when there is effectively no net current, $j1 = j2$ [3], and this dynamic equilibrium point is termed the exchange current density.

2.4.2 TAFEL Approximation

Two limiting cases may be deduced from the Butler-Volmer equation in (2.13). The resulting approximation of the equation may be analysed for very small and very large activation over-voltage. In the case where η_{act} is very small, equation (2.13) reduces to (2.14) . On the other hand, when η_{act} is very large, the equation reduces to (2.15).

$$j = j_0\frac{nF\eta_{act}}{RT} \tag{2.14}$$

$$j = j_0 e^{\frac{\alpha nF\eta}{RT}} \tag{2.15}$$

The latter case effectively neglects the reverse reaction and is a useful result since the fuel cell is operated in high current densities which correspond to high η_{act}. This approximation

for large η_{act} is known as the Tafel equation given in (2.16).

$$\eta_{act} = \frac{RT}{\alpha nF} \ln \frac{j}{j_0} \tag{2.16}$$

2.5 Fuel Cell Losses

The output voltage of the fuel cell in practical application tends to be lower than the thermodynamically set potential. This is the case even when the system is not connected to any external load. This voltage drops even further with the connection of an external load when the fuel cell now generates current. These drops in voltage is attributed to different loss mechanisms within the fuel cell system. The major losses are described below.

Activation losses

This loss describes the slowness of the reactions occurring at the electrode surface [2]. It occurs as a result of the finite amount of energy required for the reactants to proceed to products leading to the production of electricity. The loss due to activation is more pronounced at the cathode than the anode due to the sluggish kinetics of the oxygen reduction occurring at the cathode [1]. The activation loss may be expressed from (2.15) to give (2.16). It is obvious from the equation that an increase in the exchange current density results in a reduced activation loss. This relationship is important to improve the performance of the cell. The deviation from the thermodynamic potential due to the activation loss acting alone can now be represented as (2.17).

$$v_0 = E - v_{act} \tag{2.17}$$

$$v_{act} = \frac{RT}{\alpha nF} \ln \frac{j + j_i}{j_0} \tag{2.18}$$

The graph illustrating the change is shown in Fig. 2.3 for different exchange current densities.

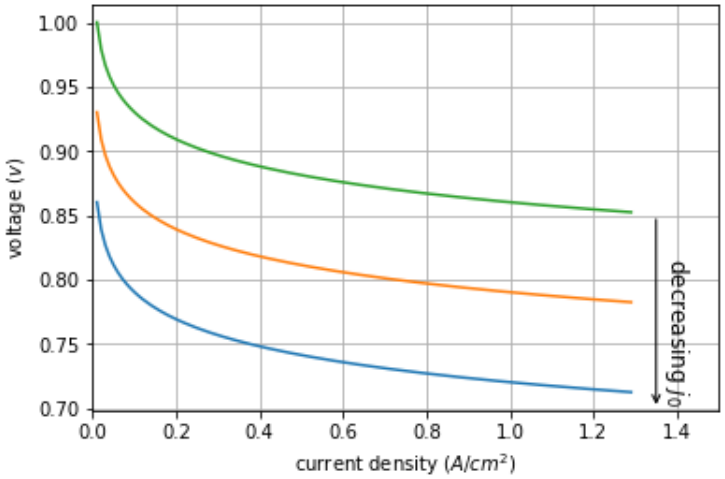

Fig. 2.3: Calculated curves for different values of j_0 illustrating the effect of activation potential on the fuel cell with $\alpha = 5$, $T = 353.15K$, $n = 2$.

Internal current losses

At OCV, the fuel cell experiences significant losses due to the leakage currents. In addition to the normal condition of allowing the flow of protons, the polymer membrane interface unfortunately allows passage of small amounts of electrons flowing from the anode to cathode. This effectively reduces the amount of electrons available to travel through the external circuit to produce useful electrical energy. This effect is however insignificant during operational conditions as the leakage current is relatively much smaller than the current flowing in the external circuit. This is partly so because the concentration of gases at the electrolyte also reduces in operation which in turn reduces the possibilities of a leakage through the membrane [2].

Ohmic losses

Ohmic losses occur in the fuel cell as a result of resistance to the flow of ions and electrons. It is majorly attributed to the ion conductivity of the electrolyte. In order to reduce this, the electrolyte is usually made to be as thin as possible. However, this is done in compromise with the need for enough thickness to also prevent possible gas mixing and ensure mechanical stability [3]. Besides the thickness, poor conductivity of the membrane may occur as a result

of poor humidification of the membrane. The components of the fuel cell in the path of electron flow also contribute to the ohmic resistance. These components may include the electrodes and interconnections, but this is usually relatively insignificant [1]. This ohmic loss contributes to the drop from the thermodynamic potential as given by equation (2.19).

$$v_{ohmic} = ir \tag{2.19}$$

Where i is the current and r is the ohmic resistance.

Concentration/mass transport losses

Concentration losses result from a deficiency in reactant quantity in the reaction area leading to an activity gradient. As reactants are being consumed in operation, a change in concentration is expected around the electrodes. This may occur due to a number of factors on either of the anode and cathode sides. The concentration gradient formed depends on the rate at which the gases are being replenished as well as the ease of flow offered by the flow fields. At high currents, this effect is more pronounced because reactants may be consumed at a much faster rate than they are being supplied. Also, for different fuel supply, such as air in substitute for oxygen, it is expected that the concentration of oxygen is lower in the former.

Concentration losses occur in the fuel cell system in both open circuit as well as in closed circuit operation and this is predicted by the Nernst and Butler-Volmer (BV) equations in (2.20) and (2.21) respectively [3].

$$v_{\text{nernst-conc}} = \frac{RT}{nF} \ln \frac{j_L}{j_L - j} \tag{2.20}$$

$$v_{\text{BV-conc}} = \frac{RT}{\alpha nF} \ln \frac{j_L}{j_L - j} \tag{2.21}$$

The limiting current density, j_L describes the point at which the reactants are consumed as fast as they are being supplied. This leads to a zero net concentration beyond which a higher current density is not sustainable [3]. The two equations put together sums up

to analytically give the losses due to concentration of the reactants. To ensure stable operation, reactants need to be supplied in the needed amounts with changing consumption rates.

The losses result in a drop of the potential from the thermodynamically predicted voltage. Together with the previously described losses, the resultant voltage may therefore be written as in (2.22).

$$v_0 = E - v_{act} - v_{ohmic} - (v_{\text{nernst-conc}} + v_{\text{BV-conc}}) \tag{2.22}$$

2.6 Fuel Cell Conditioning and Basic Characteristics

2.6.1 Introduction

For a fuel cell in operation, different conditions need to be set in place. Prominent among these conditions are the temperature, pressure and humidity. Some of the conditions such as the temperature may require control at different stages depending on the fuel cell configuration. These conditions are important as they are closely linked to the fuel cell overall performance. Also, significant deviations from normal operation may result in degradation in the system. This section outlines the various key conditions of the fuel cell and discusses their effects. The polarization curve is employed as a visual aid to emphasize variations in overall performance.

2.6.2 Temperature Conditions

The operating temperature of a fuel cell is an important conditioning parameter for the PEM fuel cell. The thermodynamic potential is dependent on the temperature as given by the Nernst equation (2.6). This predicts a lower voltage for increased temperature. However, the improvement in kinetics due to increased temperature tend to be much more than its effect on the thermodynamic potential. The forward reaction current density increases exponentially with temperature as given by equation (2.10). As temperature increases, the particles are

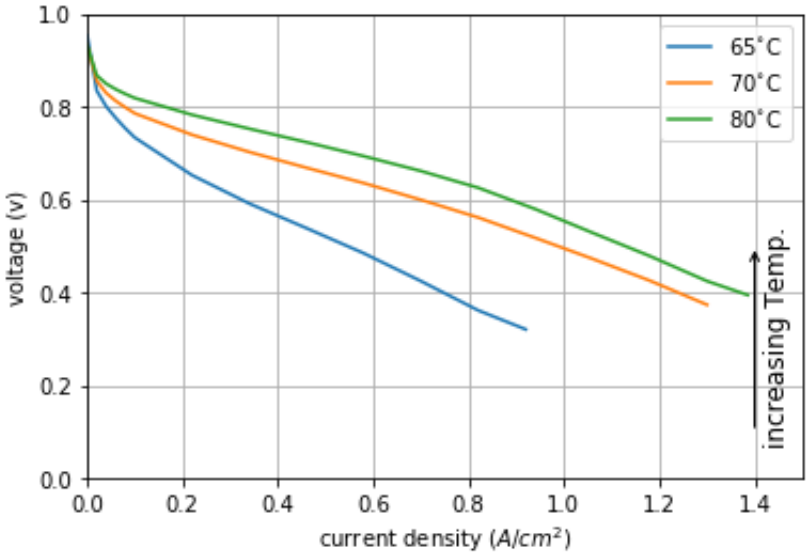

Fig. 2.4: The effect of temperature shown on the polarisation curve.

more energized and this effectively increases the probability of reactants being activated to form products. This positive effect of temperature is also experienced in the ion conductivity as well as mass transport mechanisms [3]. In general therefore, the potential will tend to increase with increase in temperature up to certain points which varies from cell to cell [1]. The upper limit may be set by the membrane as is the case for the polymer electrolyte membrane which is about a 100°C, after which dehydration may set in [1]. Fig. 2.4 shows the polarization curve for various temperature set points. It is obvious from the curves that an increase in temperature results in overall improved performance. Because the fuel cell conversion processes also involve some heat dissipation, heat removal is required in addition to a heat supply to control the internal temperature. Heating may be achieved by means of heating elements or circulatory heating fluids, while the cooling system may include a fan for air cooling or a circulatory coolant fluid system.

2.6.3 Pressure Conditions

Because the fuel supply to the system is predominantly gaseous, pressure plays an important role. The Nernst equation explains the pressure relationship with the reversible potential in (2.6). Because of this log relationship however, an increase in pressure corresponds to

only a small improvement in reversible potential. The pressure effect is most observed in the kinetics of the fuel cell. An increase in pressure translates to an increase in concentration which is good for the exchange current density.

2.6.4 Humidity Conditions

Water management is a prominent concern for the PEMFC since water is required for the transport of gases. For normal operation, the inlet gases need to be adequately humidified. Inadequate humidification results in a drying condition which reduces the performance of the fuel cell significantly. This reduction is due to the movement of ions which is dependent on water content on the membrane. The PEM fuel cell popularly employs the persulfonated polytetrafluoroethylene (Nafion) as the electrolyte [3]. The chemical structure of the Nafion are such that its transport mechanism are tightly linked to its water content in a similar manner to a liquid electrolyte. However, the hydration should also be such that not too much water is accumulated in the flow channels as this tends to inhibit flux of gaseous reactant which leads to a drop in performance.

2.7 Fuel Cell Efficiency

It has been discussed that the fuel effectively acts as an electrochemical energy conversion system - converting chemical energy in fuels to electrical energy. Like any conversion system this process is not lossless. In addition to the limits imposed by the thermodynamics of the conversion process, the fuel cell also suffers some losses in operation. The efficiency of an energy system may be expressed as follows (2.23);

$$\text{Efficiency, } \eta = \frac{\text{usable energy}}{\text{total available energy}} \tag{2.23}$$

As dictated by the thermodynamics, the useful work done is given by the Gibbs free energy, ΔG, while the total energy made available is given by the heating value of the reaction. At room temperature and pressure, the Gibbs free energy and heating value are given

as -237.17kj/mol and -285.83kj/mol [3] respectively. This results in the thermodynamic efficiency of the fuel cell given in equation (2.24).

$$\eta_{thermo} = \frac{\Delta G}{\Delta h} = \frac{273.17kJ/mol}{285.83kJ/mol} = 0.83 \tag{2.24}$$

Other contributions to the drop in efficiency include losses due to voltage losses and inefficient fuel conversion processes that occur in typical operation. The voltage losses include the losses due to kinetic processes that must occur in the fuel cell operation. Also, some of the supplied fuel does not participate in the key reaction that results in the production of electrical energy. While some participate in other side reactions, others may just flow through via leakages. With consideration for these, the overall efficiency for a fuel cell may be expressed as in (2.25) [3].

$$\eta_{\text{overall}} = \eta_{\text{thermo}} \times \eta_{\text{voltage}} \times \eta_{\text{fuel}} \tag{2.25}$$

2.8 Conclusion

This chapter presents an overview of the fuel cell with a focus on the PEM fuel cell technology. The different electrochemical characteristics have been discussed under the categories of the thermodynamics and the kinetics of the key electrochemical reactions. The impact these characteristics have on the electrical properties of the fuel cell are also presented. Various fuel cell operational conditions such as temperature, pressure, and humidity and their impact on the overall performance of the fuel cell are also investigated. Finally, the determination of the fuel cell efficiency is presented to provide understanding of the operational limits. Insights developed from this chapter form the basis of various experimental procedures and the analysis of results in this work.

Chapter 3

PEMFC Diagnostics and Condition Monitoring

3.1 Introduction

Fuel cell applications in transportation and stationary applications require a life-expectancy of about 5000h and 40000h respectively, but the life-time of a typical PEMFC is currently around 10000h [8]. This durability requirement has made diagnostics and condition monitoring a highly pertinent area of research to ensure the viability of the fuel cell as an energy source. The fuel cell as a multi-physics system relies on a number of operational conditions making it highly prone to faulty conditions. As a physical system, a fuel cell typically consists of a number of components. These include the catalyst, bipolar plates, the membrane, the gas diffusion layers (GDL), as well as the gaskets, catalyst supports and sealings [7]. Safe operation relies on the proper functioning of each of these as defects in each one may lead to the failure of the entire fuel cell system. Some of these components such as the catalyst and membrane, degrade by transforming from their original state and becoming dissolved components. Changes involving the catalyst layer as well as the GDL may also occur, and could lead to thermodynamically unfavourable interactions with water. Others such as the carbon support may undergo corrosion while the bipolar plate may experience film growth [7]. The degradation mechanisms may be as a result of operational procedures

which lead to gradual wear and tear over time. These include procedures such as the start-up and shut-down operations, loading, among others [7].

As an electrochemical system, various complex processes such as charge transport, heat transfer, electrochemical reactions and fluid flows occur in operation. For normal operation, these processes need to operate within acceptable margins. Associated operational conditions such as the humidity, temperature, pressure and fuel feeds have a major impact on the overall system durability. The manner in which the degradation occurs is also dependent on the design of the fuel cell and work is being done in this area [9] to research more durable and fault tolerant designs.

The degradation and failure mechanisms are often interlinked as well as cascaded. A drying issue for instance may lead to catalyst degradation culminating in an overall drop in performance. For this reason, it is important to isolate and analyse faulty conditions from a system viewpoint to gain understanding of the failure modes. This understanding is necessary for diagnostics as well as seeking ways to improve the overall system durability. In order to keep the system within allowable operational conditions, monitoring the state of health of the system continuously is necessary. To achieve this, knowledge of the system and fault mechanism is required as well as a fault identification scheme.

Faults in fuel cell system may be characterised in terms of the response time, resulting effects, the parameters involved and the reversibility of the faults [4]. Fig. 3.1 summarises common fault conditions the PEMFC may be subjected to.
While flooding and drying faults may take up to a few minutes to be effected, a short circuit or starvation fault manifests in milliseconds. The effects of fault occurrence are mostly observed in catalyst and membrane degradation with losses in performance. For faults such as the short circuit and starvation, these effects are relatively rapid and mostly irreversible [10, 11]. Flooding and drying faults tend to be reversible and result in slower degradations [12, 13] . Because of the inherently complex process of the fuel cell, different parameters interplay in

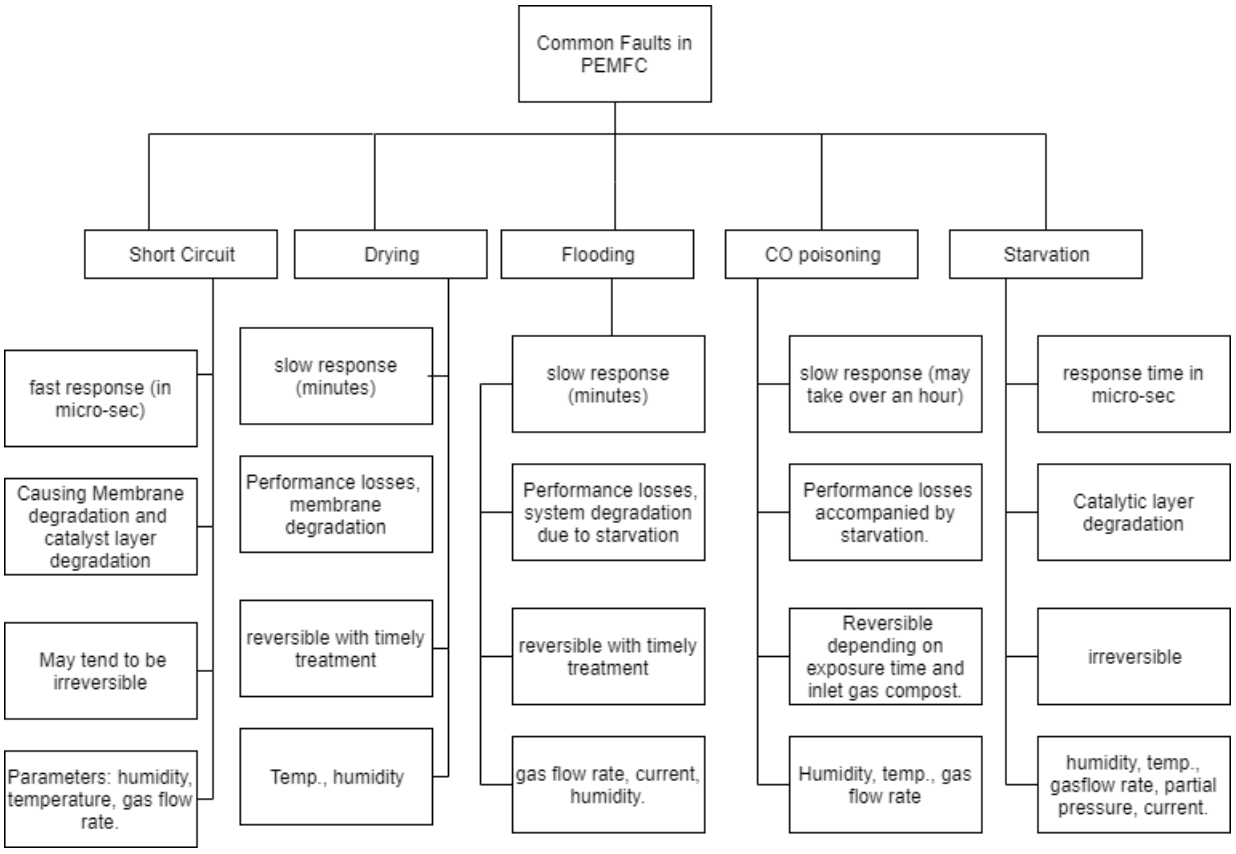

Fig. 3.1: Major PEMFC fault characteristics (adapted from [4]).

the event of a faulty scenario. They include humidity, temperature, flow rate, pressure and loading conditions [14, 15].

Monitoring system parameters is one way of gaining knowledge about the system. Data collected from operational conditions such as temperature, pressure, voltage and current output could help to provide representative information regarding the state of health of the fuel cell system. This may then be analysed to identify characteristic patterns for an anomalous condition. This would ultimately help identify a faulty condition which could then be mitigated by actuating necessary responses. Because of the complex nature of the fuel cell, condition monitoring is not trivial, as processes involved in the fuel cell tend to be tightly coupled. This makes it often difficult to separate effects observed in measurements and begs the need for advanced measurement techniques. To this end, several methods have been established to diagnose as well as characterise the fuel cell.

Various experimental procedure exist for characterisation of the fuel cell. These procedures typically involve a measurement stage and a subsequent analysis stage in order to interpret the collected measurement. A candidate measurement technique will be required to give useful information regarding the internal processes in the fuel cell with consideration for the time involved and whether it may be conducted while the system is in operation. The rest of this chapter will detail some of existing diagnostic and characterisation procedures for the fuel cell. The general measurement approaches for the fuel cell are first introduced. Various techniques are then examined in terms of measurement and analytical approaches while identifying typical applications and inherent limitations. In addition to standard approaches, some more recent methods developed in literature are also discussed.

3.2 PEMFC Measurement Techniques

As an open system, the fuel cell, operates on a combination of accessible variables. Measurements of these variables hold significant information on the state of health of the system for any given time. More particularly, for online diagnostics, measurement serves as a means to acquire signals which may be used to determine the condition of the fuel cell. These variables include pressure, temperature, humidity, stoichiometry as well as the voltage and current. Some of these, such as humidity and temperature are typically controlled to set operational conditions. Since the primary goal of the fuel cell is to generate electricity, the voltage and current serve as key monitoring parameters. As such, many of the condition monitoring techniques are centred around these two variables. The time information associated with these two parameters is also of importance particularly for the fuel cell as a dynamic system. Taking either of the voltage or current measurement with respect to time serves as an underlying concept for most diagnostic techniques. For the fuel cell, the current and voltage can however not be varied independently. Control of either one automatically results in the other being set by the electrochemistry of the system. Due to this relationship, typical measurements often set either the voltage or the current while the other is being analysed. A condition where the current is set while other response variables including the voltage are monitored is termed a galvanostatic measurement while a potentiostatic measurement has the voltage set while other variables including the current are read off. Provided steady state conditions are observed, either approach is expected to yield the same result for typical measurements [3].

To carry out reliable measurements on the fuel cell, some conditions need to be put in place. Fuel cell performance is very dependent on its operational conditions as identified in the previous chapter. Equipment such as mass flow and pressure controllers, cooling system are required to maintain a suitable operational condition to carry out needed tests. It is also often required for most measurements to commence with some “warm up” of the fuel cell system. This helps to bring the system to steady state in terms of its internal electrochemical mechanisms. In particular, the membrane needs to be hydrated and gases need to be flow-

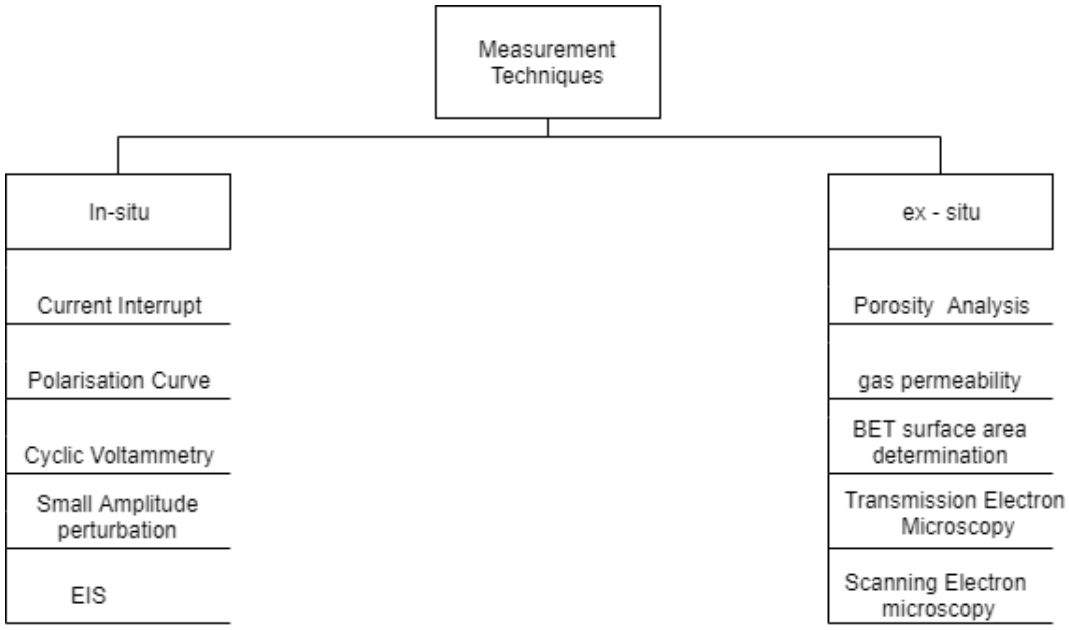

Fig. 3.2: Classification of fuel cell measurement techniques.

ing in accordance to set conditions. This process also allows other conditions such as the temperature and pressure to attain their steady state. These series of procedure is termed conditioning and also ensures validity and repeatability of experimental results [3].

Measurement techniques fall under two broad categories of in-situ and ex-situ techniques based on the manner and procedure in which they are performed. This categorisation is summarised in Fig. 3.2, with common examples for each.

In-situ techniques include those measurements that may be performed while the system is in operation. These typically involve the measurement of electrochemical variables such as voltage, current and time in order to determine the state of health of the fuel cell system. Examples of measurements that fall in this category include the polarization curve, current interrupt, and the cyclic voltammetry (CV) measurements. Ex-situ techniques go beyond just measuring operational variables to also include determining component structures and properties. The ex-situ techniques may also require that the system is disassembled in order to carry out some of the needed procedures. Some ex-situ techniques include porosity analysis,

Brunauer–Emmett–Teller (BET) surface area determination and gas permeability [1]. This work is focused on approaches suitable for monitoring the state of health of the fuel cell while it is in operation, as such, the ex-situ measurements will not be considered any further in this work. The remainder of this section focuses on the in-situ techniques for diagnostics and characterisation.

3.2.1 The Polarisation Curve

The polarisation curve is a means by which the interaction between the current and voltage is represented. As discussed in the previous section, keeping either voltage or current constant would result in the current or voltage being set by the electrochemistry of the system. We can therefore have the following equations;

$$\text{galvanostatic: } v = f(i) \tag{3.1}$$

$$\text{potentiostatic: } i = f(v) \tag{3.2}$$

where v and i are the voltage and current of the fuel cell respectively.
In order to carry out the polarisation curve measurement, the current (or voltage) is set by a loading system and the corresponding voltage (or current) is read off. This is repeated for increasing current (or voltage) set points until a predetermined operational threshold is reached beyond which the fuel cell system may be damaged. Because the polarisation curve is a steady state measurement, some time must be allowed for the system to reach steady state before taking the response for each step of the measurement. Failure to do this may result in recording undesired measurement due to transient processes which occur as a result of the step change [3].

The polarisation is useful for knowledge of the overall performance of the fuel cell for given conditions of operation [1]. Figure 3.3 describes an example polarisation curve showing the 3 major regions which are:

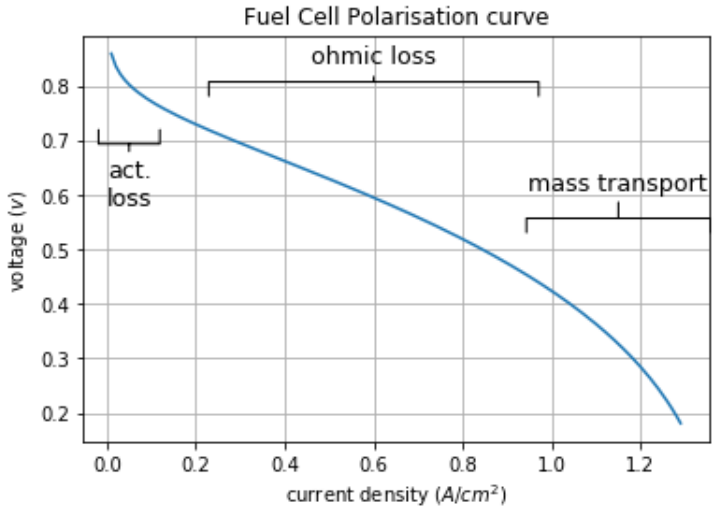

Fig. 3.3: Calculated polarisation curve illustrating the three major loss regions.

- the activation region
- the ohmic region
- the concentration region.

These regions are classified according to the dominant loss processes discussed in section 2.5. The drop in potential at the activation region is typically exponential and mostly dominated by the sluggish kinetics of the oxygen reduction reaction [16]. The ohmic region exhibits a pseudo-linear line where the loss is mostly due to ohmic resistance at medium current densities. Beyond this region, the losses due to mass concentration and transport become prominent. The Tafel approximation in equation 2.16 offers a way to estimate the activation losses from the polarisation curve. With the assumption that the ohmic resistance is insignificant at low current densities, fitting the Tafel equation may be used to extract the exchange current density as well as the transfer coefficient parameters [3].

The polarisation curve may be recorded in both direction to also investigate drying or flooding behaviour. In the event of either of these, the forward and backward sweep measurements show some hysteresis [17]. In a flooding system for instance, the backward sweep may show reduced performance since the water formed in the forward sweep will inhibit the flow of

reactants as necessary. On the other hand, for a drying situation, the backward sweep may indicate a better performance since high current densities tend to draw more water which humidifies the membrane making for better performance.

The polarization curve is one simple way of fuel cell monitoring. It helps to describe the electrical performance of the system under different conditions and parameters. For this reason, it often finds use in manufacturing procedures for determining the operation point in addition to other techniques. Because the polarisation curve does not provide time dependent operating characteristics, its use as a diagnostic tool for a dynamic system like the fuel cell is limited. The waiting time required to ensure steady state for measurement also makes this technique time consuming. The steady-state time required tends to get larger for bigger systems and may even be up to 30 minutes for automotive scale fuel cell systems [3]. Determination of suitable steady state time required for polarisation curve measurement is usually a matter of conducting a series of polarisation curve measurements for different times until a time when the changes due to transient behaviour is non-significant [3]. The polarisation curve also interferes with the operation of the fuel cell and may not be carried out while the fuel cell system is being used.

3.2.2 Current Interrupt

For a dynamic system like the fuel cell, time dependent behaviour is key to understanding the internal processes. The current interrupt exposes some time dependent characteristics of the fuel cell. For a given step change, the current interrupt technique rapidly captures the transient behaviour up to the steady state instead of allowing for a steady state before making observation as is the case for the galvanostatic polarisation curve. By doing this, the time dependent characteristics of the fuel cell are retained in the measurement. The current interrupt technique applies a step current (increase or decrease) to the fuel cell system. Taking the voltage response to this applied signal reveals two conspicuous behaviour as illustrated in

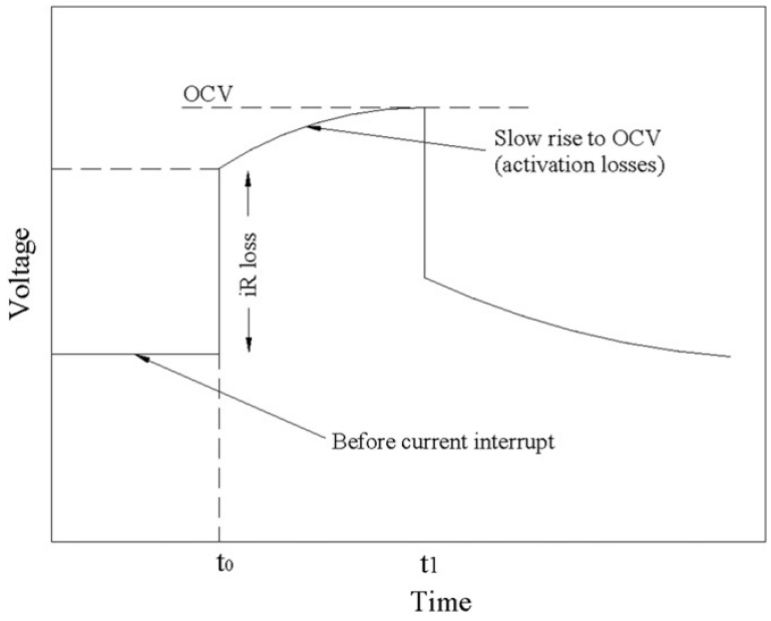

Fig. 3.4: Illustrates the voltage profile for the current interrupt technique. [1]

Fig. 3.4.

A sharp rise is immediately accompanied by a slowly rising curve similar to a charging capacitor. This sharp rise is indicative of a resistive component and has been identified to be the result of the ohmic losses while the capacitive behaviour captures the time dependent phenomena associated with mass transport and slower reaction processes [3].

The current interrupt may also be conducted alongside the polarisation curve by only including the necessary transient measurement step. This way, the current interrupt may be conducted for each step of the current which then gives the ohmic loss for each current set point for the system. By doing this, the ohmic component along the polarisation curve may be removed which will then allow for the isolation of the activation and concentration losses [3]. The current interrupt is typically simple to conduct, and it is an extremely fast measurement technique. Valid current interrupt measurement however requires rapid data acquisition in order to capture the transients [18]. Also, the interruption needs to be as close to an ideal step to avoid convolution of instantaneous and transient processes. According

to [19], timing for the current interrupt measurement should be controlled in the range of about 0.5 to 10ns.

3.2.3 Electrochemical Impedance Spectroscopy

Given the complex nature of the system, various electrochemical processes occurring exhibit interesting characteristics at various frequencies. An understanding of these processes is key to gaining relevant insight to the multi-physical processes in the fuel cell. Impedance spectroscopy is a popular tool in the electrochemical space for obtaining impedance data of a system under test across a range of frequencies [16]. The EIS is capable of isolating different characteristic processes that occur within the cell, essentially availing richer information for diagnostics than previously discussed diagnostics techniques. The process typically involves the excitation of the system under test with a sinusoidal signal. The sinusoid serves as a modulating signal over a DC current point in the case of a galvanostatic process, or a voltage point for the potentiostatic alternative. This is done for a wide range of frequencies of interest with the response measured as a voltage signal in the galvanostatic measurement and current signal for a potentiostatic measurement. To obtain the impedance, for a given frequency, the ratio of the voltage and current is calculated to give the complex impedance for the different frequencies according to Ohm's law as in equation (3.3).

$$z(\omega) = \frac{v(\omega)}{i(\omega)} \tag{3.3}$$

The Nyquist plot is often employed as a visual representation of the impedance data. It plots the decomposition of the complex impedance into its real part, z_{re} on the x-axis, and the imaginary part, z_{im} on the y-axis. To gain relevant insight from the impedance data, it is common to fit an equivalent electric circuit to the impedance data.

3.2.4 Other Characterization Techniques

Other electrochemical methods include the cyclic voltammetry achieved by sweeping the potential between two set points in order to characterise the catalyst activity of the electrochemical surface area (ECSA). The cathode discharge techniques also help to determine the resistance of the membrane electrode assembly and may be achieved by monitoring galvanostatic discharge of the fuel cell upon reactant supply interruption [16].

Since the fuel cell behaviour is dependent on multiple conditioning parameters, it may be useful to track these conditioning parameters as well. In addition to current and voltage measurements, other data may be collected especially for data driven information extraction stages. Such data may include temperature, pressure, flow-rate and humidity. These help to put other measurements in context and provide a richer set of information from which state of health knowledge could be derived.

3.3 Information Extraction for Fault Detection

An information extraction stage is often necessary to further diagnose the system, determining whether the data describes a faulty condition or not, and to what extent. Because of the nature of fuel cells, another important step is fault isolation. This is required to resolve the faulty conditions to the respective causes. The nature of the fuel cell however makes this latter stage difficult. Different degradation mechanisms and faulty conditions may often be a result of a combination of degradation processes. Also, it is not usually clear what processes or conditions constitute poor performance from data such as the polarisation curve analysis. These challenges have resulted in various research efforts aimed at analysing diagnostic data in an effort towards fault isolation. A variety of diagnostic procedures have been developed in literature. These procedures mostly involve techniques with roots in signal processing, and pattern recognition techniques such as machine learning. Others also involve the use of mathematical models requiring significant understanding of the system. Classifying these

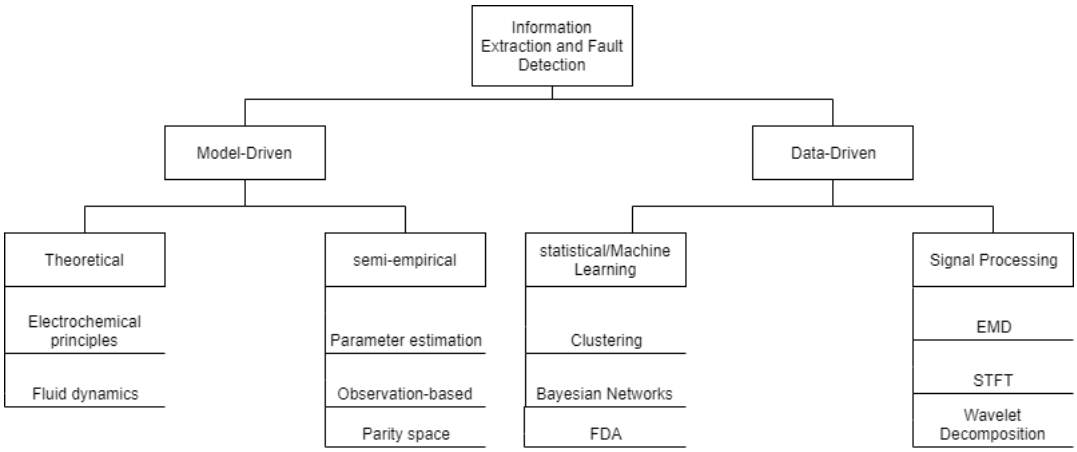

Fig. 3.5: Classification of fuel cell diagnostic techniques.

methods is not straightforward as the techniques involved often overlap on many bases. However, they will be discussed under two broad categories depending on the fundamental approach towards diagnostics - the model-driven and the data-driven models as shown in Fig. 3.5.

The following section will review various approaches under the two categories as it exists in literature. The techniques involved will be briefly discussed, while the merits as well as the challenges will also be highlighted.

3.3.1 Model Driven Diagnostics

In order to describe as well as predict the behaviour of the fuel cell system, a model of the system may be developed. This requires an understanding of the physics of the internal processes. Mathematical models which could predict the behaviour of the system are developed with knowledge of system characteristics and understanding of mechanisms by which faulty conditions proceed. Models may be derived from first principles, i.e. from fundamental electrochemical principles such as Butler-Volmer and Fick's laws, or via test data [20]. These models essentially give the input-output relationship for the fuel cell system. Physics of failure models that employ knowledge of the degradation mechanisms may also be used to

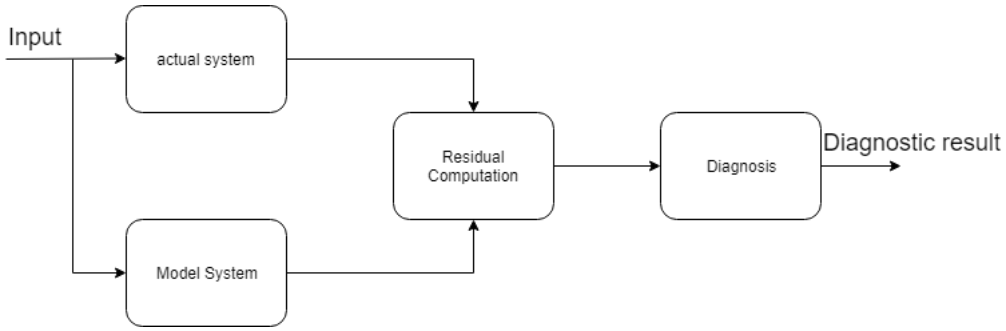

Fig. 3.6: Schematic illustrating the model-driven diagnostic technique

specifically target fault conditions.

In order to test validity of models, the outputs of the models are compared to the output from the real system for varying conditions using well established measurement techniques such as the polarisation curve and current interrupt techniques [20]. Because the behaviour of the system may now be known in advance, deviations from this signify an anomaly. Signals acquired from the fuel system may then be compared to the model predicted output. The difference between these - the residuals, may then be analysed for probable fault conditions and to further understand the cause and the degree of faults [21]. This is as shown in Fig. 3.6 illustrating the model-based fuel cell diagnostic technique where the behaviour of the actual system is compared to a representative model and diagnostic information is derived from residuals. This typical modelling representation for the residuals $r(t)$ for a given input set of conditions $x(t)$ and output $y(t)$, for a given time t, may be expressed as follows;

$$r(t) = f(x(t),\ y(t)) \tag{3.4}$$

Where $f(x,y)$ is a function that determines the residual from the input output parameters. Fig. 3.6 illustrates the process for the model-based diagnostic approach.

The model-driven method has been applied for the diagnosis of fuel cell system faults [22–24]. Subspace identification methods such as the linear covariate analysis, have been used to model the input-output relationship of the fuel cell for diagnostics [24]. Diagnosis of

system faults such as temperature by incorporating a residual fault sensitivity technique has also been presented [23]. While model-based methods may give clear insights to the system behaviour, these methods do require significant knowledge of the physics of internal processes. Also, due to the inherent complexity, they often demand significant computational power in application [23].

3.3.2 Data-Driven Diagnostics

Developing a mechanistic approach in the form of a descriptive model is a challenge since the complexity immediately becomes prohibitive for real-life applications. To address this, several data-driven methods that effectively learn the mapping which describe the characteristic behaviour of the system have been developed. These so called black-box methods do not necessarily make use of understanding of the system to develop the models [25]. The underlying concept for data driven diagnostics is the assumption on the statistical behaviour of the fuel cell. It is assumed that under some certain variables, the behaviour of the system as provided by generated data should be operated within certain limits. Outside of these limits, a fault is probable. The distribution of the data therefore provides knowledge of the system behaviour for a given time under given conditions. Because data driven techniques do not require the use of complicated physical models, but makes use of data derived from the system, they tend to be easily implemented and computationally efficient [25], hence their popularity for fuel cell diagnostics.

Machine learning methods such as neural networks [26], and clustering [27] have been applied for the diagnosis of faults. Machine learning methods may generally be classified into supervised and unsupervised learning. The distinguishing feature is the availability of a labelled response in the supervised approaches unlike the unsupervised ones where the target label is unknown. The presence of labelled targets for the supervised learning approaches makes it easy to evaluate their performance, making them more popular than unsupervised ones. Supervised learning methods generally involve an initial exploratory

analysis of the data in order to determine relevant features. These features form a design matrix that is then used to train a learning algorithm. The data is split into a training and test sets. The training data is used to train the learning algorithm which effectively learns a mapping function between the features and the label. The test data is then used as a means for scoring and diagnosing the trained model for some accuracy metric. The trained model may now be applied to new data points for the prediction of a target such as diagnostic phenomena.

Extraction of feature data form EIS results to diagnose faults including low and high air supply amounts, high CO (carbon-monoxides) concentration, and high and low H_2 supply faults was demonstrated by [28]. An accuracy of 94.5% was recorded with subsequent implementation of artificial neural networks for fault isolation. Data extracted from EIS measurement together with the supervised method - K-nearest neighbour (KNN) for classification of fault conditions was presented in [29]. Fault conditions considered include air supply, overheating, and short-circuit and a classification accuracy of 92% was reported. Similar works also include [30] and [31]. Unsupervised methods such as principal component analysis (PCA) have been employed for dimensionality reduction of data collected for diagnostics to improve computation speed [28]. Online learning approaches have also been proposed [32, 33] to ensure that models are updated in accordance to temporal behaviour. This is important for continuous monitoring of system with natural degradation over time.

Statistical methods are closely related to the machine learning approaches. Examples of these include the Fisher Discriminant Analysis (FDA) and the Bayesian Networks (BN). The FDA seeks to find discriminant vectors that minimize intra-class distances while maximizing inter-class distance among categorical observations [34]. The use of the FDA has also been demonstrated [35]. BN represent probabilistic dependence relationships between different variables. In this sense they have been used to model the relationship between observable effects and faults for a fuel cell system [36].

Signal processing techniques in fuel cell diagnostics are not far removed from the statistical and machine learning techniques. They have shown promise in the analysis of current and voltage data. Two major considerations for the signal processing techniques are the signal to monitor for diagnostics and the analysis techniques to be deployed [37]. The fuel cell voltage data is highly relevant to its state of health. Expectedly, most faulty conditions result in some level of voltage drop, and voltage data acquisition for the fuel cell is also an easy task. The measured voltage data from the fuel cell is inherently non-stationary. This makes signal analysis techniques like the discrete fourier transform unsuitable. To address this, time-frequency techniques such as the wavelet analysis have been employed. Wavelet packet decomposition technique has also been used to analyse voltage data, which enabled the diagnosis of flooding issues with results shown for a fuel cell stack [38]. Comparison of coefficients obtained from the discrete wavelet transform applied to voltage data for different conditions has also been explored [39]. This allowed ruling on high air stoichiometry conditions. The separation of electrochemical noise from other signal noise source was then useful for investigating phenomena such as flooding [40]. Time domain techniques that also allow the breakdown of voltage signal into different components such as the Empirical Mode Decomposition (EMD) have also been employed. The EMD decomposes signals into component signals which consists of a finite number of intrinsic mode function. This technique has been employed in the diagnosis of flooding and drying fault scenarios [41].

While data driven techniques have shown promise, for fuel cell diagnostics, much work is still required to further develop these approaches. Data driven techniques often require large datasets that are not available. These techniques require data under both healthy and faulty conditions. More specifically, prior information required to learn faulty conditions for some algorithms are rare. Since the accuracy of data driven approaches is tied to the quality and quantity of available data, this is a significant challenge. An example is the case of a new system with little or no data is available. These methods also tend not to generalize to different systems making them only best for use with system that generated the data on which the models have been trained [42]. Some diagnostic approaches also employ a so-called

grey-box approach in which data driven approaches are combined with model-driven ones to take advantage of both [20].

3.3.3 Impedance Spectroscopy Analysis for Fuel Cell Diagnostics

The EIS measurement has proved a popular technique for fuel cell characterisation as well as diagnostics as is evident in literature [28, 27, 60]. The popularity of the measurement technique is due in part to the fact that it provides more useful information on the state of health of the fuel cell compared to other techniques such as the current interrupt and polarisation curve. As a frequency-based measurement, it has shown suitability in capturing the dynamic characteristic of the fuel cell.

EIS has also been combined with data-driven approaches for diagnostics. The EIS is however a complex measurement with a number of conditions to be met in order to ensure accuracy. In this section, some of the important conditions identified in literature are considered. Electrical equivalent circuit modelling forms a part of most fuel cell EIS characterisation procedure. The various models employed in literature are also reviewed and some of the applications of EIS in fuel cell diagnostics are then discussed.

3.3.4 Measurement Consideration

The EIS measurement can be conceptualized essentially as a system identification technique. For a dynamic systems like the fuel cell, a frequency response characteristic is desired and the EIS provides a means to achieve this. Typically, this is achieved by perturbing the system about an operating point. Conventionally, the perturbation is achieved with a sinusoid of known frequency. This is repeated for several other frequencies to yield points that approximate a spectrum. The perturbation as well as the response signals are collected and the DFT computed using the FFT algorithm to get the complex coefficients for the corresponding frequency. The impedance is derived by taking the ratio of the complex

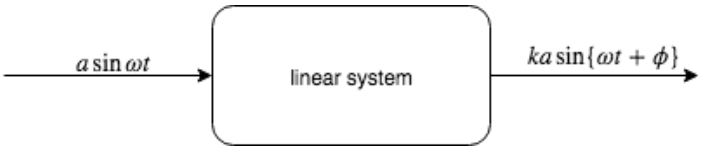

Fig. 3.7: Response of a linear system to sinusoidal input.

voltage and current as in equation (3.5).

$$z = \frac{FFT(v)}{FFT(i)} \tag{3.5}$$

This processing approach for the input and response makes some assumption on the system. The invocation of Ohm's law in the computation of impedance assumes the linearity of the fuel cell system. For a linear system, the response to a sinusoidal input is a sinusoidal output of the same frequency [43]. This is illustrated in Fig. 3.7.
For the fuel cell however, this is hardly the case. The Butler-Volmer kinetic relations explicitly state a non-linear relationship between the current and the fuel cell activation (potential drop). In addition, system nonlinearities are further pronounced in the event of anomalous conditions such as flooding [42].

Specifically, impedance may only be defined this way provided the conditions of linearity, causality and time-invariance are observed [44]. It has been shown that the impedance for a non-linear electrical system was dependent on the perturbation amplitude [45]. The effect of the kinetic parameters and electrode potential on the linearity of the system has been further highlighted [46]. To avoid these scenarios, it is noted that the amplitude of the perturbation should be made small enough to achieve quasi-linearity [47]. This idea has been observed in several works with an amplitude of about 5% of the DC point generally recommended for galvanostatic EIS [48]. This was investigated employing the total harmonic distortion measure to seek an optimal amplitude with considerations for the Signal-to-Noise ratio [48].

The fuel cell system also exhibits non-stationary behaviour. The time invariance requires that the response remains unchanged to a given perturbation signal over time [44]. Fuel

cell EIS typically requires measurements at low frequencies. This requires measurement times long enough for the system to change. It has been shown that this results in a time dependent impedance measurement which complicates analysis [49]. Reducing the timing of the measurement is one way to mitigate this and this has been the focus of many research works seeking to use advanced signals that involve shorter measurement times [50, 51]. While these have proved effective in time reduction of the procedure, some new challenges are introduced. Part of the focus of this thesis is to investigate this as will be shown later.

In addition to these principal considerations, other challenges with the measurement may include precision of the instrumentation and improper setting up of electrodes [52]. Theoretically, the Kramers Kronig (K-K) transform may be used to validate collected impedance data. The K-K transform relates the real and imaginary impedance components [53]. It is noted, that for non-linear response to large perturbation, the K-K relations fail to give a good measure of error and recommends an experimental approach [54].

3.3.5 Electrical Equivalent Circuit

EIS data is often modelled with electrical equivalent circuit (EEC) models. Circuit elements employed typically include resistors, capacitors, and inductors. Other elements include the Warburg and constant phase elements (CPE) which help to model special characteristics of the fuel cell impedance. Model circuits formed with these elements may be used to determine the performance of the fuel cell [55]. It is however important that the elements chosen correspond to the actual characteristic processes of the fuel cell [3].

Given impedance data and an appropriately chosen circuit model, values of the constituent elements of the circuit may be approximated via a non-linear least square technique [56]. Measure of error such as chi-square are used to evaluate the suitability of the resulting circuit fit. A simple and popular model circuit for most electrochemical system including the fuel cell is the Randles equivalent circuit as illustrated in Fig. 3.8. This is often employed as a starting point for most fuel cell impedance fitting. In its simplest form, it consists of a

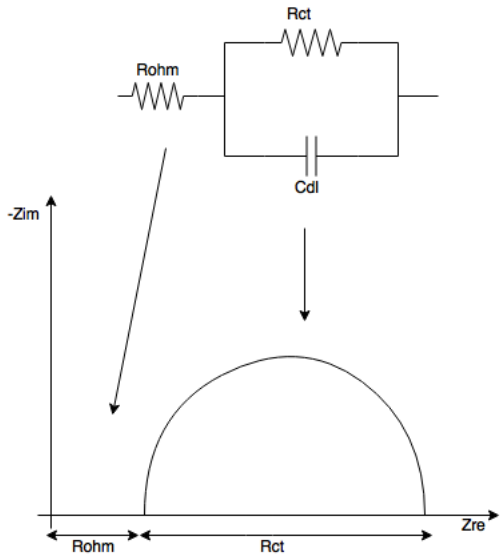

Fig. 3.8: Randles Equivalent Circuit and Corresponding Nyquist plot.

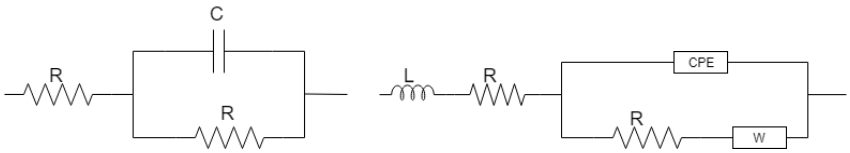

Fig. 3.9: The simple Randles equivalent circuit (a) and the modified Randles equivalent (b)

resistance in series with a parallel combination of a resistor and capacitor [1]. The resistance R_{ohm} captures the ohmic resistance of the electrolyte while R_{ct} represents the opposition to the charge transfer process in the cell. The C_{dl} represents the capacitance due to the double layer formed. In some cases where the inductance due to connectors is significant, it may be necessary to include an inductance in series with the ohmic resistance. Many more complicated circuits are also used to model more complex processes such as the diffusion mechanics also with data provided by the impedance information [1].

The Nyquist plot for a fuel cell is often not a perfect semicircle. A depressed semicircle may not be modelled with a just capacitors and resistors configurations. This behaviour may be attributed to the porous structure of the electrode and its electrical heterogeneity [57]. To model such behaviour, the capacitor may be replace by a constant phase element (CPE). the

impedance of the CPE is given in equation (3.6).

$$z_{CPE} = \frac{1}{j^n Q_0 \omega^n} = \frac{-j^n}{Q_0 \omega^n} = \frac{1}{Q_0 (j\omega)^n} \tag{3.6}$$

Where the Q_0 and n are frequency dependent and are the variable parameter with n in the range [0,1] [57]. The CPE generalizes the behaviour of the resistor and capacitor with $n = 0$ and 1 describing the ideal resistor and capacitor respectively. The Warburg element helps to model mass transport issues in the fuel cell. For a finite diffusion exhibited by the fuel cell, the impedance of the Warburg may be represented as in equation (3.7).

$$z_w = R.\frac{\tanh(j.T_w.\omega)^\Psi}{(j.T_w.\omega)^\Psi} \tag{3.7}$$

While it is possible to fit a highly complicated circuit over the impedance data with high accuracy, care must be taken to ensure that circuit elements reference corresponding physico-chemical processes of the actual fuel cell system. A number of circuits have been proposed such as in [58, 56, 42]. Separate circuits models were proposed for high and low current operations and validated using simulation and experimental data [56]. A novel configuration has also been presented, with additional resonant loops on the cathode and anode side [56]. The proposed model was experimentally verified and accounted for the low-frequency inductive phenomena.

The various parameter values extracted from the equivalent circuit fit provided useful information for different conditions in the form of varying circuit parameters. These can then be used to characterize as well as understand the behaviour of the system for varying conditions. The use of EEC has been demonstrated in the study of faults such as Phosphoric Acid loss and CO-poisoning by monitoring equivalent circuit parameter changes [42]. In studying the

oxygen reduction process and the methanol oxidation process at the cathode, a circuit with the capacitance and the charge transfer resistance taking into consideration the double layer of the oxygen reduction process has been proposed [59].

Some procedures for analysing impedance data such as dealing with outliers and smoothening of the impedance plot are laid out in [44]. Smoothing is justified for most impedance data since a smooth curve is generally expected [44]. The Complex non-linear Least Square (CNLS) is popular for fitting circuit models to impedance data. Unlike other existing methods, the CNLS makes use of all the data points at each iterative step. In addition, it enables the fitting of complex models with multiple circuit elements while providing a measure of uncertainty for the estimated parameters [44]. The chi-square (χ^2) value is often used to define the goodness of fit which is related to the suitability of the resulting circuit fit.

Going by existing literature, it is noted that various EEC models have been employed. Modifications are often made as necessary to account for special characteristics. Also prior knowledge of internal characteristics of the system in question informs necessary modifications.

3.4 Conclusion

This chapter presents a review of the various diagnostics and condition monitoring techniques. Standard electrochemical methods, some of which are employed throughout this work are first reviewed. A detailed study of information extraction techniques is also presented and divided into the model-driven and the data-driven techniques. As a popular technique, the EIS measurement technique is investigated. The various measurement considerations required for a valid EIS measurement are presented. The use of electrical equivalent circuit for modelling impedance data is also discussed. Advantages and disadvantages of the different diagnostic techniques are also noted and form the basis for further research which this thesis focuses on.

Chapter 4

Experimental Setup and Procedures

4.1 Introduction

In order to test various techniques proposed in this work, tests are carried out on a single cell test station. Throughout this work, some standard electrochemical methods, including the polarisation analysis and the EIS are carried out. The rest of this chapter describes the single cell fuel cell used throughout this work. Key components and relevant parameters are highlighted, and the different test procedures are presented. As earlier noted, initial conditioning is necessary in order to ensure stable measurements. The conditioning procedure implemented for all tests is described. Finally, the procedure for initiating fault conditions studied in this work is detailed.

4.2 Fuel Cell Assembly

Experiments were conducted on a single cell fuel cell system. The fuel cell assembly consists of a single cell system with an active area of $25cm^2$. The innermost layer consists of the membrane lying between the anode and cathode to constitute the membrane electrode assembly (MEA). Fig. 4.1 shows the constituent parts of the MEA - anode, membrane and cathode. The MEA is sandwiched between the graphite bipolar plates which is shown in Fig. 4.2. Current collectors form the next layer and the whole assembly is enclosed in an

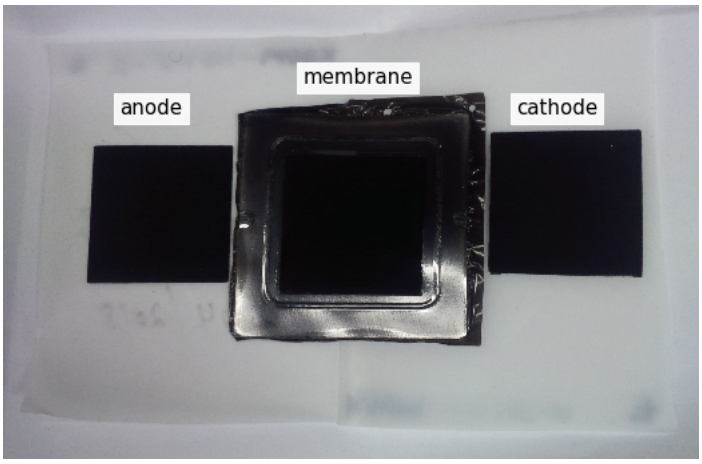

Fig. 4.1: The three components that constitute the membrane electrode assembly - anode, membrane and cathode.

outer casing which is insulated from the current collector plates.

The fuel cell assembly is connected to a Fuelcon test station enables supervisory control and allows continuous monitoring of fuel cell conditions during testing. The test station also allows for automated testing via an application programming interface. Other components included in the test station consists are gas humidifiers, heating and cooling channels, mass flow controllers for both the incoming reactant gases as well as the exhaust gases.

Also housed in the test station is a potentiostat/galvanostat and an impedance analyser with leads which are firmly connected to the current collector's positive and negative plates. The mass flow controllers allow for the control of the fuel in accordance to set flow-rate or stoichiometry. Air is fed in at the cathode while Hydrogen is fed in at the anode. Humidifiers help to maintain the required level of humidity with the action of the bubblers. A temperature sensor inserted into a hole in the fuel cell assembly helps to monitor the temperature. For temperature control, the assembly is heated with the use of heating plugs attached to the assembly body. A fan is also positioned close to the set-up to provide cooling. In setting up, the flow pipes were thermally insulated to ensure the set temperature of the incoming gases is maintained along the flow channels upon entry into the fuel cell assembly.

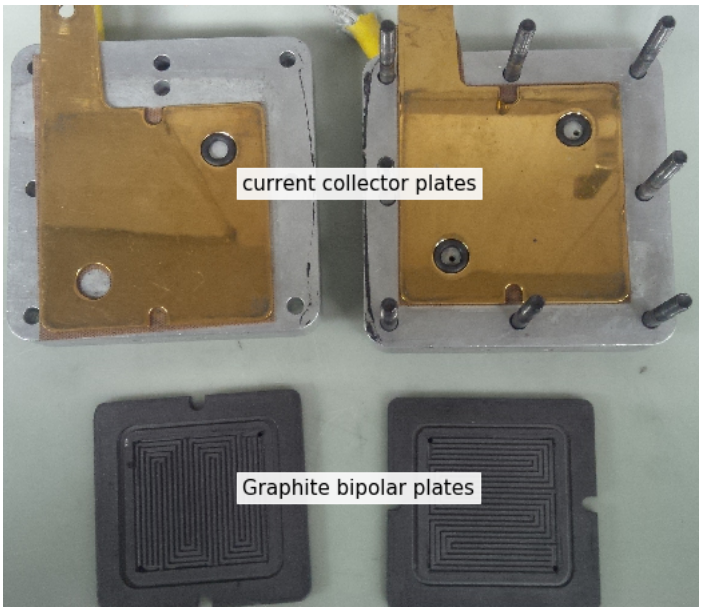

Fig. 4.2: The current collector and graphite bipolar plates.

4.3 Test Conditions

As earlier noted, test conditions have significant impact on the performance of the fuel cell. For this work, some parameters were varied while others were kept constant. This section details standard parameter values set under normal operation. When these change, it is explicitly stated.

The stoichiometry of the anode and cathode was set at 1.5 and 2 respectively. To maintain this stoichiometry, the flow rate is dynamically controlled for a given current set-point using the following relations;

$$\text{anode-flow rate} = \frac{i}{nF} \times V_0 mol \times 60 \tag{4.1}$$

$$\text{cathode-flow rate} = \frac{i}{nF} \times V_0 mol \times 60 \times \frac{1}{0.21} \tag{4.2}$$

where i is the current, n is the amount of electrons exchanged, F is the Faraday constant, V_0 is the molar gas volume at standard temperature and pressure. The airflow rate is scaled

Table 4.1: Table of parameter values for fuel cell test

Parameter	value
Anode stoichiometry	1.5
Minimum Hydrogen flow	$0.15Nl/min$
Minimum Oxidant flow	$0.53Nl/min$
Cathode stoichiometry	2
Maximum current	$45A$
Minimum voltage	$0.35V$
Stabilisation period	$30s$
Repeat readings	3
Activation Increment	$1A$
Ohmic increment	$3A$
Rest time	$10s$
Humidity	100%
Temperature	80^0C

by 0.21 which accounts for the molar fraction of O_2 in air. A minimum hydrogen flow of 0.15 and oxidant flow of 0.53 is maintained for all tests to prevent a zero flow rate which may result in damage of the membrane. The temperature is set at 80°C for the tests which is in accordance to membrane manufacturer's recommendation. The table 4.1 summarises the parameter values.

4.4 Conditioning

It has been mentioned in chapter 3 that initial conditioning is necessary to ensure the fuel cell system equilibrium in operating conditions. This helps to minimize non-steady state behaviour [3]. Prior to carrying out tests, the conditioning procedure is first run as an initiating procedure. For this work, the cyclic conditioning has been recommended by the membrane manufacturers.

To commence conditioning, the Hydrogen flow-rate is initially set to 0.15Nl/min and the air supply set at 0.5Nl/min. Humidification then starts with the anode and cathode flow through

Fig. 4.3: The experimental conditioning procedure.

the bubblers. To avoid a temperature increase, the air flow rate is slightly reduced before turning on the humidifiers. The flow rate for the anode and cathode are set to equivalent values for a current density of $1200 mA/cm^2$ for a given stoichiometric ratio of 1.5 (anode) to 2 (cathode). This set point is approached in small increments of 0.05 to avoid possible overshoot. With the flow rates set for both the anode and cathode, the fuel cell voltage is then cycled between 0.8V and 0.3V using the electronic load. The potential is maintained at 0.8V for 30 seconds, and for 60 seconds at 0.3V. This is repeated 12 times after which the voltage is set to 0.8V. Because this procedure results in an increase in the temperature of the cell, a 5-minute period is allowed for the stabilization of the temperature before tests are carried out.

4.5 Standard Electrochemical Test Procedures

Electrochemical tests such as the polarization curve and EIS form part of standard electrochemical procedures and are employed extensively in this study. The procedures followed in these tests are discussed in this section.

4.5.1 Polarisation Curve

The polarisation curve test serves as a simple measurement to evaluate the overall performance of the fuel cell. In this work, it serves the purpose of characterising the system used in order to understand factors such as limit in current density to prevent damage to the cell. Polarisation curves are compared for various tests carried out in order to observe possible changes to the fuel cell performance due to the other procedures undertaken.

The procedure begins with the load disconnected. The valves are opened, and the minimum flow rate is then set for the anode and cathode sides. The load is connected and a small amount of current (2.5A) is drawn. At this point, the cell temperature control is activated. The current is reduced to zero and some time allowed for the fuel cell to return to open circuit voltage (OCV). The OCV is read to start the current step process during which the current is increased in small increments and the corresponding voltage read.

Changes in potential occur relatively rapidly at the activation region. In order to improve the resolution in this region, shorter step sizes of 1A are used, while a step size of 3A is used in the linear ohmic region. A wait period of 30 seconds is allowed between consecutive measurement to ensure steady state readings are made. Also, three voltage readings are acquired for each current set-point and the average of these is recorded as an added measure of reliability. For given current, the corresponding flow-rate is set in accordance to the set stoichiometric ratio using the following equation (4.1) and (4.2).

A maximum current and minimum voltage of 45A and 0.35V respectively are set as limits to signal the termination of current increase. The current is increased until one of two termination conditions are met. For the first, a maximum current limit is set and it is determined if the next step exceeds this maximum value as in equation (4.3). The second condition subtracts the previous potential drop due to the current step from the current potential and compares this with the minimum voltage value as shown in equation (4.4). The

measurement is terminated if the resulting value is less than 0.35.

$$i + i_{increment} \leq i_{max} \tag{4.3}$$

$$v - (v_0 - v) < V_{min} \tag{4.4}$$

4.5.2 Electrochemical Impedance Spectroscopy

The standard EIS measurement is carried out on the test station with the aid of an in-built impedance spectrum analyser which controls an external electronic load. Conditions set for the EIS measurements are similar to those of the polarisation curve. Measurements are carried out at a given current set point. With the flow rates, pressure, humidity and temperature set, the current is increased gradually by the electronic load until the desired set point is reached. The system is perturbed with sinusoidal frequency points from a logarithmic distribution. 4 periods of each sinusoidal perturbation are allowed for improved accuracy. Except otherwise stated, the frequency range of deployed is 0.1-10kHz.

4.6 Fault Emulation

The fuel cell is prone to various faulty conditions as previously discussed. Prominent among these are the flooding and drying faults. Other known faults such as starving and membrane degradation mechanisms often occur as a result of flooding and drying. A number of activities that result in flooding have been laid out in [7]. First, flooding may result from condensation of humidified gaseous reactants. Also, the product water forming at the cathode may also result in flooding when not properly managed. Proton transport across the membrane also results in electro-osmotic drag which in turn results in an accumulation of water. Drying occurs when there is relatively low water content in the cell. This also leads to degradation

of cell components when not timely addressed.

In the course of experiments, care is taken to establish a reference point by operating the fuel cell under standard conditions and carrying out standardized tests such as the EIS and polarisation curve. This ensures that comparisons could be made between results without confounding the effects. As an example, in the case of a flooding condition, EIS results and Polarisation curve show distinguishable results from results achieved under normal operation. In some case, drying of the bipolar plate becomes necessary to completely reverse the effect of flooding.

4.6.1 Flooding Procedure

A procedure for emulating a flooding condition was described in [60]. This procedure is used as a guide and compared to other results found in literature as well as experimental observations which will be further discussed. To realize, the initial cell conditioning procedure as discussed above is first run. The system is then allowed to operate under predetermined standard conditions for a few minutes for a constant current of approximately 10A. In order to initiate the flooding condition on a test fuel cell, the system humidifier on the anode and cathode side is set to be higher than the fuel cell temperature. The result is that more water is absorbed in the incoming gaseous reactant at higher temperature. The result is a temperature gradient which allows condensation to happen rather rapidly upon reaching the fuel cell where the temperature is relatively lower. In this case, the humidifier heater temperature on either electrode side is gradually increased to 100°C while the fuel cell temperature is maintained at 75°C. Other conditions such as the pressure are maintained. The cell is also run at high current which necessitate higher electroosmotic drags, further enabling a flooding condition as necessary.

4.6.2 Drying Procedure

The drying procedure also employs the humidifier temperatures to achieve the desired results. Having less water in the cell than normal will result in a drying fault The system is first allowed to run under standard operational conditions for a few minutes after conditioning. The humidifier temperature is set to a temperature of 55°C while the cell temperature is maintained at 80°C. This results in less absorbed water by the incoming gaseous reactant. The relatively higher temperature in the cell causes a drying as a result of low water content. The current is also reduced as necessary to enforce a drying condition.

4.7 Conclusion

The standard experimental procedure and operational parameters have been presented in this chapter. Details of the fuel cell assembly used throughout this work are also discussed. The procedure for realising the different fault conditions investigated in this work are also presented.

Chapter 5

Design and Implementation of an Active Load for Fuel Cell Impedance Measurement

5.1 Introduction

Implementing the impedance spectroscopic measurement may be carried out in a number of ways. These all aim to inject the sinusoidal perturbations at the required frequencies, while the response of the device under test is measured. As discussed earlier, this perturbation signal could be a current or a voltage signal. This section however focuses on the use of a current signal for reasons already stated.

One way the fuel cell impedance spectroscopy is often carried out is with the aid of expensive frequency response analyser equipment. The frequency response analysers are deployed in the laboratories to interface with the cell for carrying out measurements. The cost of such set-up has however hindered the use of EIS for more practicable purposes. Also because these test stations systems tend to be large, incorporating them into an actual system would mean a low energy-volume density for the overall fuel cell system. In addition to these constraints, some of the laboratory test system do not offer the flexibility for carrying varying

test. This makes it difficult to implement proven advanced impedance spectroscopy measurements using specially designed signals. Another popular approach is the use of commercial electronic load equipment. This receives a transient signal serving as the perturbation from a signal source while interfacing with the device under test (DUT). The drawback of this approach lies in the amplitude and frequency requirement of the perturbation which may be above permissible limits of typical laboratory devices. This is in addition to the size of this laboratory equipment.

This chapter details the implementation of an active dynamic load for impedance spectroscopic measurement. To achieve this, a current source is implemented. The active load as a current source allows to set an instantaneous transient current at any point allowing for the simulation of a wide range of load profile. The remainder of this chapter proceeds with the design of the proposed system. It starts with a detailed functional description of the proposed system and introduces the load modulation technique. The circuit is developed, analysed and simulated and appropriate behaviours are described with tests carried out on equivalent circuits and on an actual fuel cell.

5.2 Functional Principle

The goal of the EIS is to derive the impedance response of a given system over a desired spectrum. This may be achieved by injecting the sinusoidal signals for selected frequencies within the desired frequency range. The signal input may be achieved by implementing a current pump or a current sink. To ensure an output current signal independent of the load, a current pump implementation will theoretically require an infinite output impedance to ensure the integrity of the output signal. This poses a challenge for portable practical implementations. For the fuel cell which requires frequencies in the kilohertz range, the challenge is further pronounced as the output impedance of most current pumps get attenuated at high frequencies. Much effort has been put forward to achieve this, such as the

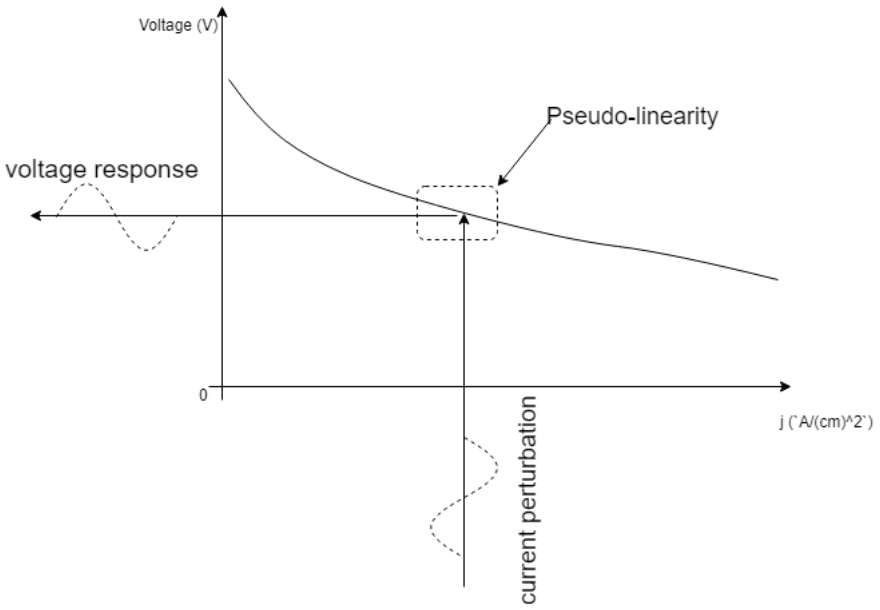

Fig. 5.1: The small signal perturbation and response illustrated on a polarisation curve.

Howland circuits [61], but they often require complicated circuits as well as high precision components to ensure an output current independent of the load [62]. The current sinking approach on the other hand, allows for more flexibility with the use of low-cost equipment. Also, for the fuel cell application, an operation point is often desired for measurement and diagnostic purposes. This is easily achieved in a current sink configuration. For these reasons, a current-sink implementation has been chosen in this design.

In the configuration, impedance spectroscopy is achieved by a load modulation technique. The load modulation provides a way to implement the EIS technique for a given cell operation point as illustrated in Fig. 5.1. Figure 5.2 below shows the overall system set-up.

The DUT is represented as a voltage source with its associated impedance. This represents the fuel cell stack system to be tested and is interfaced with the active load which draws an instantaneous current. The current drawn by the active load is determined by the input signal to the active load which is the perturbation signal offset by the required DC point. The input and the output signals may then be acquired as shown for further processing. The input (current), i, and response (voltage), v signal may be represented in terms of the DC, I, and

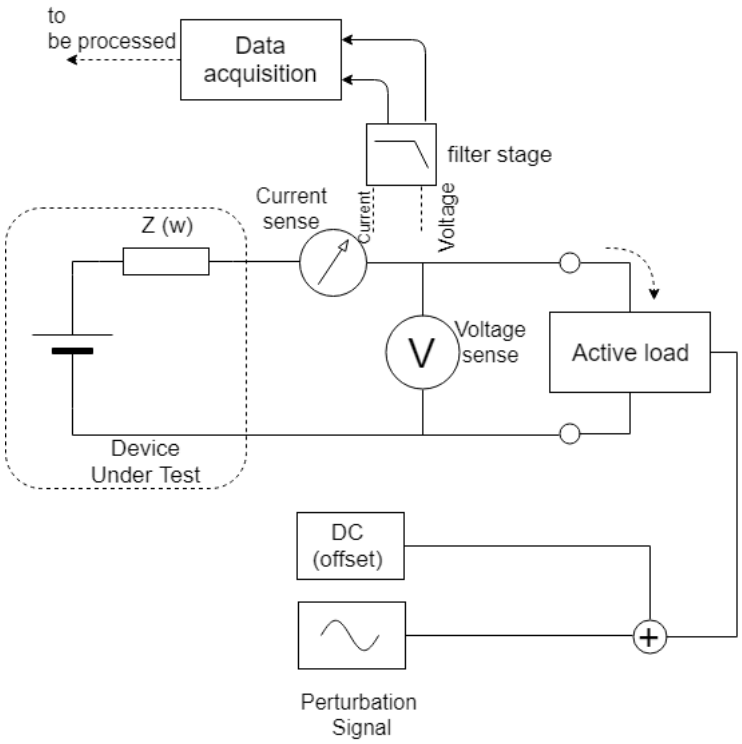

Fig. 5.2: Schematic describing the load modulation setup for impedance measurement of a device under test (DUT).

modulating signal Δi as in (5.1).

$$\text{current, } i = I + \Delta i \tag{5.1}$$

Particularly, the technique is achieved by implementing a wideband voltage controlled system. The active load helps to modulate a DC load operating point of the cell with sinusoidal waveforms of desired frequencies.

For the derivation of impedance for a linear system, the Ohm's law may be applied for the voltage and current signals. This however requires linearity of the system in question. The fuel cell is an inherently nonlinear system. To achieve linearity, a small signal approximation is necessary. This is expressed in the following equations, given the relationship;

$$v = f(i) \tag{5.2}$$

The Taylor's expansion around the operation point I may be expressed as:

$$v = f(i) = f(I) + \left.\frac{df}{di}\right|_I \Delta i + \left.\frac{1}{2!}\frac{d^2 f}{di^2}\right|_I (\Delta i)^2 + \ldots \tag{5.3}$$

Since $v = V + \Delta v$ and $f(I) = V$,

$$v = V + \Delta v = V + \left.\frac{df}{di}\right|_I \Delta i + \left.\frac{1}{2!}\frac{d^2 f}{di^2}\right|_I (\Delta i)^2 + \ldots \tag{5.4}$$

We may ignore higher order terms for small values of Δi to give:

$$\Delta v = \left.\frac{df}{di}\right|_I \Delta i \tag{5.5}$$

This yields the desired relationship and the impedance may then be calculated as follows:

$$\frac{\Delta v}{\Delta i} = \left.\frac{df}{di}\right|_I = z \tag{5.6}$$

The sinusoidal perturbation needs to be of low amplitude to satisfy the linearity requirements for the impedance calculation using the Ohm's law. Other issues relating to the amplitude as it affects the EIS measurement specific to the fuel cell are discussed in subsequent sections.

5.3 System Design of the Active Wide-Band Load

The active load is required to interface the DUT as a controlled load system. For the proposed system, a voltage controlled current source topology is adopted.

5.3.1 Current Source Design

To realize the load modulation technique, a wideband voltage controlled current source is designed. A bandwidth at least 10kHz which allows the typical fuel cell impedance information is also desired.

The schematic shown describes the characteristics of the voltage controlled current source system. The current i on the right-hand side of Fig. 5.3 is a function of the input voltage v_{GS}.

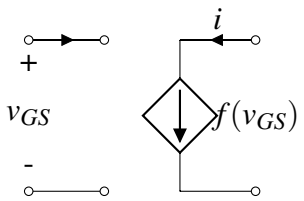

Fig. 5.3: Voltage controlled current source showing the dependence of the current on the input voltage.

As shown in Fig. 5.4, describing the current-voltage characteristics of the MOSFET, two major regions may be identified. The triode region describes the linear relationship between the drain-to-source voltage, v_{DS} and the drain-to-source current, i_{DS}, with the on-resistance R_{on} as the proportionality constant. As the drain-to-source voltage (V_{ds}) approaches the voltage difference between V_{gs} and the threshold voltage, V_T, the gradient of the $i-v$ curve

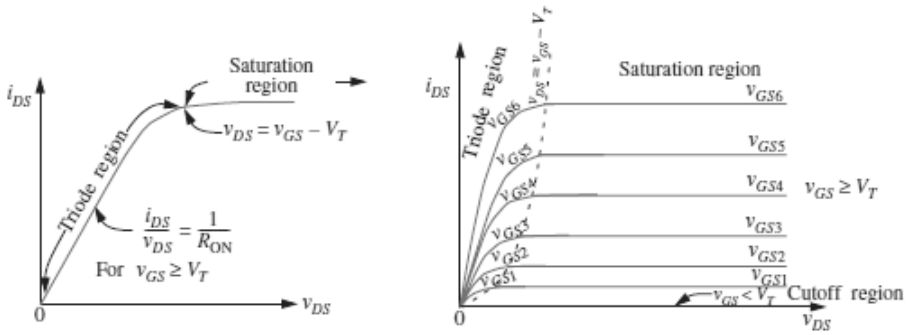

(a): Illustrating MOSFET triode and saturation characteristics

(b): MOSFET characteristics showing the three major regions - the triode, saturation, and cutoff regions

Fig. 5.4: MOSFET drain-to-source current voltage characteristics [5].

approaches zero rapidly. At this point, the current increases no further even with an increase in V_{ds}. At this stage, the MOSFET is said to be in saturation region. This region is key to the constant current operation required independent of changes to V_{ds}. Further increase in the V_{ds} leaves i_{ds} unchanged as shown in Fig. 5.4.

This controlled current characteristics is therefore achieved by operating the MOSFET in its saturation region. The conditions under which this occurs is given in equation (5.7) [5]. The drain current i_{DS} may then be controlled by the gate voltage.

$$i_{DS} = \frac{K(v_{GS} - V_T)^2}{2} \tag{5.7}$$

$$\text{for } v_{GS} \geq V_T \text{ and } v_{DS} \geq v_{GS} - V_T$$

From (5.7) above, i_{DS} which is the drain current is only dependent on the gate voltage v_{GS}. The threshold voltage V_T and constant K are characteristic of the MOSFET and are largely constant [5].

To achieve the required gate drive for an analog control, the MOSFET is located within a feedback loop to achieve linear control, as shown in the control block. The feedback

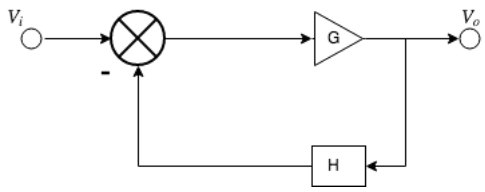

Fig. 5.5: Figure illustrating feedback loop.

sacrifices the high gain of the op-amp for more desirable characteristics such as the stability of the system. This effectively leaves the amplifier only subject to its external circuitry and not its material properties which may vary with factors such as temperature. Stable operation also necessitates negative feedback in order to keep the output current constant despite variations in the transistor parameters caused by manufacturing tolerances or temperature drift [63]. This makes it possible to set a required current equivalent to the device operation point. To achieve the current control, the feedback is made to sample a proportion of the signal of interest. In this design, the voltage across a sense resistor is fed back to make for voltage control. This affords the linear relationship between the desired signal and the control signal. Fig. 5.5 illustrates a simple feedback control loop. The loop transfer function is given as (5.8).

$$\frac{v_0}{v_i} = \frac{G}{1+GH} \tag{5.8}$$

For typical op-amps, the open loop gain G, is usually much larger than one. The above equation may therefore be approximated by (5.9) where H is the feedback gain.

$$\frac{v_0}{v_i} = \frac{1}{H} \tag{5.9}$$

The gain now obviously depends solely on the feedback gain and not G which may be dependent of variables such as temperature [64].

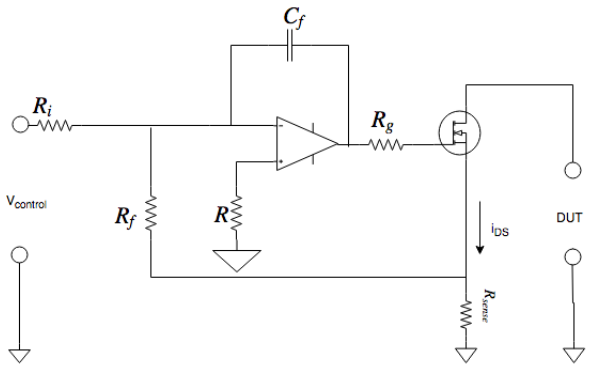

Fig. 5.6: Schematic of the controller stage showing the MOSFET located in the loop

5.3.2 DC Characteristics

The control circuitry is implemented as shown in Fig. 5.6 to achieve the initial proportional control. At low frequency, this circuit behaves as an inverting op-amp configuration(details in section A.2). The output is constantly sensed and compared to the desired output while the system responds accordingly to maintain the required output. In the diagram, the instantaneous input control voltage is constantly compared to the voltage across the sense resistor helping to set the MOSFET current drain. The control loop may be considered with the voltage across the sense resistor as the control output. The input-output relationship, $\frac{v_0}{v_i}$ may then be calculated. This results in the following (5.10).

$$\frac{v_0}{v_i} \approx \frac{R_f}{R_{in}} \tag{5.10}$$

Since v_0 is the voltage across the sense resistor, the current flowing through the source may be given as (5.11);

$$i_D = \frac{v_0}{R_{sense}} \tag{5.11}$$

In order to ensure a 1 : 1 equivalence between the control voltage v_{in} and the drain current i_D, the values of R_f and R_{in} are chosen according to the following; (5.12).

$$i_D = \frac{\frac{R_f}{R_in}.v_{in}}{R_{sense}} \tag{5.12}$$

A low resistance is desired for the sense resistor such that it may allow significant amount of current within the power rating constraint. R_f and R_{in} are then chosen such that the ratio is equal to the resistance R_{sense}. For a test on a single cell fuel cell, a load current of 10A is required to achieve a desired operation point. In order to limit the heat-sink size, two parallel arrangements are adopted to allow 5A for each MOSFET drain. Given the 1:1 relationship, input voltage of up to 5V is desired.

5.3.3 AC Characteristics

The perturbation signals required for the impedance spectroscopy measurement demands a wide bandwidth. Specifically, a frequency range of about 0.1Hz to 10kHz is required. Considering this, the choice of an op-amp with wide-band characteristics is required. Also, a feedback network exhibits frequency and amplitude dependent behaviour. For the required application, the frequency-dependent behaviour is a more stringent requirement and is therefore examined. The key to improving the approximation from equation (5.8) to (5.9) above is the product of GH. For the approximation to remain valid, it is necessary that this product is much greater than 1, as seen from the equation. However, because the op-amp effectively exhibits a low-pass filter characteristics, as shown in Fig. 5.7 for a typical op-amp, the value of G decreases with an increase in frequency.

This behaviour introduces some error in the behaviour of the feedback loop. One of the effects of this drop in the open loop gain is the lack of regulation between the input pins of the op-amp feedback, violating the virtual short assumption of the ideal op-amp [64]. We proceed to determine the overall loop response in order to determine the frequency characteristics of the loop. A method used to measure the loop gain as a function of the frequency via a signal injection approach in a feedback system is described in [6]. This affords

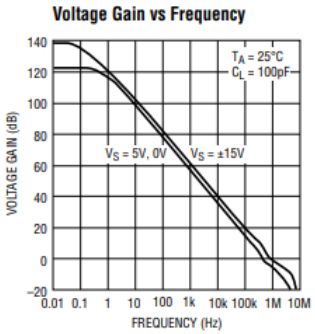

Fig. 5.7: Gain characteristics of the LT1014 op-amp.

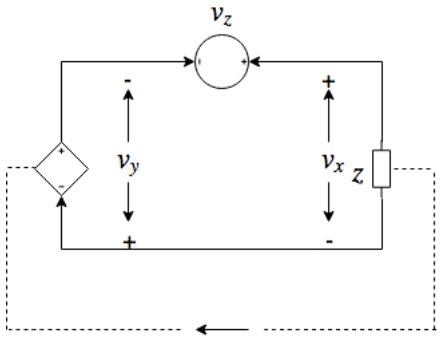

Fig. 5.8: Measurement of the loop response by signal injection into the closed loop (adapted from [6])

a way to realize the frequency response of the system using a test signal injected into the loop.

The measurement of the loop gain may be implemented by a voltage injection or a current injection. Either approach requires certain conditions on the impedance on either side of the injected signal. Specifically, for the voltage injection approach, it is necessary that the impedance looking backward from the point of injection is smaller compared to that looking forward. While for the current injection, the reverse is required; that the backward impedance being much greater than the forward. Fig. 5.8 gives a schematic of the procedure for both the current and voltage injection methods. In both cases, the loop gain, T may be given by the following formula (5.13);

$$T = \frac{v_y}{v_x} \tag{5.13}$$

For a given frequency, the magnitude is computed from the magnitude ratio of v_y and v_x. Resolving the trigonometric solution of the phasor also yields equation (5.14) for the computation of the phase angle [6].

$$\angle T = \pm \arccos \left[\frac{|v_z|^2 - \left(|v_x|^2 + |v_y|^2\right)}{2|v_x||v_y|} \right] \tag{5.14}$$

Gain and phase margin compensation for loop stability

For feedback circuits, oscillation at high frequency is a challenge. From previous block diagram and the equation (5.8), the ratio of V_{in} to V_{out} resolves to infinity in the event that the product GH is -1. This may occur in the event of a phase shift of -180 degrees and unity gain, effectively making the circuit a positive feedback. It is necessary that there is adequate margin of operation to avoid an oscillation.

To prevent this, it is required that the gain falls well below the 0db crossover before a phase shift of up to 180° . This helps to make room for some phase margin. As noted earlier, the feedback loop including the op-amp exhibits a low pass characteristic. The Bode plot in Fig. 5.9 shows the obtained frequency response of the control circuit. For practical applications, a gain margin of 3dB, together with a phase margin of about 60° is recommended [65]. Fig. 5.9 shows the response for both the uncompensated and compensated frequency response derived using the method described in the previous section. From the plot, it is shown that the phase margin sits at about 80° which is large enough. The gain margin however appears to be relatively low in the uncompensated response. To achieve the required margin, a dominant pole compensation [63] strategy is adopted. This compensation allows a faster roll-off of the first natural pole such that phase shift due to the second pole only starts with the gain already below 0db. The dominant pole however sacrifices some open loop gain as well as bandwidth for stability. The compensation network has been chosen to optimize for the required bandwidth for the impedance measurement while fulfilling the stability requirement needed to prevent oscillation. With the compensation, the frequency response

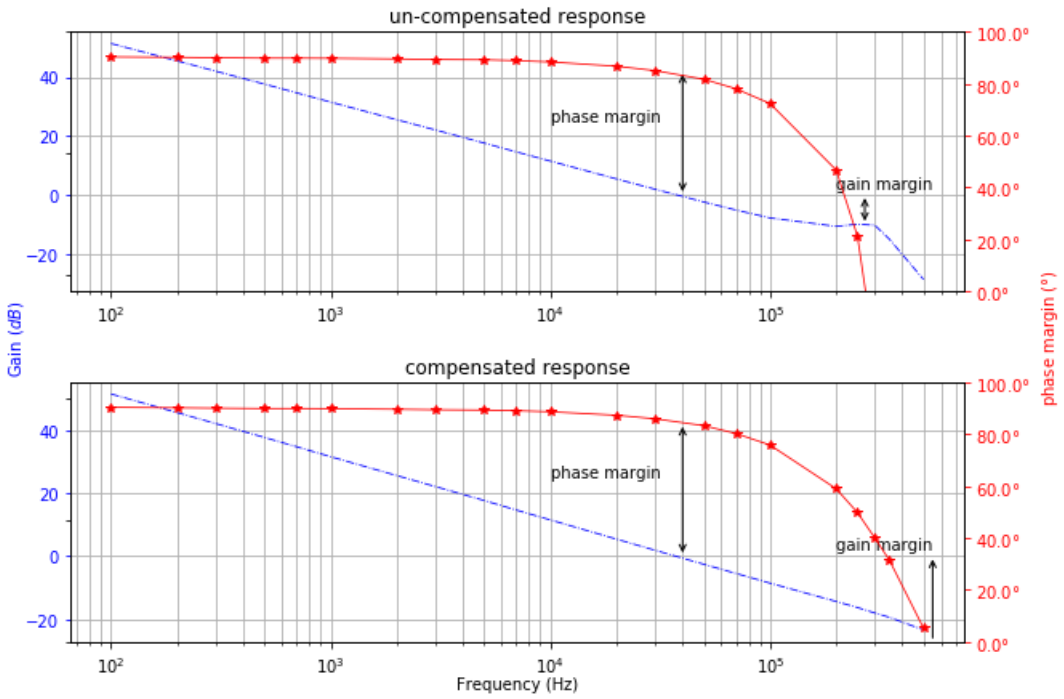

Fig. 5.9: Measured AC response of the control loop showing the effect of the compensation as it affects the gain and phase margins.

now exhibits an increased gain margin of about 28dB, with the phase margin maintained to ensure the desired stability.

5.4 Implementation and Measurement

The measurement involves acquisition of the voltage and current signals as shown in Fig. 5.2. The input perturbation signal is prepared in MATLAB and realized via the National Instruments Data Acquisition (DAQ) equipment which provides the control output to the active load input. The data acquisition only provided for a global sampling frequency across all input and output ports. As such, the same sampling frequency is used for both the signal generation and acquisition. For each perturbation frequency, a sampling frequency $Fs \geq 2f$ is ensured in accordance to the Nyquist theorem. A 2MS/s National Instruments data acquisition (DAQ) device is used in this work. At this rate, the maximum frequency of interest which is 10kHz affords a maximum of 200 samples/period. 500 samples are used per period of signals not

greater 4kHz. In order to generate the higher signal frequencies, the sampling frequency, F_s, of the device had to be changed dynamically within the software as given in (5.15).

$$F_s = frequency \times samples \leq 2Ms/s \tag{5.15}$$

The perturbation signal is summed up with a desired DC offset serving as the operating point. To avoid clipping of the negative cycles of the sinusoidal signal, adequate offset is ensured for each measurement.

The processing stage extracts the information only corresponding to the frequency in question. To achieve this, the signal is transformed to the frequency domain using Discrete Fourier Transform (DFT), where information on the magnitude for each frequency is distinguishable. The required frequency information is then extracted from the voltage and current data.

5.4.1 Filtering

The signal integrity must be considered to adhere accurate impedance information. The acquired signals may contain other frequencies outside of the perturbation frequency. To prevent aliasing, signals are passed through a filtering stage prior to the data acquisition. Anti-aliasing filters are used to remove frequency components greater than half of the sampling frequency to reduce the effect of high frequency distortion. A unity-gain Sallen-key topology shown in Fig. 5.10 is implemented.

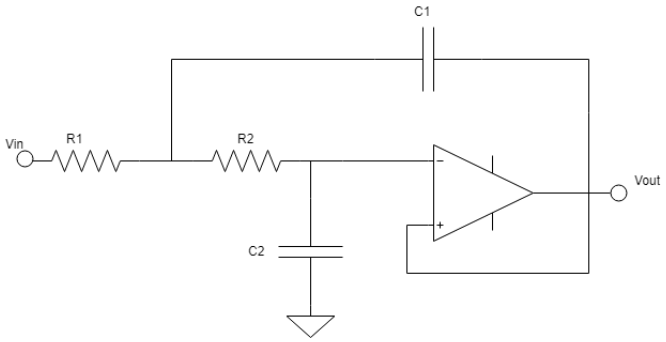

Fig. 5.10: Sallen-Key low pass filter configuration.

This has been chosen for its simplicity and acceptable performance. The transfer function of this topology is given in equation (5.16)

$$\frac{v_0}{v_i} = \frac{1}{S^2 R_1 R_2 C_1 C_2 + C_2 (R_1 + R_2) + 1} \tag{5.16}$$

The filter needs to be designed for a cut-off of, at most half the sampling frequency. Component values are obtained using the following equations [66].

$$\text{let } \frac{R_1}{R_2} = m \text{ and } \frac{C_2}{C_1} = n \tag{5.17}$$

$$Q = \frac{\sqrt{mn}}{m+1}, \quad f_c = \frac{1}{2\pi RC\sqrt{mn}} \tag{5.18}$$

$$R_2 C_1 = \frac{1}{2\pi f_c \sqrt{2}} \tag{5.19}$$

m and n are chosen to be 1 an d 2 respectively. With a sampling frequency of 100MS/s used for acquisition, a cut-off frequency, f_c of 50kHz is chosen where Q is the Q factor. A standard value of 10nF is chosen for C_1 which corresponds to a R_2 value of about 225Ω and a standard 220Ω resistor is chosen for simplicity. R_1 and C_2 are then calculated using the relationship above.

Figures 5.11 and 5.12 show the filtered and unfiltered samples in the time and frequency domain respectively for a sample 100Hz signal acquired.

The time domain representation shows an obvious improvement in the variance of the signals. Also, it is seen that higher frequency components have been significantly attenuated.

5.4.2 Quantisation

The data acquisition is done via sample and hold to realize the discretized signal [67]. This consists of the sampling and the quantisation processes. The error associated with the quantisation process may be analysed for the fundamental frequency perturbation. The signal

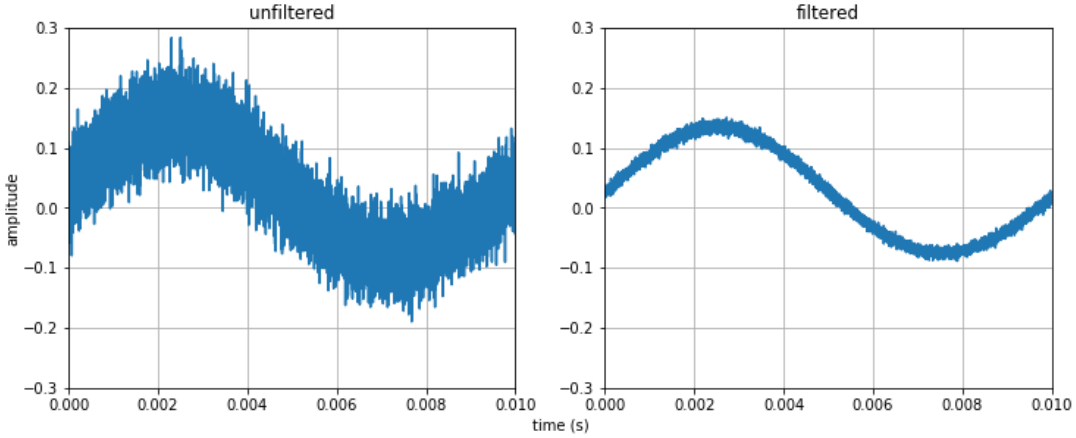

Fig. 5.11: Time domain representation of the filtered and unfiltered acquired signal showing the filtering effect.

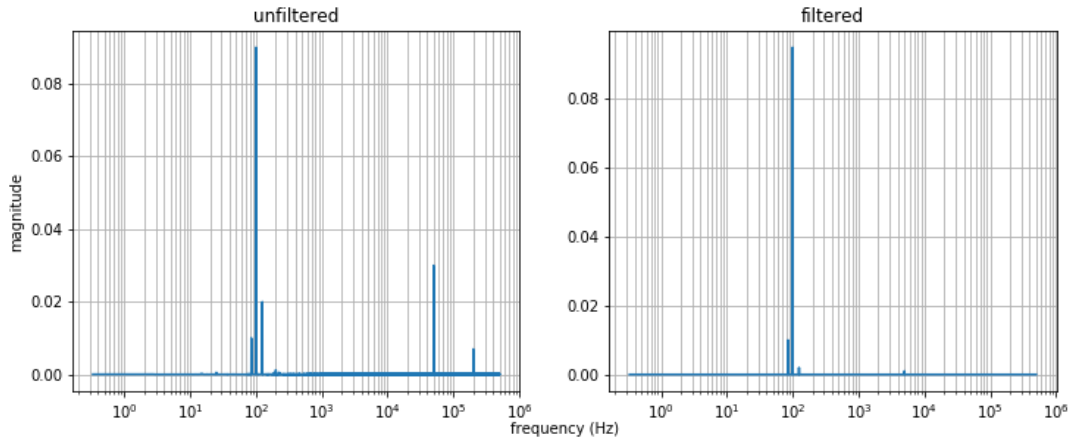

Fig. 5.12: Frequency domain representation of the filtered and unfiltered acquired signal showing the filtering effect.

$y(t)$ is related to its quantised version as follows,

$$y_q(t) = kq \tag{5.20}$$

where, $kq - \frac{q}{2} \leq y(t) < kq + \frac{q}{2}$.
The amplitude a_m may then be written in terms of the number of quantisation level, l between 0 and a_m as in (5.21).

$$lq - \frac{q}{2} \leq a_m < lq + \frac{q}{2} \tag{5.21}$$

With l qunatisation levels, the magnitude error may be computed using the following equation derived in [68]. Using this, the minimum level required to achieve an error limit may be computed. Typical EIS measurements often requires that the signals consists of a DC set point as well as the perturbation signal. However, in most cases, the amplitude of the perturbation signal is relatively smaller than the DC point. Due to the low impedance of the fuel cell system, this response to the perturbation is also relatively low compared to the DC component. The implication of this is that there is low resolution of the perturbation components because the quantisation level are mostly used up by the relatively large DC component. To address this problem, a high pass filter may be used to remove the DC components. However, with low frequencies required for EIS measurement and the use of a high pass filter may distort low frequency signals. Further, design of such high pass filter will require significantly complicated circuitry. Instead this impact is minimized by setting the input range of the DAQ device close to that of the signals to be acquired for each measurement which results in acceptable performance. For least significant bit for an n bit DAC is given as (5.22).

$$\frac{v^+ - v^-}{2^n} \tag{5.22}$$

Where $(v-, v+)$ is the input range set. For a ceiling magnitude error requiring l quantisation level, the following is required (5.23).

$$input\ signal peak \geq l \times \frac{v^+ - v^-}{2^n} \tag{5.23}$$

For a magnitude error of 0.1%, l needs to be greater than 50 following equation (5.24) [68].

$$y_e = 100 \left[1 - \frac{4}{\pi(l-0.5)} \sum_{k=1}^{l-1} k \left(\sqrt{1 - (\frac{k-0.5}{l-0.5}^2)} - \sqrt{1 - (\frac{k+0.5}{l-0.5}^2)} \right) \right] \tag{5.24}$$

This lower bound is reconciled with the minimum amplitude of the observed signals to set the gains such that the minimum requirement is met.

5.4.3 Current and Voltage Measurement

The current data was collected with the aid of a LEM LA55 hall effect sensor which is powered by a $\pm$15V supply. Its conversion ratio of input to output is 1000:1. In order to achieve a 1:1 measurement, the output voltage is collected across a 1kΩ resistor. Since the current signal is within the range (-10V, 10V) of the DAQ device, the signal is acquired directly with no need for a down-scaling. The voltage of interest is the output voltage of the device under test and this is also acquired after filtering.

5.5 Experimental Tests and Results

The overall set-up is shown in Fig. 5.13 with the data acquisition device and the load control circuitry. The DAQ device is also responsible for the input control signal in addition to the voltage and current sensing. The load control unit has been mounted on a heat-sink for heat dissipation.

Tests were conducted on the load using a workbench power supply unit for calibration purposes with the set-up as shown in Fig. 5.14. The input signal is synthesized in the

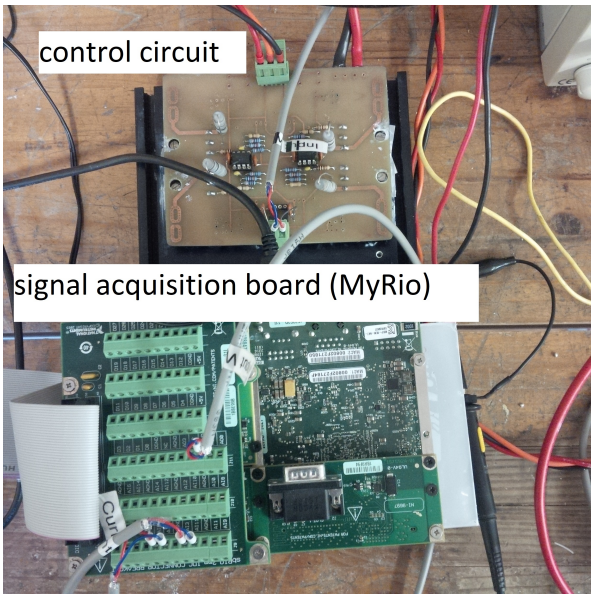

Fig. 5.13: The active load setup showing the RIO acquisition device together with the control circuitry on a heatsink.

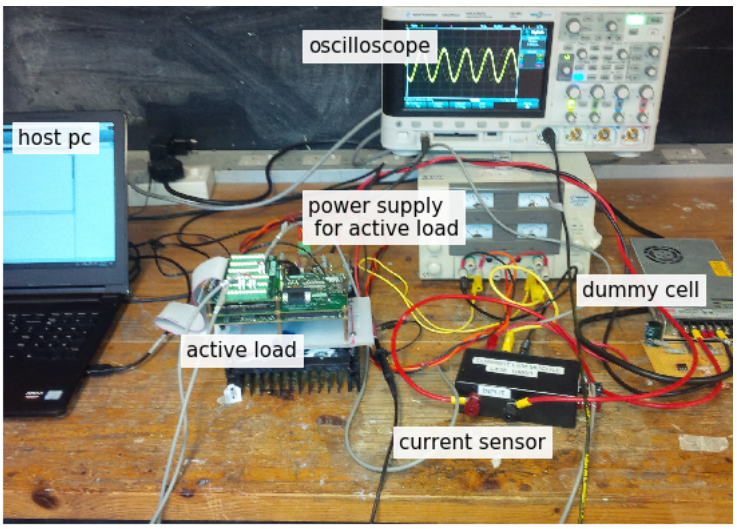

Fig. 5.14: The setup used for calibration of with discrete circuit elements.

MATLAB environment on the host and realized by the DAQ device which then controls the active load. The oscilloscope is used to monitor the various signals. The bench supply acts as the device under test and is first used to accurately determine the DC characteristics of the active load set-up. The plot of control voltage against the drain current is shown in Fig. 5.15.

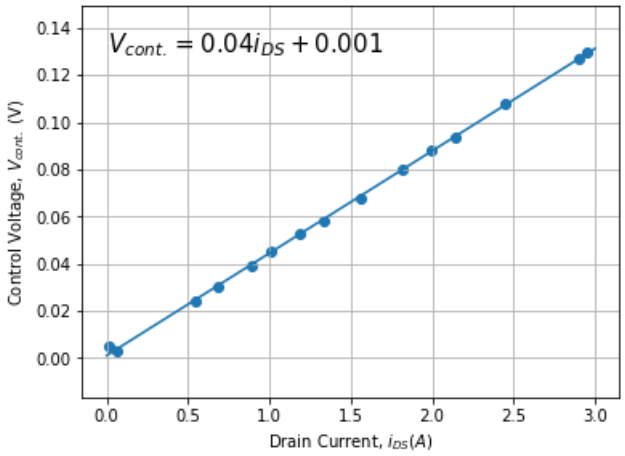

Fig. 5.15: Active load linear control characteristics showing the relationship between the control voltage and the drain current.

The sense resistor determines the linear relationship between the DC control voltage and corresponding DC current. To determine its value precisely, data was collected for varying control voltage set-points and the corresponding current measured. A linear regression fit is performed to extract the precise resistance value which is the gradient as shown in the Fig. 5.15. and this is used to compute the control voltage.

5.5.1 Impedance Measurement

In this section, the use of the active load in carrying out impedance measurement is described. Results obtained are compared with a commercial frequency response analyser.

As the equipment is intended for use with fuel cell system, a simple Randles equivalent circuit is built with discrete electrical components to compare its performance with a commercial FRA equipment. The Randles equivalent circuit is connected in series to the supply of a

Table 5.1: Component values for Randles equivalent circuit model

Component	value
R_{ohm}	0.5Ω
R_{ct}	4.7Ω
C_{dl}	$2.2\mu F$

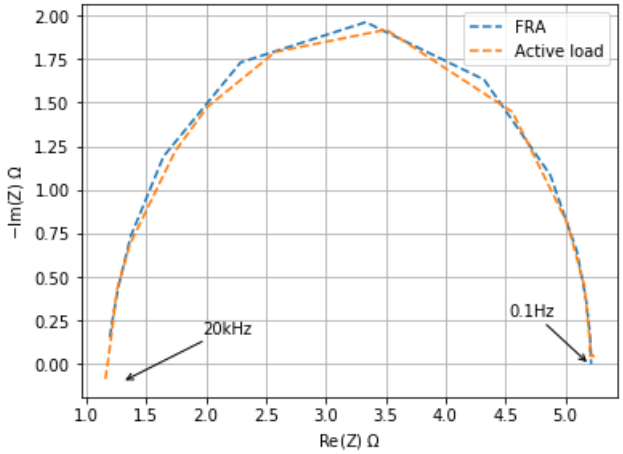

Fig. 5.16: Experimental result showing the Nyquist plot generated using the active load in comparison with commercial FRA equipment for discrete element equivalent circuit.

predetermined output impedance so the impedance of the circuit alone could be determined. The values for the model components are given in table 5.1. These values have been chosen arbitrarily given readily available components just to verify the performance of the system. The resulting Nyquist plot is shown for the standard FRA equipment and active load as in Fig. 5.16. It is seen that the result from the active load matches that of the FRA closely enough across the frequency band for impedance estimation.

The experimental test setup for the fuel cell is as shown in Fig. 5.17. Here the developed active load device is connected as usual to the device under test which in this case is the fuel cell. The fuel cell normal operating conditions are set using the Fuelcon SCADA interface and EIS procedure is started after conditioning.

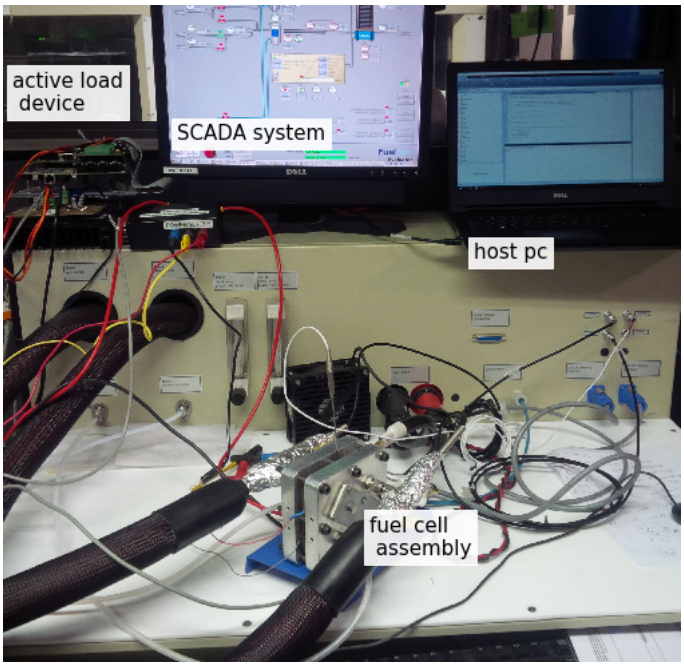

Fig. 5.17: The setup for fuel cell testing.

5.5.2 Results and Discussion

Since the impedance measurement is based on steady state assumptions, care must be taken to consider this in practice. However, it is difficult to ensure steady conditions in real-life measurements especially for an electrochemical system like the fuel cell [3]. A work around is to ensure a good number of cycles is collected for processing procedures such as the FFT computation [69]. This helps to improve the results by reducing the effect of distortions due to transient conditions.

This idea is demonstrated below with the experiment run for a number of periods. The improvement in the spectral information is obvious with increased periods as seen in Fig. 5.18. Fig. 5.18 shows the magnitude frequency spectrum for 2, 4 and 6 periods of the computed signal in order. The red line indicates the gradual decrease in the second highest high frequency distortion with a corresponding increase in the number of periods. It is important to note this for more sophisticated impedance measurement techniques such as a broadband signal (later discussed). The trade-off must be made between the desired accuracy and number of pe-

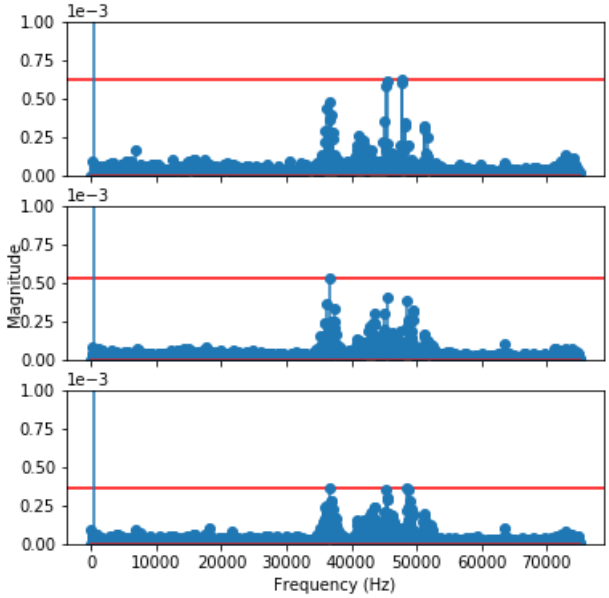

Fig. 5.18: Effect of increased integration times on the distortion in the frequency spectrum. The plot is shown for 2, 4 and 6 periods in order from the top.

riods to ensure a quick measurement. For impedance results shown, 3 periods have been used.

It is also necessary to ensure that the amplitude of the sinusoidal signal is small enough to make for approximately linear excursions of the sinusoidal perturbation.

To understand the effect of the sinusoidal amplitudes, the experiment was run for different amplitudes with the harmonics examined. Linear systems theory establishes that the response to a sinusoidal perturbation of a linear system is also a signal of same frequency with a possible phase shift and amplitude scaling given causality and stability of the system [43]. The harmonic distortions on the current signal is computed for increasing amplitudes using the Total Harmonic Distortion (THD) measure as in (5.25).

$$THD = \frac{\sqrt{V_1^2 + V_2^2 + V_3^2 + \dots}}{V_F} \times 100 \tag{5.25}$$

where $V_1 + V_2 + V_3 + \dots$ represent the harmonics and V_F represents the fundamental frequency. The 2nd, 3rd and 4th harmonics are used to approximate the distortion present due to the possible non-linearities. Fig. 5.19 shows the plot of the THD values for a chosen frequency

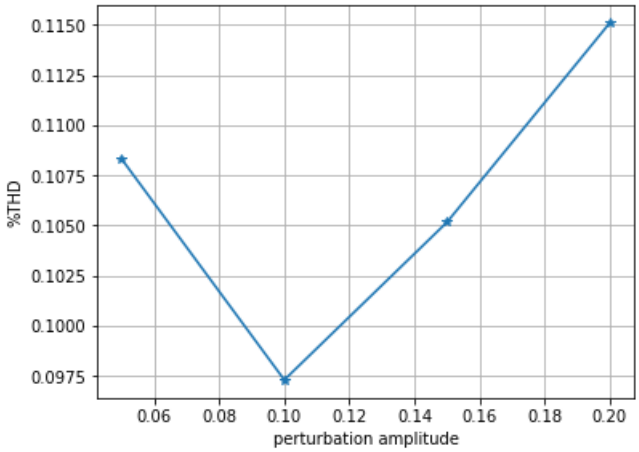

Fig. 5.19: Graph showing the percentage total harmonic distortion for corresponding perturbation amplitude. A minimum is seen to occur at perturbation amplitude of 0.1

for increasing amplitudes. It can be observed that the magnitude of the harmonic distortion does not exhibit a monotonic behaviour with increasing amplitude. Particularly, a minimum distortion appears at a perturbation amplitude of 0.1. For accurate impedance measurement, it is important that there is a compromise between minimizing the harmonic distortion due to increasing amplitude and improving the signal to noise ratio [48]. The resulting Nyquist plot of the impedance for both the active load and commercial FRA equipment are as shown in Fig. 5.20. The equipment could also be employed for a wide range of signals such as the chirp as shown in Fig. 5.21. This flexibility makes it useful for various diagnostic procedures by signal injection.

5.6 Conclusion

The load modulation technique for the realization of EIS has been presented. This has been implemented with a low cost active load which may be controlled by input voltage signals. The procedures to ensure a valid impedance spectrum are also discussed and results are presented to demonstrate the capabilities of the active load for frequencies of up to 20kHz for impedance estimation. The results demonstrate the ability of the active load to replace expensive FRA equipment as a portable and low-cost alternative. The equipment also offers

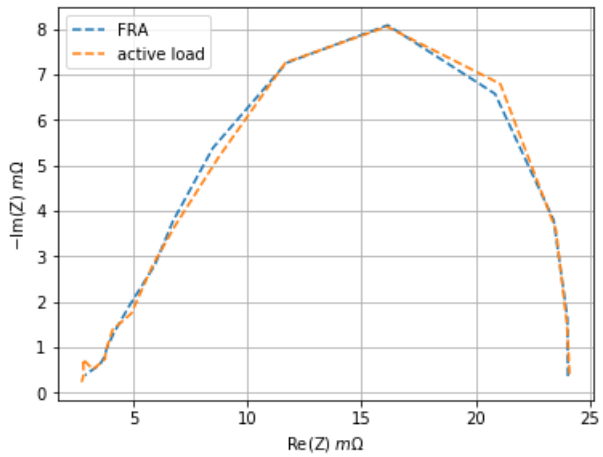

Fig. 5.20: Nyquist plot for fuel cell for both the active load device and the standard FRA equipment.

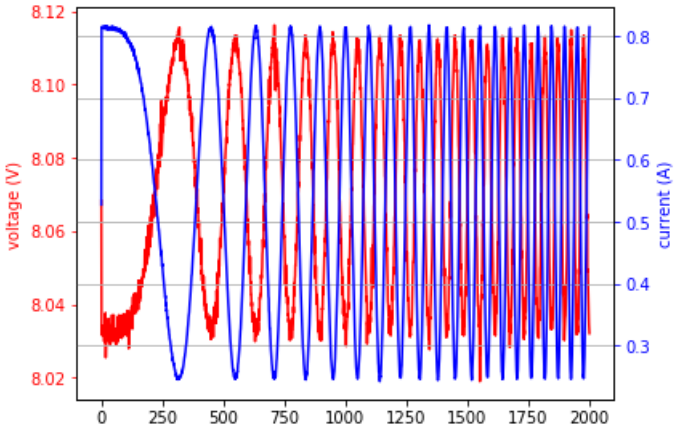

Fig. 5.21: Chirp signal perturbation and response by active load showing the suitability of the device for superimposing an arbitrary signal.

flexibility in the different types of signals that could be injected. Its capability to inject an arbitrary signal will also be leveraged in investigating alternative signal types for rapid EIS measurement later in this work.

Chapter 6

Multi-Sine Signal Optimisation

6.1 Introduction

A key advantage of the EIS over other electrochemical methods is its ability to provide more diagnostic information. Small amplitude transient signals may be injected around an operational point with the response recorded and impedance may be computed. This procedure is commonly carried out with the use of expensive commercial FRA in the laboratories. A low-cost alternative to this has been developed as detailed in the previous chapter and this makes use of an active load which receives a perturbation signal input summed with a desired DC point.

Perturbation signal choice is critical to the analysis of the dynamic behaviour of the fuel cell. Conventional single sinusoid EIS takes a significant amount of time largely due to low frequency signals. For the set of desired frequency perturbation, each frequency point is injected one after another. In order to ensure reliable measurement, a rest time is also required between intermediate frequencies, further resulting in an time-consuming process This makes the procedure unsuitable for real-time state of health information acquisition.

The multi-sine signal has been proposed to address the time efficiency of the EIS [70] for on-line analysis. The time reduction is achieved by taking a linear combination of required

discrete frequency points as one composite signal. This enables the simultaneous measurement of spectral components. The signal period is then determined by the lowest frequency component in the set. The impedance is calculated by dividing the complex output frequency coefficient by the corresponding input coefficients. This method however, may introduce some challenges in its accuracy. Although inherently nonlinear, the linear assumptions for fuel cell EIS helps to simplify analysis. This also requires that the amplitude of the perturbation signal is kept minimal as discussed in [48]. Linearity can however, not be fully achieved, and this results in harmonics of the fundamental frequency being generated in the output response [71]. For the multi-sine EIS approach, the implication is that these harmonics may interfere with the other signal input of higher frequency, resulting inaccurate measurement.

In addition, the linear combination of individual frequencies leads to an increase in the amplitude of the composite signal. An increased amplitude results in violation of the linearity assumption required for the impedance computation using the Ohm's law [71]. In this work, the crest factor and the frequency distribution are considered for the optimisation of the multi-sine signal towards an accurate measurement. A low crest factor is required to addresses the need to minimize the multi-sine amplitude to achieve quasi-linearity. Some work have been done to address this amplitude challenge. A time domain optimisation technique to minimize the amplitude of the multi-sine signal has also been used [51]. Phase values that minimize the amplitude are found for each individual frequency component. However, the compromise between the amplitude and the corresponding signal to noise ratio needs to be considered. Ultimately, to make diagnostic inference from multi-sine EIS data, the measurement errors must be minimized.

The frequency distribution proposed in this work here is in two stages. First a frequency distribution is detailed and the optimisation of the resulting perturbation signal is presented. To achieve an impedance spectrum for the fuel cell within a frequency band of interest, it is often enough to take a set of discrete points within the desired interval. Interpolation techniques may then be utilized to obtain an approximate spectrum. The goal here is to

ensure the frequency set chosen within the interval of interest closely approximates the ideal spectrum. Two characteristics of the component frequencies to be considered in this light are the distribution as well as the number of frequency points. A trivial choice of frequency is an equally spaced set of frequency points within the interval of choice. Considering the frequency band of interest of the fuel cell EIS, this would require many of frequency points. Taking the linear combination of such many sinusoidal signals would result in a high crest factor signal which is undesirable for linearity considerations of the impedance measurement. The authors in [51] noted the importance of the resolution of the impedance and it was also suggested in [72] that prior knowledge of the impedance spectrum relaxation may be useful in making this choice. To ensure adequate impedance resolution within the frequency range of interest, the frequency points need to be carefully chosen [42]. Following this, a linear-log-linear frequency distribution was proposed for frequency components of the multi-sine perturbation signal, where the distribution is linear for the low and high frequency regions [51]. Owing to the significant variation in the impedance response in the mid-frequency region, an exponential distribution is adopted. This choice was made to reduce the effect of non-linearities which may introduce higher order harmonics at fundamental frequency points. For this work however, the choice of the proposed distribution curtails the need to have this sparse distribution which may lead to low resolution for impedance information.

The frequency selection is investigated here with the goal of achieving a signal which is robust to the effect of harmonics or noise. This proposed approach is designed and implemented with the aid of the low-cost active load device developed in the previous chapter. The performance of the new approach is evaluated on a simulated non-linear system and compared, based on an accuracy metric, with the exponential frequency distribution. The method is then tested on a fuel cell to investigate flooding and drying phenomena on the PEMFC, with results showing good correspondence with measurements using the single sine technique on the commercial FRA.

6.2 Signal Synthesis for Optimal Impedance Spectroscopy Measurement

In addition to causality and stability, linearity is a major condition for valid impedance spectroscopy measurement [44]. For conventional impedance spectroscopy measurement performed on the fuel cell, this condition is difficult to achieve. This poses even more of a challenge for a multi-sine perturbation schemes.

The periodic multi-sine perturbation signal of N discrete frequency components may be represented in time domain as follows (6.1);

$$X(t) = \sum_{i=1}^{N} a_i \cos(2\pi f_i t + \Phi_i) \tag{6.1}$$

where a_i is the amplitude of i_{th} sinusoidal component, f_i is the frequency of i_{th} sinusoidal component and Φ_i is the phase of the corresponding component. Each frequency component is uniquely defined by its amplitude, phase and frequency values.

The response of the fuel cell due to its non-linear characteristics consists of higher order terms in addition to the excited frequencies of the perturbation signal. These higher order terms manifest as harmonics of the fundamental frequency. In a multi-sine input signal, harmonics generated by lower frequency component could interfere with other components of the multi-sine signal. These harmonics compromise the accuracy of the overall impedance estimation over the simplifying assumption of linearity and causality. In addition, the non-linearity of the fuel cell tends to increase under certain conditions such as flooding [42] making it non-deterministic.

To mitigate against the effect of harmonics, a frequency set which reduces the chance of harmonic interference from lower frequency components is desired. Precisely, a set of frequencies, S is required, such that for every element i of S, $n \cdot i$ is not an element of the

same set S. n here may be any positive integer greater than 2 up to a maximum of about 5. This condition minimizes the effect of having harmonics of lower frequencies impact higher order components as will be shown.

A set fulfilling the requirement is a set of pairwise coprimes and the set of prime frequencies is an even more special case [73]. It is important to be sure of the feasibility of this requirement for a given upper bound. Results in number theory established that the maximal number of integers $a_1 < \ldots a_k \leq n$ with none dividing the other is $n - \frac{n}{2}$ [74]. This gives room for enough frequencies within the typical EIS range for most applications. For fuel cell EIS measurement, the band of interest lies between 0.1 Hz and 10 kHz [1]. In order to fulfill the pairwise coprimality condition for frequencies $f < 1$, these frequencies f_l may be chosen such that 1 modulo $f \neq 0$. The corresponding 10th multiple $(10 * f_l)$ may then be omitted from the set to maintain the condition although this may not be necessary given that 10 is relatively large with negligible effects.

The result of the above scheme is a signal that is relatively less prone to harmonic distortion effects as would be shown in the following sections. While there are other sets S which fulfill the pairwise coprimality condition, a prime number set is employed as a special case for $f > 1$ and will ensure some robustness towards harmonics due to unintended input signal. Another consideration in this work is the application in which the required impedance information is targeted. The low frequency regions of the fuel cell impedance capture significant information useful for diagnostics. Phenomena such as flooding and drying mostly result in effect which manifest in the lower frequency as far as impedance is concerned [60]. Essentially, a function which begins with a slow growth and ramps up is preferable to increase required resolution in the low frequency regions. For this, an exponential function in base two is chosen and may be expressed as follows (6.2);

$$f_j = 2^j f_0 \tag{6.2}$$

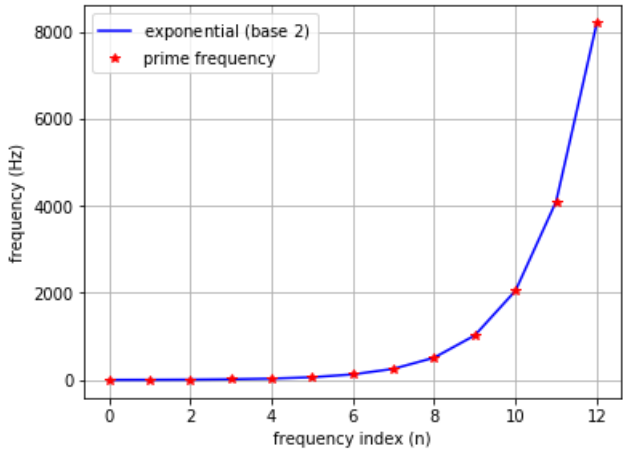

Fig. 6.1: The exponential frequency distribution showing the prime frequency points.

where f_0 is a start frequency point and $j \in \mathbb{Z}$. The result of this is shown in Fig. 6.1 with the blue line. The selected set of coprimes is now required to follow this distribution closely. In order to achieve this, the closest prime number to the frequency point is selected where closeness is defined as the absolute difference. The co-prime frequency sequence (CFS) is expressed as follows;

Let $|f_j - P|$ denote $(|f_j - p_1|, |f_j - p_2|, \ldots, |f_j - p_m|)$. Then,

$$frequencypoint, f_n = p_i \tag{6.3}$$

Where;

$i = arg\min(|f_j - P|)$

$P = (p_1, \ldots, p_m)$ is the set of prime in the desired interval

$F = (f_1, \ldots, f_k)$ is the set of exponential frequency point in the desired interval.

The composite signals making up the multi-sine result in an overall increase in amplitude and peak factor as previously discussed. Injecting this multi-sine signal in a fuel cell system will result in perturbation excursions farther away from the desired operating point, resulting in an unstable system affecting the accuracy of the system.Ideally, the peak value of the multi-sine signal should be much lower than its RMS [75]. The Crest Factor (CF) metric

which relates the signal peak and its rms value is often used to measure how extreme the peaks in the signal are relative to the overall signal [72]. The CF of a periodic time domain signal $x(t)$ with period T is defined mathematically as follows (6.4). follows (6.4).

$$CF = \frac{max_{t\in[0,T]}|x(t)|}{x_{rms}} \tag{6.4}$$

where,

$$x_{rms} = \sqrt{\frac{1}{T}\int_0^T [x(t)]^2}$$

For a given number for frequency components, the CF is dependent on the choice of phase for each of the signal. The challenge therefore is to design a waveform with a set of individual phase values that minimize the CF of the multi-sine. This may be expressed as follows;

$$arg\min_{P\in\mathbb{R}^n} f(P) \text{ subject to } 0 \leq p_i \leq \pi \tag{6.5}$$

The minimisation of the CF poses a non-linear optimisation challenge [72]. Various methods have been proposed for the minimization of the CF as a function of the phases of each frequency component. Two prominent approaches include the Schroder [76] and Newman Phases [77]. This problem as addressed by Schroeder used the asymptotic relationships between the power spectra of frequency modulated signals and their instantaneous frequencies [76]. For a spectrum with N consecutive harmonics, Schroeder showed that the phase of the nth harmonic may be given as (6.6). The relationship proposed by Newman is also given as (6.7)

$$\text{Schroeder phases: } \theta_n = \theta_1 - \frac{\pi n^2}{N} \text{ for } n = 1,\ldots,N \tag{6.6}$$

$$\text{Newman phases: } \theta_n = \frac{\pi(n-1)^2}{N} \text{ for } n = 1,\ldots,N \tag{6.7}$$

Table 6.1: Crest factor and peak results for different optimisation schemes.

scheme	crest factor	peak amp.
zero	3.667	0.9896
Newman	3.9667	1.0553
Schroeder	4.0310	1.1097
GA optim.	3.3315	0.9119

More recent approaches have employed numerical optimisation routines to achieve an optimal phase arrangement [78].

The genetic algorithm (GA) optimisation approach is explored in comparison to the other two methods to solve the optimization problem as posed. The GA serves as a method for solving optimisation problems whose objective functions are non-linear [65]. The algorithm begins towards an optimal solution with the creation of an initial population of possible solutions. The population is updated with a new population determined by scoring each member of the previous population using a fitness value after each iterative step. This procedure is repeated until some stopping criterion is met.

The GA for the crest factor minimization is implemented using the MATLAB optimisation toolbox. The objective function to be minimized is as given in equation (6.5). Although the GA is not guaranteed to produce a global solution, several parameters such as initial conditions may be tuned to achieve a viable solution. The CF as a function of phases has several local minima [77]. To have a sufficient scan of the solution space, the procedure was run many times with different initial points randomly generated. For each run of the algorithm, the function tolerance was used as the stopping criterion. This effectively monitors for an improved solution over a given window of generations. The procedure terminates if the average change in the fitness value is less than the function tolerance. The overall minimum which minimizes the N-dimensional objective function is then chosen as the set of phases that gives a minimum crest factor.

Table 6.2: Frequency and optimised phase values

freq.	phase
0.3	1.29
0.7	6.2332
2	6.1003
3	0.835970
7	6.189
17	5.0208
31	4.6259
61	0.035136
127	6.1102
257	0.23
509	1.8158
1021	4.6075
2053	5.5032
4093	1.1707
8191	1.2762

Table 6.1 shows the results of the three methods by comparing the crest factors obtained and the peak of the resulting multi-sine signal. It can be seen that the GA approach performs better than the other two approaches. It is important to add here while the genetic algorithm approach yields the best results for this scenario, the performance may not necessarily generalize to other frequency distributions or values of N. Such distributions would have to be separately compared with other approaches to establish suitable optimisation routines to adopt. The genetic optimisation approach is also computationally expensive. This is however not a challenge in a case such as this application where the optimisation is only required once to determine the optimal phase arrangements. Also, it is observed the zero-phase scheme performs better than the Newman and Schroeder schemes, this is just a specific case given the number of frequency points. The phases generated are used to synthesize the now optimized multi-sine signal. The phases and the corresponding frequency are as given in table 6.2.

Figure 6.2 compares this optimized signal with the unoptimized equivalent. The unoptimized signal constitutes harmonic components with zero phases. With this array of phases, the

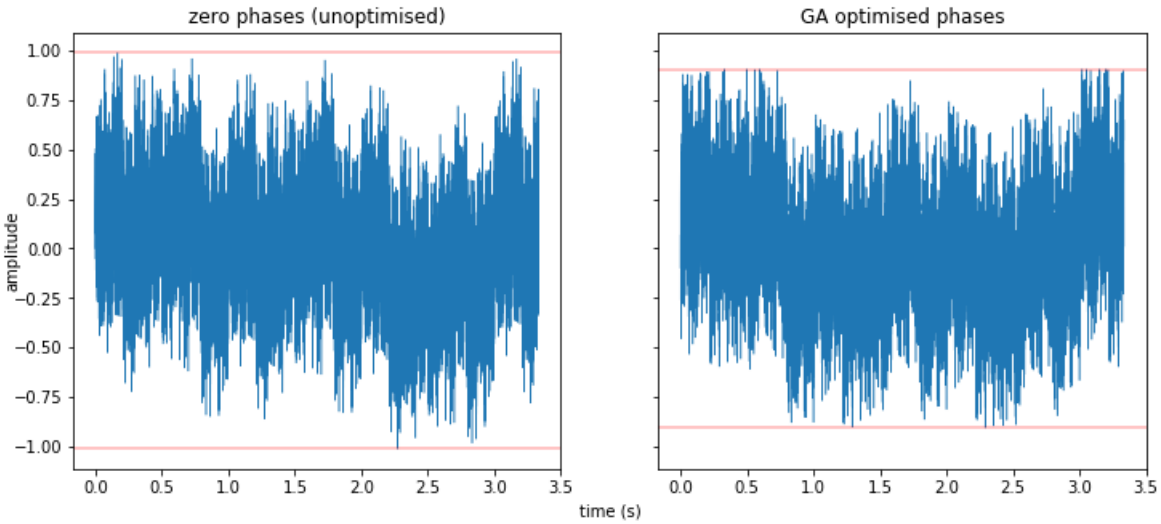

Fig. 6.2: Unoptimised (left) and crest factor optimised (right) multi-sine signals in time domain with lines showing the peak-to-peak amplitude.

crest factor is approximately 3.7. For the optimized signal using the phases in Table 6.2, a lower CF of 3.3 is obtained. In addition to the reduced CF, it is shown that the peak of the optimized signal is also reduced. The implication of this is that perturbing a system with the optimized signal will result in less distortion compared to the unoptimized signal ultimately ensuring more accurate measurements. Calculating the impedance is similar to that of the single frequency case. The response to the perturbation signal is acquired and the DFT of both the input and output components are computed using the FFT algorithm. The DFT complex coefficients may be extracted corresponding to the constituting signal for both the input and output signal. The impedance may then be computed as usual by taking the ratio of the output and the input signals for the corresponding frequency points.

6.3 Non-linearity Test

The weak non-linear characteristics of the fuel cell results in higher order harmonics which may lead to low accuracy of the impedance measurement. The prime frequency distribution has been presented to improve on the noise and harmonic rejection capability of the

Table 6.3: Coefficients for polynomial function simulating a weakly non-linear system.

coeff.	value
a_0	$25e-3$
a_1	1
a_2	$6e-1$
a_3	$-1e-3$
a_4	$5e-6$
a_5	$1e-5$

multi-sine scheme. To validate this, this section compares results achieved using the CFS distribution as proposed in comparison to the popular exponential frequency distribution. To achieve this validation, it is instructive that a simulation technique is adopted such that the causal relationship of the system for the input output is maintained. This also ensures that confounding variables such as those closely linked with time dependent behaviour are controlled for the purpose of comparison. An nth-order polynomial with $n > 1$ is used to simulate a nonlinear system. To imitate the weakly non-linear characteristics of the fuel cell, the higher order term coefficients are set relatively much lower compared to first order gain of the system. A fifth order polynomial function expressed as (6.8) is considered with coefficient values as given in Table 6.3.

$$f(x) = a_n x^n +, \ldots, +a_2 x^2 + a_1 x^1 + a_0 \tag{6.8}$$

Here x represents the input to the system f.

Another important factor is the noise and its effect on the accuracy of the measurement. The noise here may simply be modelled as an additive white Gaussian noise of zero mean coupled to the input of the system. This may be expressed as follows;

$$Noise, N = \mathcal{N}(\mu, \sigma) \tag{6.9}$$

The noise is summed up with the original signal as input to the system as shown in Fig. 6.3.

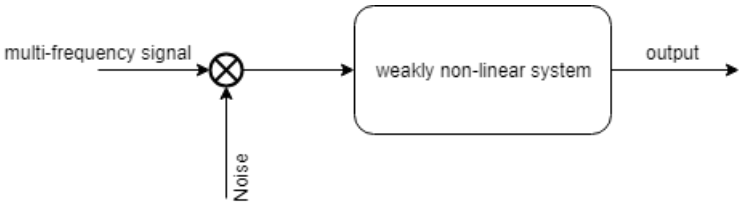

Fig. 6.3: Schematic showing noise-coupled input to a weakly non-linear system

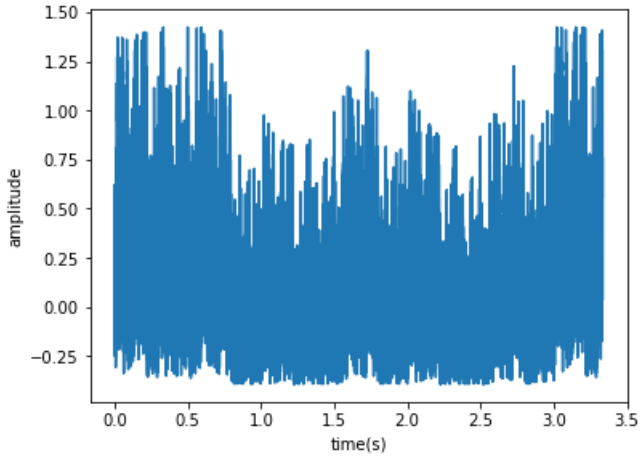

Fig. 6.4: Sample output in time domain of the weakly non-linear system for a noisy multi-sine input.

6.4 Results and Discussion

The system as designed in the previous section is implemented in MATLAB. The proposed approach is compared with the widely used exponential distribution [79]. Each multi-sine signal resulting for the different schemes serves as input x to the designed nonlinear system and the output computed from (6.8). Fig. 6.4 shows a sample output from the system which is now distorted and noisy. The frequency domain representations for the CFS and that of the exponential distribution are compared in in Fig. 6.5. Outside of the major frequency points, some harmonics may also be observed. These are due to the effect of the non-linear system on the input signal as well as the noise associated with the input signal.

For the considered outputs, a signal quality metric is needed for appropriate comparison. Herein, the effect of non-linearity in the input signals is quantified. The variable of interest

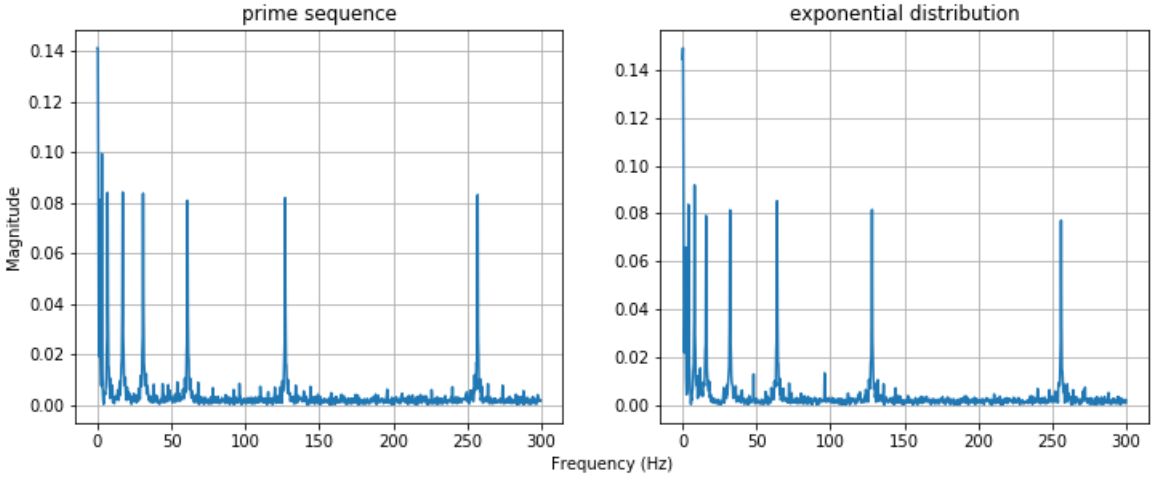

Fig. 6.5: Spectrum of the output corresponding to the proposed prime frequency (left) and that of the exponential distribution.

here is the magnitude of the input and output signal as the magnitude is key to the impedance results. The magnitude distortion metric between the input and output signals is thus defined as follows; Let X_i be the magnitude of frequency component, i, for input signal and $\hat{X}_i$ be the magnitude of frequency component i for the output signal. The input-output distortion, d may be defined as;

$$d = \sum_{i=1}^{N} |X_i - \hat{X}_i| \tag{6.10}$$

where N is the number of frequency components. The distortion is further calculated for increasing noise variance levels. Figure 6.6 compares the input output magnitude distortion, d as defined for both the exponential distribution and the proposed prime distribution.

The prime frequency distribution outperforms the exponential distribution with lower distortion across the noise level. This reduction in error implies that the proposed distribution is relatively less error-prone. Under anomalous conditions such as flooding, non-linear behaviour of the fuel cell becomes more significant leading to distortions in the magnitude spectrum. For diagnostic purposes, it is important to be able to carry out measurement under such conditions. The negative impact of resulting distortions under such conditions for a multi-sine scheme is however reduced with the proposed distribution. The CFS thus

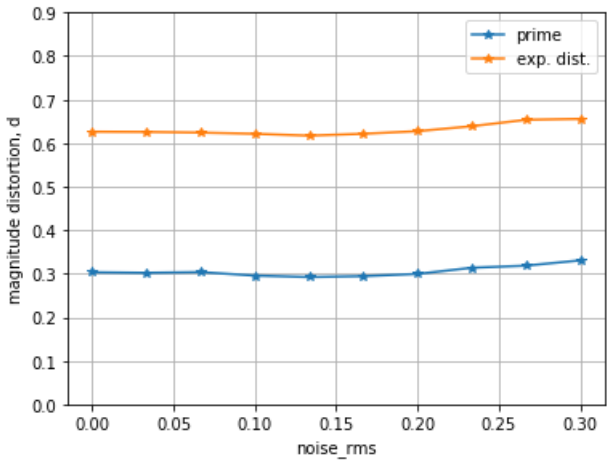

Fig. 6.6: The Magnitude distortion compared for both the prime frequency distribution and the exponential distribution.

improves the accuracy of the multi-sine EIS while affording the reduction in time relative to the single-sine EIS.

6.5 Fault Diagnostics

Water management is key to the performance of the fuel cell in operation. For the PEMFC in particular, this is a major challenge since water may exist as a liquid and gas given the typical operating temperature. Water is required to convey protons from the anode to the cathode efficiently. The persulfonated polytetrafluoroethylene simply known as Nafion is popular for use as electrolyte in the PEMFC due to its high ion conductivity [3]. Nafion however requires hydration to sustain this capability. For PEMFC, this hydration may be achieved by the humidification of incoming reactant gases. Water is also produced by virtue of the main electrochemical reaction in the fuel cell and may also be transported as a result of the electro-osmotic drag phenomena [1] which is aggravated by high currents. This occurs as a result of protons dragging water molecules while passing through the membrane from the anode to the cathode side. Accumulation of water at the cathode side may result in water flow from the cathode side to the anode side due to highly probable concentration gradient.

Removal of such products is necessary to prevent a blockage situation where reactants cannot reach reaction sites. These make water management an important issue for the fuel cell and it is important that measures are taken to ensure that such unwanted conditions are detected in time to prevent further damage to the system while in operation.

An important point to note is that, even though the inlet gases may be controlled to the required amounts, the performance of the cell is ultimately determined by the availability of reactants at the reaction sites in appropriate amounts, which may be subjected to other factors other than the inlet flow rates. While the fuel cell is in operation, probing this is difficult. We must therefore rely on surrogate fault characteristics or signatures.

The EIS earlier discussed offers a profound way to characterise the electrochemical processes of the fuel cell system as had earlier been discussed. Furthermore, techniques developed in this work in previous sections have proved to improve the capability of the EIS measurement in terms of measurement accuracy as well as reducing time cost. These techniques are hereafter deployed for diagnostic purposes of the fuel cell in the presence of simulated fault conditions - flooding and drying, which are two prominent faults related to water management of the fuel cell.

6.5.1 Experimental Setup

The setup used is similar to that shown in Fig. 5.17 with the schematic in Fig. 5.2 illustrating the setup. Initial conditioning was performed and the fuel cell conditions are maintained at normal parameter values as already discussed. A constant current of 10A is also maintained. In this predetermined standard operation, initial measurement were carried out to establish normal operation. Flooding and drying procedures are then initiated using the procedures describe in chapter 4.

Separate MEAs have been used for simulation of the different fault conditions in this work. This is necessitated by the fact that flooding and drying effects tend to affect the MEA which

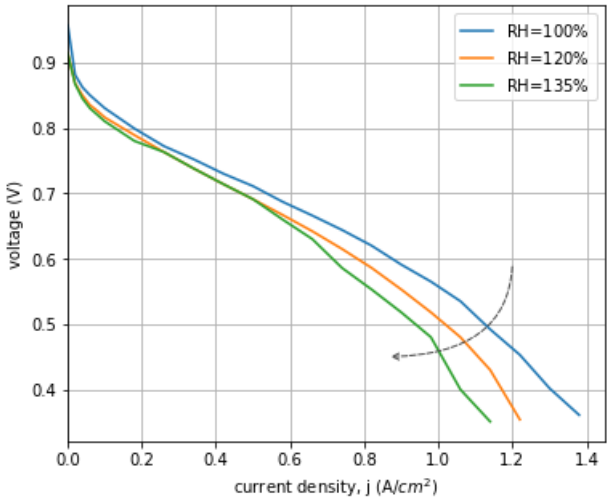

Fig. 6.7: Polarisation curve showing the current voltage relationship for different levels of flooding.

may translate to confounding results for the different faults when the same MEA is used. Polarisation curves are first used as a baseline comparison to ascertain the performance of the different MEAs are equal under standard conditions. Measurements were taken at different values of current densities which is expected to translate to varying degrees of flooding and drying since higher currents aggravate flooding and lower currents help induce drying while the necessary humidity gradient is ensured in each case.

The multi-sine signal was synthesized as described in the previous section in the MATLAB environment and realized via the output port of the National Instruments signal acquisition device. For the flooding condition, the perturbation signal was injected under the flooding condition and the response acquired at 100000 samples per second, which is about 10 times the highest frequency of the constituent frequencies of the multi-sine signal. Acquisition time was about 3.33 seconds, largely dictated by the lowest frequency signal - 0.3Hz.

6.5.2 Results and Discussion

The polarisation curves are shown for different flooding levels dictated by the change in relative humidity in Fig. 6.7. There is clearly a change in the $i - v$ characteristics from the

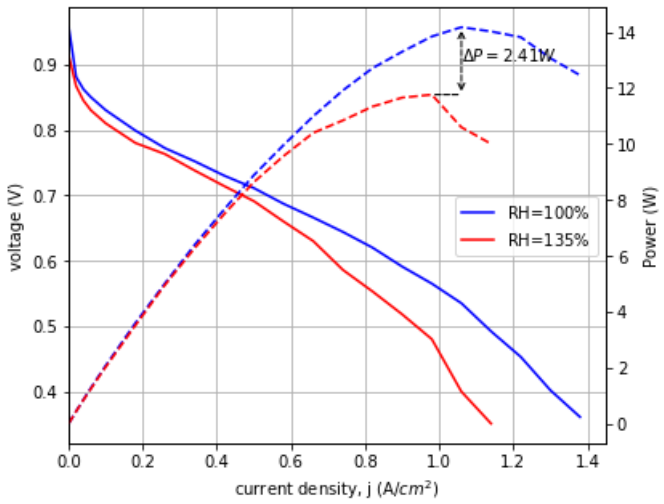

Fig. 6.8: Polarisation curve showing the power loss due to flooding.

polarisation curve for each of the results shown relative to the normal operational condition. It is important to note that the voltage drop in the case of flooding is mostly manifested in the mass transport region. The intermediate region (ohmic) region does not experience a significant variation. Water accumulation in the gas flow channels tend to block the passage of reactants to the catalyst area where they may be used up. This occurs as a result of water cooling off to form liquid in the gas channels due to the lower temperature in the flow channels relative to the humidifier temperatures. This series of events result in an overall performance loss arising from mass transport issues, hence the large variation observed in the polarisation curve in the region.

To elucidate on the losses due to flooding, Fig. 6.8 compares the maximum power point for the normal and flooding conditions as derived from the polarisation curve.

For the polarisation curve obtained for normal operation, it is seen that a maximum power of about 14.2W is obtained compared to that the flooding scenario of about 11.8W, giving a loss of 2.4W loss.

Impedance data obtained using the multi-sine perturbation signal are plotted alongside those obtained by the FRA system as shown in Fig. 6.9. Measurements were taken at 250mA/cm^2 current density set point.

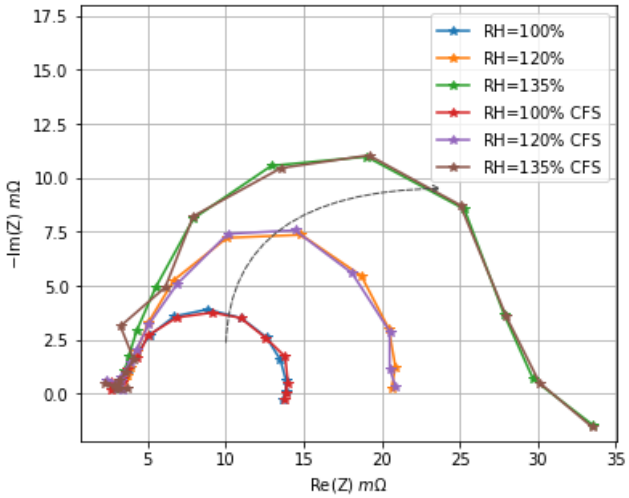

Fig. 6.9: Nyquist plot for different levels of flooding.

First it may be observed that the multi-sine approach implemented using the active load device yields very similar results to those for the FRA. Measurement time is however reduced significantly with the proposed method and the portable active load device also affords the required flexibility. From the Nyquist plot, it is seen that there is a significant difference in the overall size, particularly the increase in radius for increasing levels of flooding. This indicates in increase in the charge transfer resistance which occurs as a result of flooding of the electrode. With the humidifier temperature maintained above 100^0C to enforce flooding, the flow line temperature is further reduced to create severe flooding conditions. As had been mentioned earlier and noted by [42], severe flooding conditions would result in increased level of non-linearity. As such, EIS using the single sine is significantly affected. However, given the short time afforded by the multi-sine signal and the noise rejection capabilities proposed, results were obtained under the severe flooding conditions. The result is presented in Fig. 6.10. Results could not be achieved from the Fuelcon test station under these conditions for comparison due to system enforced constraints. However, the plot shown in the Fig. 6.10 indicates a reasonable trend following from milder flooding scenarios in Fig. 6.9. This result is particularly important for online diagnostics where it is necessary to estimate the impedance even in the event of such extreme conditions.

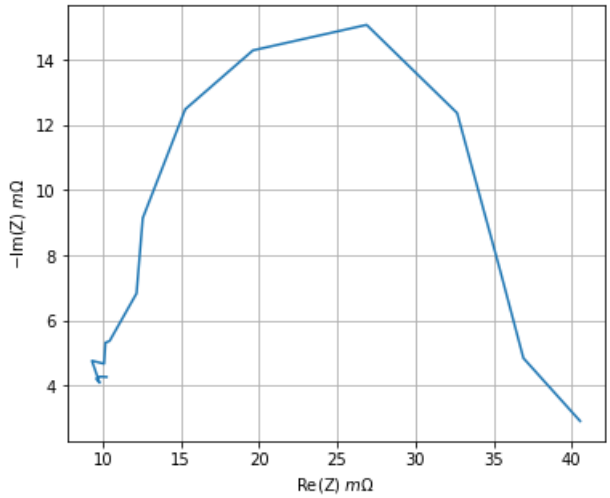

Fig. 6.10: Nyquist plot representing Impedance data for an excessive flooding scenario.

Drying was also initiated according to the procedure previously discussed. This was gradually effected by reducing the humidifier temperature and taking measurements. A major impact of drying is its effect on the membrane. For the passage of ions, the membrane requires adequate humidification. In the event of drying, this is inhibited, resulting to an increased resistance.

The polarisation curve is shown in Fig. 6.11 for different levels of drying which is dictated by the relative humidity. It can be observed that there is a significant shift mostly around the intermediate region of the polarisation curve indication an ohmic drop as the relative humidity decreases.

To elucidate on the losses due to drying, Fig. 6.12 compares the maximum power point for the normal and drying conditions as derived from the polarisation curve. For the polarisation curve obtained for normal operation, it is seen that a maximum power of about 14.2W is obtained compared to that the drying scenario of about 8.54W, giving a loss of 5.6W loss. Impedance results are also represented in the form of Nyquist plots here in Fig. 6.13. It is also observed that drying results in a shift in the high frequency intercept of the Nyquist plot

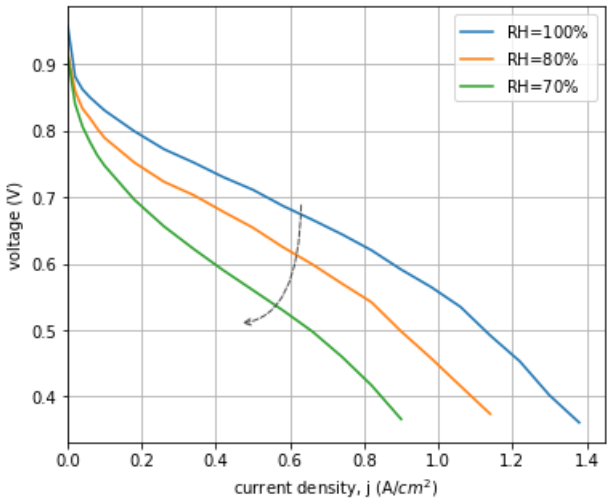

Fig. 6.11: Polarisation curve showing the current voltage relationship for different levels of drying.

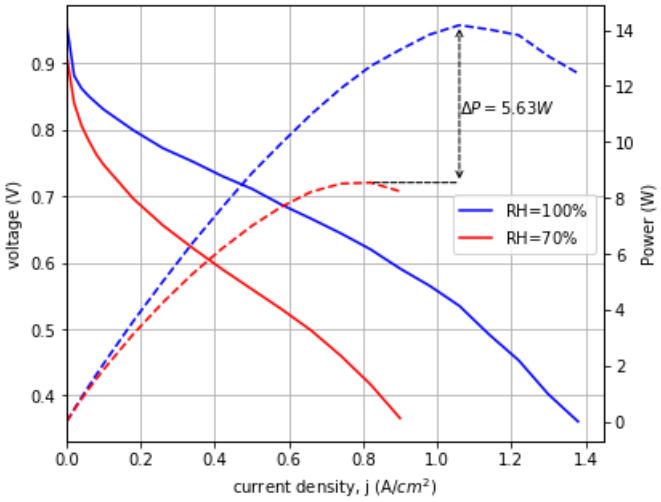

Fig. 6.12: Polarisation curve showing the power loss due to drying.

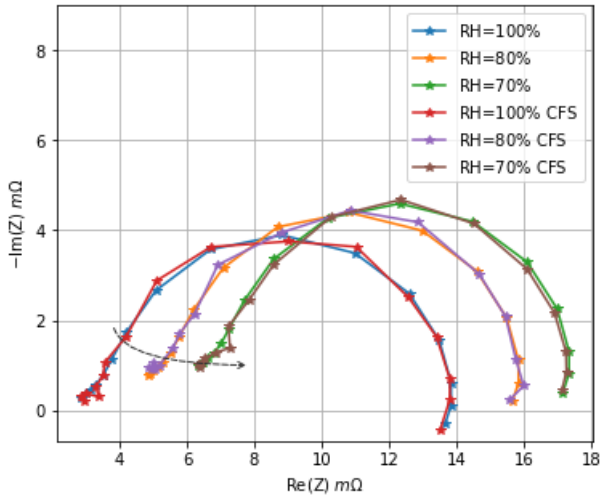

Fig. 6.13: Nyquist plot for different levels of drying.

which follows from the increased ohmic resistance. Compared to the flooding case, it is also observed that the overall size for the drying fault condition does not vary significantly. Finally we compare impedances for normal flooding and drying condition in Fig. 6.14. The characteristic large radius of the Nyquist is evident for the flooding case. The drying case includes a shift on the real axis but with a relatively minimal change in radius compared to the flooding result.

6.6 Conclusion

An improved multi-sine impedance spectroscopy scheme has been proposed. This reduces the time cost of the measurement by several orders of magnitude. In this work specifically, measurements were carried out in less than 4 seconds compared to conventional EIS which could take several minutes. Two major fault conditions of the PEMFC are also considered. Faults occurring in the fuel cell system mostly manifest as a voltage drop. For a fuel cell in operation, a drop in voltage below an operating point is an indication of the occurrence of a faulty condition. Beyond this however, it is necessary to identify the particular fault condition in order to inform mitigation. It has been shown that impedance estimation offers tremendous

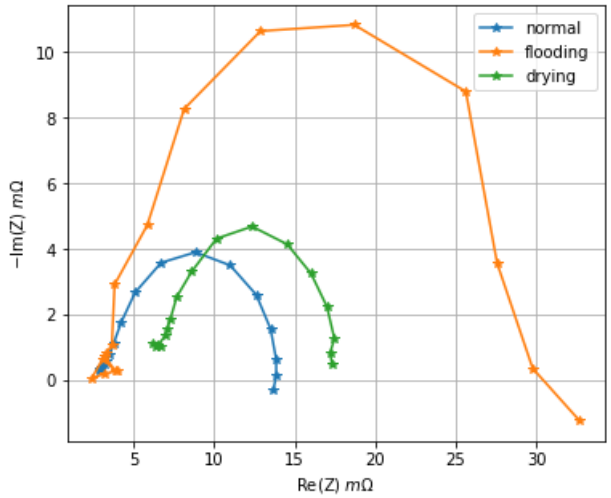

Fig. 6.14: Nyquist plot for normal, flooding and drying scenarios.

support for distinguishing between either case of flooding or drying while providing useful markers. Such information may be fed to actuators to ensure fault correction or mitigating strategies.

Chapter 7

Time-Frequency Analysis of the Chirp Response for Rapid Electrochemical Impedance Estimation

7.1 Introduction

Given the findings discussed in the previous chapters, the Electrochemical Impedance Spectroscopy (EIS) shows potential to be adapted as an in-situ measurement technique for on-line condition monitoring with minimal disturbance [56]. However several factors need to be considered such as the time cost of the measurements which this work focuses on improving. The multi-sine signal technique which combines the required sinusoidal perturbation into one single perturbation helps to reduce the measurement time significantly. However, other problems arise, such as the harmonic distortion effect discussed in the previous chapter. Although, the proposed frequency distribution in the previous chapter makes effort to reduce this impact of the overall impedance, the effects are not completely eliminated. The rest of this Chapter presents the proposed approach which employs a different perturbation signal type - a chirp. Furthermore, the use of the wavelet transform as an analysis tool of choice is presented. The characteristic nature of the chirp signal makes for a broadband frequency sweep over time possible, hence enabling a faster impedance estimation. Useful information

is gained by the localisation of the signal vectors in both the time and frequency space employing the continuous wavelet transform for analysis and the resulting decomposition is then harnessed for impedance calculation. This approach is first tested in simulation and results for the equivalent circuit are shown. It is shown that the generated impedance well approximates the theoretical values. Various conditions are considered in evaluating the proposed techniques. The technique is then further tested on a developed rig to demonstrate its practical use and short measurement time, whereby results show good performance relative to a commercial frequency response analyser (FRA) implementing the single sine technique.

7.2 Proposed Method

This work seeks to address the time requirement of the EIS measurement. It does so by proposing the development of a rapid measurement technique that avails the EIS for online fault diagnostic applications. The work develops in two parts. First the chirp signal is considered as an alternative for the discrete frequency signals in the case of a multi-sine perturbation signal and the single sine EIS. This consideration is made given the rich frequency content of the chirp signal in a given time measure. The wavelet transform is then introduced as an analysis tool of choice. These combined provides a novel approach to estimating device impedance for online use.

7.2.1 The Chirp Signal

The chirp is used to describe a signal whose frequency increases or decreases as a function of time. It may be mathematically described by (7.1).

$$y(t) = \cos\left(2\pi f_i(t)t + \phi_0\right) \tag{7.1}$$

$$f_i(t) = f_0 \times \beta^t \tag{7.2}$$

where,

$$\beta = \left(\frac{f_1}{f_0}\right)^{\frac{1}{t_1}}$$

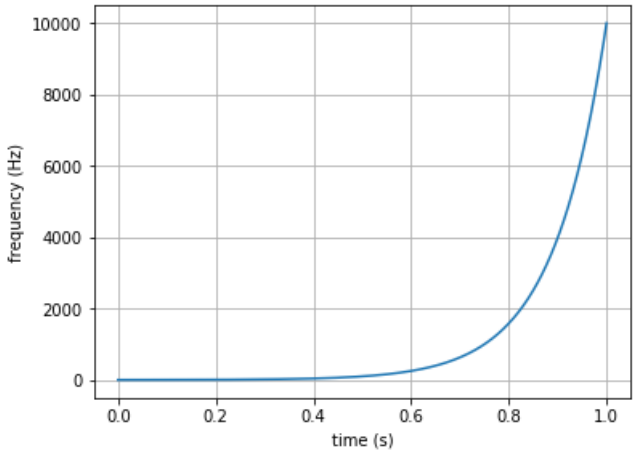

Fig. 7.1: The frequency sweep of the defined exponential chirp as a function of time.

Depending on the rate of frequency sweep, different categories of chirp signals include the linear, exponential and quadratic [65]. In choosing the desired frequency function, we consider the frequency range and distribution necessary to achieve suitable resolution required for the EIS as well as the corresponding frequency sweep time. Considering fuel cell impedance characteristics in general, the linear chirp for instance is considered unsuitable since a longer time may be necessary to sweep the frequency range of interest. Ideally the required function should grow slowly from the low-frequency region and ramp up rapidly at intermediate frequencies towards the higher frequencies. The exponential chirp offers this characteristic as shown in Fig. 7.1.

The instantaneous frequency for an exponential chirp could be described mathematically as in (7.2). f_0, f_1 are start and target frequency points for a target time t_1. This time-dependent frequency characteristic makes it possible to span a wide frequency range within a short time span. The chirp has been investigated for fuel cell impedance estimation using the FFT for analysis [80]. The drawback with this is the loss in accuracy in the high frequency region. An interesting implementation for the analysis of the chirp signal for impedance calculation has been proposed [69]. The signal envelopes of the current and voltage responses are used to approximate the amplitude of the signal and the phase derived from the analytical formula. Though this method was shown to perform well with simulation results, the authors however

noted some challenges in the determination of the phases leading to computational overheads.

For a sufficiently detailed analysis of the chirp signal, a time-frequency paradigm is necessary. Due to its non-stationary characteristics, the DFT is not suitable as it obfuscates the time information. Hence, the signal needs to be characterised in both time and frequency for details. The Short Time Fourier Transform (STFT) is used extensively for time-frequency analysis. The trade-off here is between a complete obfuscation of frequency in time domain and that of time in frequency domain. Equation (7.3) expresses this constraint.

$$\Delta t \times \Delta f = 2\pi \tag{7.3}$$

Where Δt and Δf are the time and frequency resolutions respectively. To achieve this, the entire signal length is divided into pieces and the DFT calculated for each piece. This helps to retain some time information. However, the STFT suffers from issues such as window determination in size and type which have significant effect of the transformed signal. To attempt to resolve the issues associated with the STFT, the wavelet transform has been introduced. This will now be discussed in more detail in the proceeding section.

7.2.2 The Wavelet Transform

The wavelet transform allows for a more precise time-frequency localisation of a non-stationary signal such as the chirp. It has been deployed in various disciplines for transient detection as well as in analysis of geophysical phenomena [81]. The wavelet transform is achieved by dilation and translation of a wavelet basis - a function of zero average [82]. For the analysis, a suitable wavelet basis must be chosen. Four factors that should be considered in the choice of a wavelet basis. These include orthogonality, whether it is complex or real, the width and the shape [83]. Orthogonal bases are often a desire in signal processing for efficient encoding of signal information. A complex wavelet function returns the complex coefficients useful in the determination of the magnitude and phase. The generalised Morse

wavelets are a family of complex-valued wavelets with parameters well defined for tuning to achieve a suitable basis. The MATLAB implementation for finite length signal has thus been employed in this chapter.

A wavelet function may be described as in (7.4) where the dilation and translation parameters are represented as s and u respectively [82].

$$\psi_{u,s}(t) = \frac{1}{\sqrt{s}}\psi(\frac{t-u}{s}) \tag{7.4}$$

For a given signal $x(t)$ therefore, the wavelet transform, $W_f(u,s)$ may be given as the inner product of the signal with $\psi_{u,s}(t)$.

$$W_f(u,s) = \int_{-\infty}^{\infty} x(t)\frac{1}{\sqrt{s}}\psi^*(\frac{t-u}{s})dt \tag{7.5}$$

7.2.3 Impedance Estimation

The continuous wavelet transform of the chirp signal yields a time-frequency grid of complex coefficients. For impedance measurement, it is necessary to analyse both the excitation and the response signals. The time-frequency mapping of the time domain chirp signal in (7.2) is used to jointly locate the coefficients to the nearest frequency and time points This is expressed in the following equations. The co-efficient for a given frequency f and time t is approximated by $f' \in F$ and $t' \in T$ as dictated by (7.6).

$$|f - f'| = \min|f - F| \text{ and } |t - t'| = \min|t - T| \tag{7.6}$$

where,

$$t = \frac{\log(\frac{f_i(t)}{f_0})}{\log\beta}$$

F & T are arrays of frequency and time coefficients respectively, $|f - F|$ denotes a set consisting of the difference between frequency, f and each element of array F and $|t - T|$ denotes a set consisting of the difference between time, t and each element of array T. This

approximation relies on two conditions. Firstly, that there is low variance in the coefficients in the frequency band for the desired frequency. Secondly, that the impedance of the system will vary relatively smoothly for a slight change in frequency as dictated by the wavelet frequency bins. The coefficients $W_i(t,f)$ and $W_v(t,f)$ are extracted for both the input and response signals respectively and the impedance z for each frequency is given by (7.7).

$$z(t,f) = \frac{W_v(t,f)}{W_i(t,f)} \tag{7.7}$$

7.3 Results and Discussion

7.3.1 Impedance Simulation

In order to test the efficacy of the proposed approach, commonly used fuel cell equivalent circuits models like the Randles circuit (discussed in section 3.3.5) which consists of a resistor in series with a parallel arrangement of a resistor and capacitor, are employed. The chirp excitation is of 1s sweep time for frequency range of 0.1Hz - 10kHz for all results shown. Equivalent circuit elements have been limited to resistors, capacitors and inductors for simulation in the Simulink environment. A sample perturbation and response time domain signal is shown in Fig. 7.2 with the corresponding wavelet transform shown in the spectrogram plot of Fig. 7.3. Fig. 7.4 shows the master circuit in the subsystem used to generate other circuits according to values in Table 7.1. These values represent predetermined characteristics describe in [69]. The proposed technique is first implemented for circuits 0, 1 & 2 as described by table. It is shown in Fig. 7.5 that the resulting impedance curve derived from the proposed method closely approximates the theoretical impedance for each of the circuits. This shows the accuracy of the proposed approach for impedance measurement of

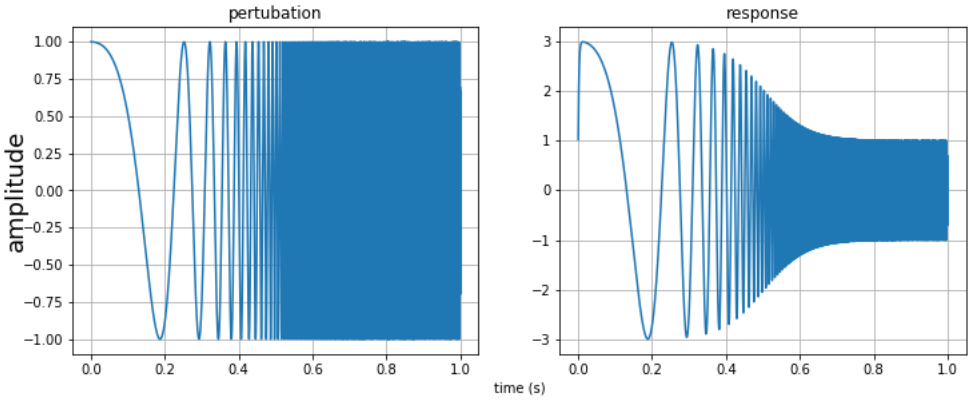

Fig. 7.2: Chirp perturbation and response signal as obtained from the simulation.

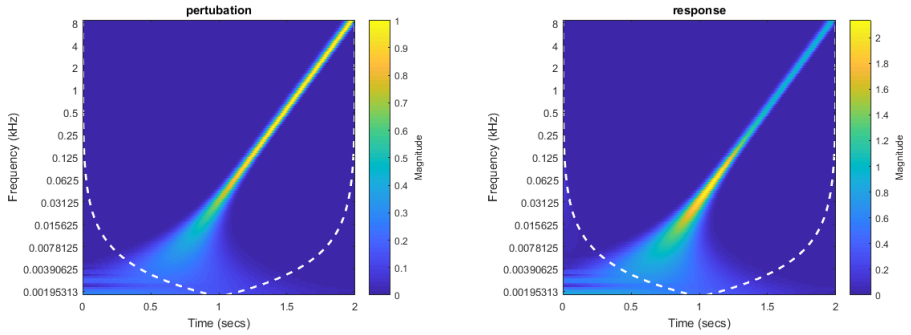

(a) (b)

Fig. 7.3: Spectrogram of the perturbation signal (a) and the corresponding response (b).

the fuel cell.

Impedance data are often used to extract useful diagnostic and characterisation information by studying relative variations or monitoring parameter changes. This is simulated by changing different parameters in the equivalent circuits, the corresponding Nyquist plots exhibits slight changes in shapes. It is shown in Fig. 7.6 for circuits 3-9 that the impedance estimation

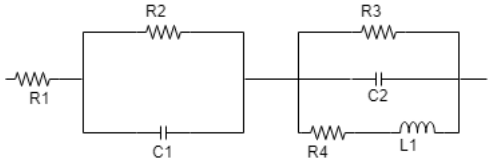

Fig. 7.4: Master circuit used to derive other circuits for validation.

Table 7.1: Component values for circuits.

no.	$R_1(\Omega)$	R_2	R_3	$C_1(mF)$	C_2	R_4	$L_1(H)$
0	1	2	short	1	open	open	open
1	1	1	2	1	5	open	open
2	13	2	short	0.16	open	4	0.01
3	1	1	short	1	open	open	open
4	1.2	1	short	1	open	open	open
5	1.6	1	short	1	open	open	open
6	1	1.2	short	1	open	open	open
7	1	1.6	short	1	open	open	open
8	1	1	short	5	open	open	open
9	1	1	short	10	open	open	open

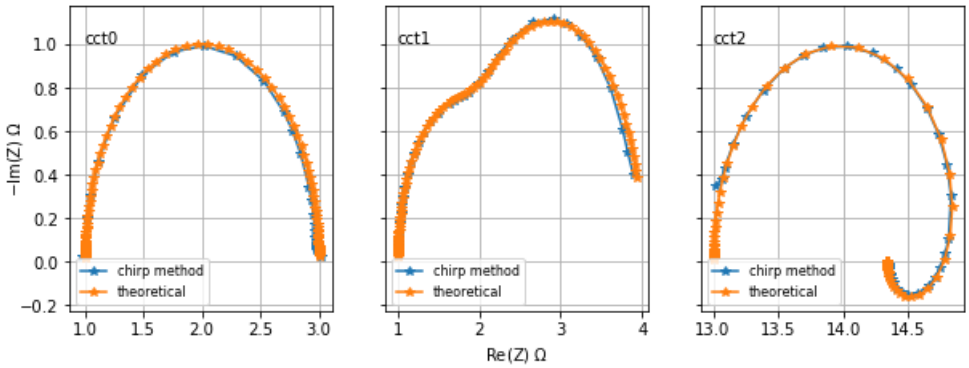

Fig. 7.5: Impedance plots compared for the chirp method and theoretical values.

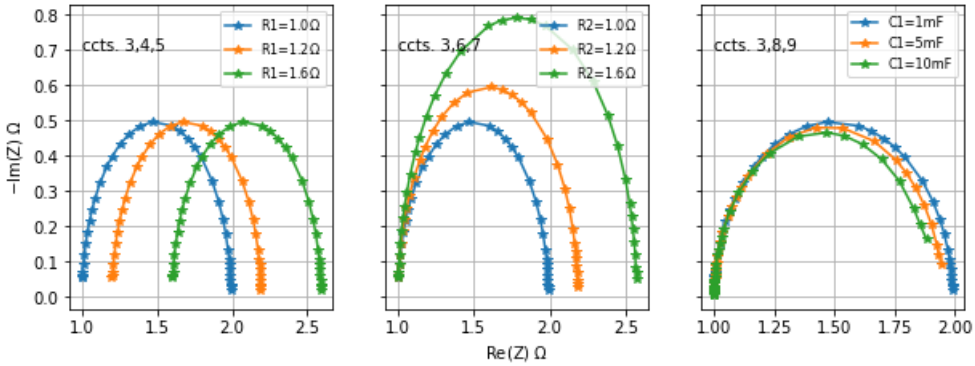

Fig. 7.6: Influence of parameter changes on Nyquist plot useful for diagnostics.

technique shows sensitivity to parameter changes as expected.

7.3.2 Noise Tolerance

It is also necessary that the proposed approach is considered for conditions such as noise that may occur in practical applications. To realise this effect, we consider the clean signal with an additive white Gaussian noise. The noisy signal is synthesised using the signal to noise ratio (SNR) as described in (7.8). Furthermore, different noise levels are implemented with the corresponding noisy signals used to determine the impedance as described above. The results are then analysed for performance limits.

$$SNR_{dB} = 10\log_{10}(\frac{A_{signal}}{A_{noise}})^2 \tag{7.8}$$

The wavelet transform tends to be sensitive to noise [83] which may compromise the impedance measurement as had been previously described. For the wavelet transform of a noisy signal, locating the wavelet co-efficient according to (7.6) may yield spurious results. To address this problem, we analyse the distribution of the magnitude coefficients around the points determined by the time-frequency co-located coefficients. Fig. 7.7 shows the magnitude for 30 frequency points near (either side) a sample frequency point located in time. It is seen that the magnitude slowly rolls off on either side of the of the frequency point. We harness this pattern to improve the selection of coefficients to guard against anomalous or outlier coefficients which may occur as a result of the sensitivity of the wavelet transform to a noisy signal.

Let us consider a neighbourhood of n frequency points around the desired frequency. For a valid coefficient the pattern should be similar to Fig. 7.7. To enforce this characteristic, we require that the standard deviation of the magnitude of the n points around the frequency of

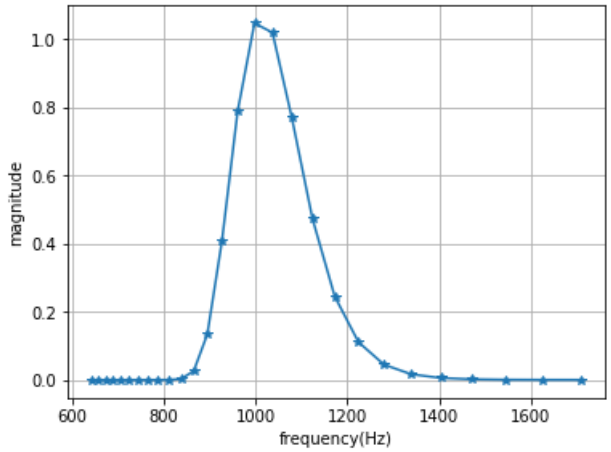

Fig. 7.7: Frequency magnitude around a time located frequency point of 1000Hz.

interest be less than a chosen value as follows;

Let c_i be the coefficient at a time located frequency of interest f_i, then we define the coefficients C_n in the neighbourhood of f_i as given by:

$$C_n = \{c_{i-\lfloor \frac{n}{2} \rfloor}, \ldots, c_i, \ldots, c_{i+\lfloor \frac{n}{2} \rfloor}\} \tag{7.9}$$

and require that standard deviation $\sigma_{C_n} < \sigma_{thresh}$.
Desired frequency points used whose coefficients are used to compute the impedance may now be validated using the above approach given the large number of discrete frequency choices that may be made within the band of interest.

Fig. 7.8 shows the resulting Nyquist plot for varying SNR. For these results 10 points around the desired frequency point is considered for each frequency. To determine σ_{thresh}, the mean of the distribution of the magnitudes without noise is considered to set a minimum value of 0.28 for σ_{thresh}. This threshold is gradually relaxed by increasing in steps of 0.1 until the number of desired discrete points are gotten. For these results, σ_{thresh} has been determined to be 0.35. While the effect of reducing SNR is noticeable, it is seen that the resulting Nyquist plot closely follows the theoretical plot.

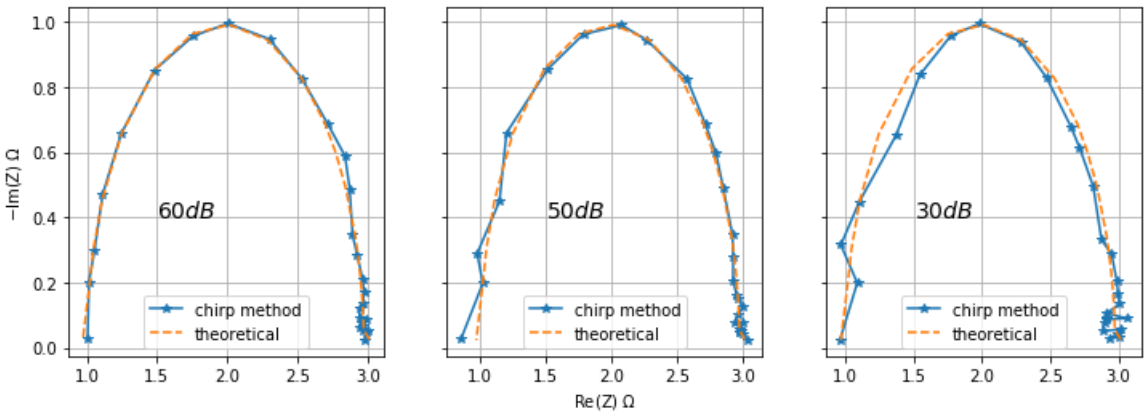

Fig. 7.8: Nyquist plot for different values of signal to noise ratio showing the performance of the proposed approach in the presence of noise.

7.3.3 Fuel Cell Test

Finally, the technique is implemented on an impedance measurement setup for a fuel cell which is as developed in [84]. The rig to be employed for carrying out the experimental investigation includes a Baltic fuel cell test assembly interfaced with a Fuelcon test station as already shown in Fig. 5.17. For the fuel cell the amplitude perturbation signal, it is a compromise between the linearity requirements and the SNR ratio. For this work, the chirp amplitude has been limited to 0.1A where suitable performance was derived following the THD tests shown in Fig. 5.19. While other conditions required for normal operation of the fuel cell were maintained, the system was perturbed with a chirp input swept from 0.1Hz - 10kHz in a time of 2 seconds and the corresponding response acquired. Acquisition of the signal was done at 20kHz and the resulting time domain signal and time-frequency domain representation are shown in Fig. 7.9. Computation of impedance was done as previously described and the impedance plot is shown in Fig. 7.10. The results as shown demonstrates the potential capability for use in the estimation of fuel cell or similar electrochemical systems impedance.

The advantages of this impedance estimation approach stem from the characteristics of the chirp signal and the wavelet transform as an analysis tool. It reduces the time required for impedance estimation by orders of magnitude relative to the single sine technique. The

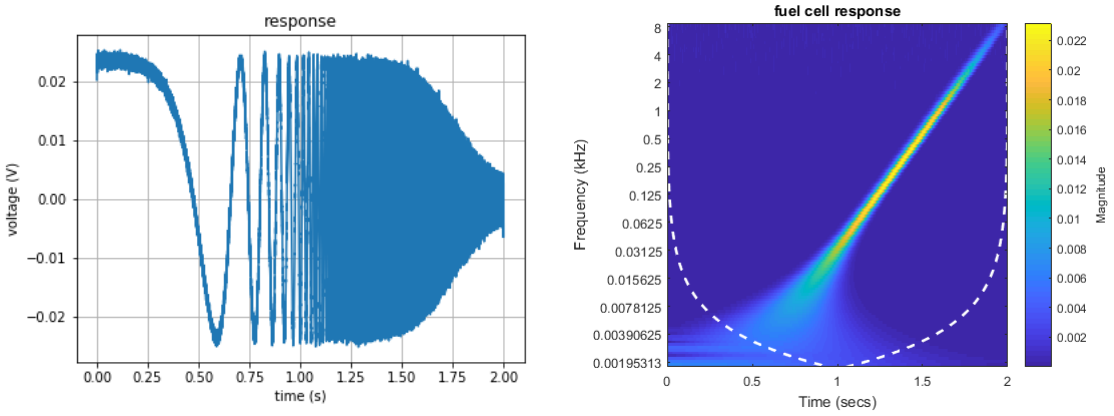

(a) (b)

Fig. 7.9: Fuel cell response (a) and corresponding spectrogram (b)

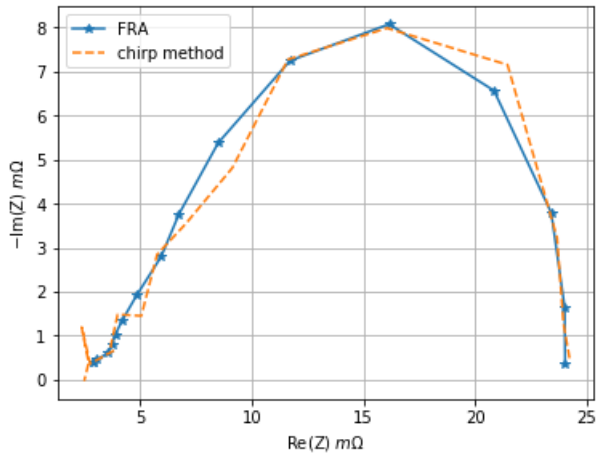

Fig. 7.10: Nyquist plot showing results achieved using a commercial FRA and the chirp method implemented with an active load.

chirp excitation also compares favourably with other approaches such as the multi-sine in its frequency content for impedance information. The one-to-one time-frequency mapping means a wide range of frequencies could be contained in a short time. The multi-sine technique takes a linear combination of discrete frequency points leading to increased amplitude which compromises linearity assumption for impedance. Also, minimum time limit for the multi-sine technique is still largely dictated by the lowest frequency which may be a few seconds. The wavelet transform as a signal processing tool also allows improved accuracy compared to other signal processing method such as the STFT. Furthermore, the chirp signal effectively makes for a smooth spectrum for the duration of the signal. This may be useful for impedance estimates where there is high variance in the frequency to frequency response where interpolation results in significant errors.

7.4 Conclusion

The proposed approach is a novel technique for rapid impedance estimation. As demonstrated, the technique can estimate the impedance for a fuel cell a time of about 2 seconds with significant accuracy. It draws from the time-frequency analysis of the frequency-rich chirp signal using the continuous wavelet transform. This enables the detailed analysis of the chirp signals with a localisation of frequency coefficients in both time and frequency. These coefficients are extracted by an approximate scale and time approach utilising the one-to-one mapping of the chirp signal and impedance is computed. Results are shown for fuel cell model circuits demonstrating the ability to match varying models as well as sensitivity to parameter change for a given model. The technique is thus suitable for purposes of real-time diagnostics as well as characterisation given its speed and accuracy.

Chapter 8

Closure

8.1 Conclusions

Techniques aimed at monitoring the fuel cell state of health have been investigated in this work. The fuel cell is reviewed as an electrochemical system alongside its various diagnostic and measurement techniques. Simulations were carried out to demonstrate proposed approaches aimed at improving existing methods. Experiments are also carried out on an actual fuel cell system to show practicality of the techniques developed in this work.

The impedance spectroscopy has been reviewed and investigated as a desired measurement technique able to provide useful insight towards diagnosis of faults in fuel cells. Given its importance, techniques aimed at improving the EIS for practical implementation have been presented. Towards this, two key characteristics are improved which are the measurement time and accuracy. The accuracy concerns of the multi-frequency perturbation is investigated and a solution is proposed in the distribution of the frequency components. This offers significant improvements in accuracy when compared to existing approaches. This improvement in accuracy is particularly vital when impedance results are to be deployed for diagnostic purposes.

A low-cost active load device is also designed to implement the load modulation techniques enabling the implementation of the approaches proposed in this work. The device showed acceptable performance when compared to those obtained from a commercial FRA for reproducible tests carried out with equivalent circuits.

Using the proposed approach, insights have been developed into the fault characteristics of the fuel cell for flooding and drying scenarios which are two major fault conditions associated with the PEMFC. These scenarios are studied by analysing polarisation curves and Nyquist analysis of the results show clear fault characteristics which could be deployed for detection as well as isolation of the drying and flooding fault condition. In addition, results showed that the measurements were comparable to the single sine technique implemented with the FRA and even under highly non-linear conditions of flooding.

8.2 Recommendations For Future Work

This work has developed techniques aimed at improving fuel cell diagnostics. The PEMFC has been investigated as the subject fuel cell type. To extend this work, the techniques developed may be deployed on other fuel cell types. The impedance spectroscopy is a also applicable to battery testing, as such, techniques developed in this work could also be applied to battery applications. Finally, since some portions of this work contributes towards improved accuracy while shortening measurement times, the techniques could be incorporated into existing diagnostic frameworks.

References

[1] Frano Barbir. *PEM fuel cells: theory and practice*. Academic Press, 2012.

[2] Andrew Dicks and David Anthony James Rand. *Fuel cell systems explained*. Wiley Online Library, 2000.

[3] Ryan O'hayre, Suk-Won Cha, Fritz B Prinz, and Whitney Colella. *Fuel cell fundamentals*. John Wiley & Sons, 2016.

[4] Etienne Dijoux, Nadia Yousfi Steiner, Michel Benne, Marie-Cécile Péra, and Brigitte Grondin Pérez. A review of fault tolerant control strategies applied to proton exchange membrane fuel cell systems. *Journal of Power Sources*, 359:119–133, 2017.

[5] Anant Agarwal and Jeffrey Lang. *Foundations of analog and digital electronic circuits*. Morgan Kaufmann, 2005.

[6] R David Middlebrook. Measurement of loop gain in feedback systems. *International Journal of Electronics Theoretical and Experimental*, 38(4):485–512, 1975.

[7] Haijiang Wang, Hui Li, and Xiao-Zi Yuan. *PEM fuel cell failure mode analysis*, volume 1. CRC Press, 2011.

[8] Frank de Bruijn. Pemfc lifetime and durability an overview. Application note, Nedstack, September 2011.

[9] Brian Bullecks, Raghunathan Rengaswamy, Debangsu Bhattacharyya, and Gregory Campbell. Development of a cylindrical pem fuel cell. *International Journal of Hydrogen Energy*, 36(1):713–719, 2011.

[10] Rosa Elvira Silva, Fabien Harel, Samir Jemei, Raphaël Gouriveau, Daniel Hissel, Loïc Boulon, and Kodjo Agbossou. Proton exchange membrane fuel cell operation and degradation in short-circuit. *Fuel Cells*, 14(6):894–905, 2014.

[11] N Yousfi-Steiner, Ph Moçotéguy, D Candusso, and D Hissel. A review on polymer electrolyte membrane fuel cell catalyst degradation and starvation issues: Causes, consequences and diagnostic for mitigation. *Journal of Power Sources*, 194(1):130–145, 2009.

[12] Hui Li, Yanghua Tang, Zhenwei Wang, Zheng Shi, Shaohong Wu, Datong Song, Jianlu Zhang, Khalid Fatih, Jiujun Zhang, Haijiang Wang, et al. A review of water flooding issues in the proton exchange membrane fuel cell. *Journal of Power Sources*, 178(1):103–117, 2008.

[13] Frano Barbir, H Gorgun, and Xinting Wang. Relationship between pressure drop and cell resistance as a diagnostic tool for pem fuel cells. *Journal of Power Sources*, 141(1):96–101, 2005.

[14] Dongryul Lee and Joongmyeon Bae. Visualization of flooding in a single cell and stacks by using a newly-designed transparent pemfc. *International Journal of Hydrogen Energy*, 37(1):422–435, 2012.

[15] Akira Taniguchi, Tomoki Akita, Kazuaki Yasuda, and Yoshinori Miyazaki. Analysis of degradation in pemfc caused by cell reversal during air starvation. *International Journal of Hydrogen Energy*, 33(9):2323–2329, 2008.

[16] Jinfeng Wu, Xiao Zi Yuan, Haijiang Wang, Mauricio Blanco, Jonathan J Martin, and Jiujun Zhang. Diagnostic tools in pem fuel cell research: Part i electrochemical techniques. *International journal of hydrogen energy*, 33(6):1735–1746, 2008.

[17] Junbo Hou. A study on polarization hysteresis in pem fuel cells by galvanostatic step sweep. *International Journal of Hydrogen Energy*, 36(12):7199–7206, 2011.

[18] Tuomas Mennola, Mikko Mikkola, Matti Noponen, Tero Hottinen, and Peter Lund. Measurement of ohmic voltage losses in individual cells of a pemfc stack. *Journal of power sources*, 112(1):261–272, 2002.

[19] Felix N Büchi, Alois Marek, and Günther G Scherer. In situ membrane resistance measurements in polymer electrolyte fuel cells by fast auxiliary current pulses. *Journal of the Electrochemical Society*, 142(6):1895–1901, 1995.

[20] Raffaele Petrone, Zhixue Zheng, Daniel Hissel, Marie-Cécile Péra, Cesare Pianese, Marco Sorrentino, Mohamed Becherif, and N Yousfi-Steiner. A review on model-based diagnosis methodologies for pemfcs. *International Journal of Hydrogen Energy*, 38(17):7077–7091, 2013.

[21] Rolf Isermann. Model-based fault-detection and diagnosis–status and applications. *Annual Reviews in control*, 29(1):71–85, 2005.

[22] D Hissel, MC Péra, and JM Kauffmann. Diagnosis of automotive fuel cell power generators. *Journal of Power sources*, 128(2):239–246, 2004.

[23] T Escobet, D Feroldi, S De Lira, V Puig, J Quevedo, J Riera, and M Serra. Model-based fault diagnosis in pem fuel cell systems. *Journal of Power Sources*, 192(1):216–223, 2009.

[24] Michael Buchholz, Mathias Eswein, and Volker Krebs. Modelling pem fuel cell stacks for fdi using linear subspace identification. In *Control Applications, 2008. CCA 2008. IEEE International Conference on*, pages 341–346. IEEE, 2008.

[25] Thamo Sutharssan, Diogo Montalvao, Yong Kang Chen, Wen-Chung Wang, Claudia Pisac, and Hakim Elemara. A review on prognostics and health monitoring of proton exchange membrane fuel cell. *Renewable and Sustainable Energy Reviews*, 75:440–450, 2017.

[26] N Yousfi Steiner, D Hissel, Ph Moçotéguy, and Denis Candusso. Diagnosis of polymer electrolyte fuel cells failure modes (flooding & drying out) by neural networks modeling. *International Journal of Hydrogen Energy*, 36(4):3067–3075, 2011.

[27] Z Zheng, R Petrone, MC Pera, D Hissel, M Becherif, and C Pianese. Diagnosis of a commercial pem fuel cell stack via incomplete spectra and fuzzy clustering. In *Industrial Electronics Society, IECON 2013-39th Annual Conference of the IEEE*, pages 1595–1600. IEEE, 2013.

[28] Christian Jeppesen, Samuel Simon Araya, Simon Lennart Sahlin, Sobi Thomas, Søren Juhl Andreasen, and Søren Knudsen Kær. Fault detection and isolation of high temperature proton exchange membrane fuel cell stack under the influence of degradation. *Journal of Power Sources*, 359:37–47, 2017.

[29] Elodie Pahon, Samir Jemei, Fabien Harel, Rosa Elvira Silva, Latifa Oukhellou, and Daniel Hissel. k-nearest neighbours fault diagnosis of proton exchange membrane fuel cell. In *IDHEA*, page 9p, 2014.

[30] Daniel Hissel, Denis Candusso, and Fabien Harel. Fuzzy-clustering durability diagnosis of polymer electrolyte fuel cells dedicated to transportation applications. *IEEE Transactions on Vehicular Technology*, 56(5):2414–2420, 2007.

[31] Zhixue Zheng, Marie-Cécile Péra, Daniel Hissel, Mohamed Becherif, Kréhi-Serge Agbli, and Yongdong Li. A double-fuzzy diagnostic methodology dedicated to online fault diagnosis of proton exchange membrane fuel cell stacks. *Journal of Power Sources*, 271:570–581, 2014.

[32] N Fouquet, C Doulet, C Nouillant, G Dauphin-Tanguy, and B Ould-Bouamama. Model based pem fuel cell state-of-health monitoring via ac impedance measurements. *Journal of Power Sources*, 159(2):905–913, 2006.

[33] Abdellah Narjiss, Daniel Depernet, Denis Candusso, Frederic Gustin, and Daniel Hissel. Online diagnosis of pem fuel cell. In *Power Electronics and Motion Control Conference, 2008. EPE-PEMC 2008. 13th*, pages 734–739. IEEE, 2008.

[34] Zhixue Zheng, Raffaele Petrone, Marie-Cécile Péra, Daniel Hissel, Mohamed Becherif, Cesare Pianese, N Yousfi Steiner, and Marco Sorrentino. A review on non-model based diagnosis methodologies for pem fuel cell stacks and systems. *International Journal of Hydrogen Energy*, 38(21):8914–8926, 2013.

[35] Leo H Chiang, Evan L Russell, and Richard D Braatz. Fault diagnosis in chemical processes using fisher discriminant analysis, discriminant partial least squares, and principal component analysis. *Chemometrics and intelligent laboratory systems*, 50(2):243–252, 2000.

[36] Luis Alberto M Riascos, Marcelo G Simoes, and Paulo E Miyagi. On-line fault diagnostic system for proton exchange membrane fuel cells. *Journal of Power Sources*, 175(1):419–429, 2008.

[37] Rolf Isermann. *Fault-diagnosis systems: an introduction from fault detection to fault tolerance*. Springer Science & Business Media, 2006.

[38] Nadia Yousfi Steiner, Daniel Hissel, Philippe Moçotéguy, and Denis Candusso. Non intrusive diagnosis of polymer electrolyte fuel cells by wavelet packet transform. *International Journal of Hydrogen Energy*, 36(1):740–746, 2011.

[39] E Pahon, N Yousfi Steiner, S Jemei, D Hissel, and P Moçoteguy. A signal-based method for fast pemfc diagnosis. *Applied Energy*, 165:748–758, 2016.

[40] MA Rubio, K Bethune, A Urquia, and J St-Pierre. Proton exchange membrane fuel cell failure mode early diagnosis with wavelet analysis of electrochemical noise. *International Journal of Hydrogen Energy*, 41(33):14991–15001, 2016.

[41] Cédric Damour, Michel Benne, Brigitte Grondin-Perez, Miloud Bessafi, Daniel Hissel, and Jean-Pierre Chabriat. Polymer electrolyte membrane fuel cell fault diagnosis based on empirical mode decomposition. *Journal of Power Sources*, 299:596–603, 2015.

[42] Chris De Beer. *CONDITION MONITORING OF POLYMER ELECTROLYTE MEMBRANE FUEL CELLS*. PhD thesis, UCT, 2014.

[43] Alan V Oppenheim, Alan S Willsky, and I Young. Signals and systems. 1983. *and*, 459(461):19, 1983.

[44] Evgenij Barsoukov and J Ross Macdonald. *Impedance spectroscopy: theory, experiment, and applications*. John Wiley & Sons, 2005.

[45] Kazimierz Darowicki. The amplitude analysis of impedance spectra. *Electrochimica acta*, 40(4):439–445, 1995.

[46] J-P Diard, B Le Gorrec, C Montella, and P Landaud. Constant load vs constant current eis study of electrochemical battery discharge. *Electrochimica acta*, 42(23-24):3417–3420, 1997.

[47] GS Popkirov and RN Schindler. Effect of sample nonlinearity on the performance of time domain electrochemical impedance spectroscopy. *Electrochimica acta*, 40(15):2511–2517, 1995.

[48] JJ Giner-Sanz, EM Ortega, and V Pérez-Herranz. Optimization of the perturbation amplitude for impedance measurements in a commercial pem fuel cell using total harmonic distortion. *Fuel Cells*, 16(4):469–479, 2016.

[49] N Wagner and E Gülzow. Change of electrochemical impedance spectra (eis) with time during co-poisoning of the pt-anode in a membrane fuel cell. *Journal of Power Sources*, 127(1-2):341–347, 2004.

[50] B Sanchez, E Louarroudi, E Jorge, J Cinca, R Bragos, and R Pintelon. A new measuring and identification approach for time-varying bioimpedance using multisine electrical impedance spectroscopy. *Physiological measurement*, 34(3):339, 2013.

[51] Chris de Beer, Paul S Barendse, and Pragasen Pillay. Fuel cell condition monitoring using optimized broadband impedance spectroscopy. *IEEE Transactions on Industrial Electronics*, 62(8):5306–5316, 2015.

[52] S Chechirlian, P Eichner, M Keddam, H Takenouti, and H Mazille. A specific aspect of impedance measurements in low conductivity media. artefacts and their interpretations. *Electrochimica Acta*, 35(7):1125–1131, 1990.

[53] Yuan Xiao-Zi, Song Chaojie, Wang Haijiang, and Zhang Jiujun. *Electrochemical Impedance Spectroscopy in PEM Fuel Cells*. Springer, 2010.

[54] Mirna Urquidi-Macdonald, Silvia Real, and Digby D Macdonald. Applications of kramers—kronig transforms in the analysis of electrochemical impedance data—iii. stability and linearity. *Electrochimica Acta*, 35(10):1559–1566, 1990.

[55] Parthasarathy M Gomadam and John W Weidner. Analysis of electrochemical impedance spectroscopy in proton exchange membrane fuel cells. *International Journal of Energy Research*, 29(12):1133–1151, 2005.

[56] Aparna M Dhirde, Nilesh V Dale, Hossein Salehfar, Michael D Mann, and Tae-Hee Han. Equivalent electric circuit modeling and performance analysis of a pem fuel cell stack using impedance spectroscopy. *IEEE transactions on energy conversion*, 25(3):778–786, 2010.

[57] Jiujun Zhang. *Electrochemical impedance spectroscopy in PEM fuel cells*. Springer, 2009.

[58] Ivan Pivac, Boris Šimić, and Frano Barbir. Experimental diagnostics and modeling of inductive phenomena at low frequencies in impedance spectra of proton exchange membrane fuel cells. *Journal of Power Sources*, 365:240–248, 2017.

[59] Kazimierz Darowicki and Lukasz Gawel. Impedance measurement and selection of electrochemical equivalent circuit of a working pem fuel cell cathode. *Electrocatalysis*, 8(3):235–244, 2017.

[60] Abraham Gebregergis, Pragasen Pillay, and Raghunathan Rengaswemy. Pemfc fault diagnosis, modeling, and mitigation. In *Industry Applications Society Annual Meeting, 2008. IAS'08. IEEE*, pages 1–8. IEEE, 2008.

[61] Abdullah Azher Al-Obaidi and Mahmoud Meribout. A new enhanced howland voltage controlled current source circuit for eit applications. In *GCC Conference and Exhibition (GCC), 2011 IEEE*, pages 327–330. IEEE, 2011.

[62] Dhouha Bouchaala, Qinghai Shi, Xinyue Chen, Olfa Kanoun, and Nabil Derbel. A high accuracy voltage controlled current source for handheld bioimpedance measurement. In *Systems, Signals & Devices (SSD), 2013 10th International Multi-Conference on*, pages 1–4. IEEE, 2013.

[63] Ulrich Tietze, Christoph Schenk, and Eberhard Gamm. *Electronic circuits: handbook for design and application*. Springer, 2015.

[64] Simon Bramble and Gabino Alonso. Loop gain and its effect on analog control systems. Application note, Linear Technology, January 2015.

[65] MATLAB. *version 79.2.0.538062 (R2017a)*. The MathWorks Inc., Natick, Massachusetts, 2017.

[66] Jim Karki. Active low-pass filter design. *Texas Instruments Application Report*, 2000.

[67] Hao Peng, Aleksandar Prodic, Eduard Alarcón, and Dragan Maksimovic. Modeling of quantization effects in digitally controlled dc–dc converters. *IEEE Transactions on power electronics*, 22(1):208–215, 2007.

[68] Shimul Kumar Dam and Vinod John. High-resolution converter for battery impedance spectroscopy. *IEEE Transactions on Industry Applications*, 54(2):1502–1512, 2018.

[69] Brian Bullecks, Resmi Suresh, and Raghunathan Rengaswamy. Rapid impedance measurement using chirp signals for electrochemical system analysis. *Computers & Chemical Engineering*, 106:421–436, 2017.

[70] B Sanchez, Gerd Vandersteen, R Bragos, and Johan Schoukens. Basics of broadband impedance spectroscopy measurements using periodic excitations. *Measurement Science and Technology*, 23(10):105501, 2012.

[71] Kazimierz Darowicki. Linearization in impedance measurements. *Electrochimica acta*, 42(12):1781–1788, 1997.

[72] B Sanchez, G Vandersteen, R Bragos, and J Schoukens. Optimal multisine excitation design for broadband electrical impedance spectroscopy. *Measurement Science and Technology*, 22(11):115601, 2011.

[73] Godfrey Harold Hardy and Edward Maitland Wright. *An introduction to the theory of numbers*. Oxford university press, 1979.

[74] ERDŐS PÁL. Számelméleti megjegyzések iv. *Amer. Math. Monthly*, 65:47, 1958.

[75] David Rees and Douglas L Jones. Design and application of non-binary low peak factor signals for system dynamic measurement. In *Control 1991. Control'91., International Conference on*, pages 644–650. IET, 1991.

[76] Manfred Schroeder. Synthesis of low-peak-factor signals and binary sequences with low autocorrelation (corresp.). *IEEE Transactions on Information Theory*, 16(1):85–89, 1970.

[77] Stephen Boyd. Multitone signals with low crest factor. *IEEE transactions on circuits and systems*, 33(10):1018–1022, 1986.

[78] Andrew Horner and James Beauchamp. A genetic algorithm-based method for synthesis of low peak amplitude signals. *The Journal of the Acoustical Society of America*, 99(1):433–443, 1996.

[79] Alfred Waligo and Paul Barendse. A comparison of the different broadband impedance measurement techniques for lithium-ion batteries. In *Energy Conversion Congress and Exposition (ECCE), 2016 IEEE*, pages 1–7. IEEE, 2016.

[80] Brian Bullecks. *Rapid fault detection and mitigation strategies in the low temperature polymer electrolyte membrane fuel cell*. PhD thesis, 2013.

[81] Aslak Grinsted, John C Moore, and Svetlana Jevrejeva. Application of the cross wavelet transform and wavelet coherence to geophysical time series. *Nonlinear processes in geophysics*, 11(5/6):561–566, 2004.

[82] Stéphane Mallat. *A wavelet tour of signal processing*. Academic press, 1999.

[83] Christopher Torrence and Gilbert P Compo. A practical guide to wavelet analysis. *Bulletin of the American Meteorological society*, 79(1):61–78, 1998.

[84] Fabusuyi A Aroge and Paul Barendse. Signal injection by active load modulation for pem fuel cell diagnostics. In *Power Africa, 2018 IEEE*. IEEE, 2018.

Appendix A

A.1 Loop Response Simulation and Analysis

The control stage of the active load was simulated in a SPICE environment. The circuit configuration is as shown Fig. A.1;

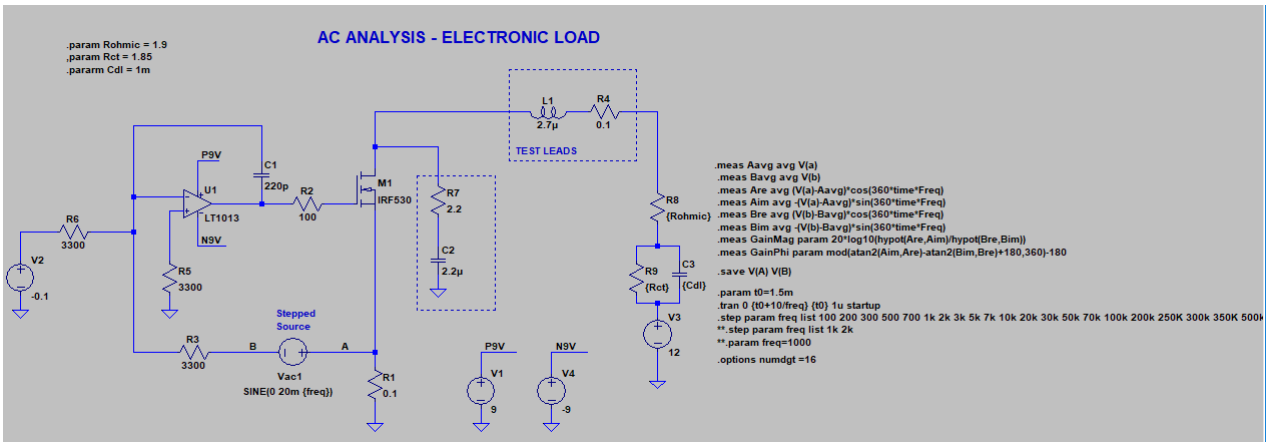

Fig. A.1: SPICE schematic implementing the loop response determination using the signal injection method.

A voltage source is included in the feedback path. The source is made to perform a frequency sweep within the range of interest while the voltage at the terminals are read. The gain and phase is calculated for each of the frequency perturbation to derive the frequency response shown in Fig. 5.9.

The overall circuit is as shown in Fig. A.2.

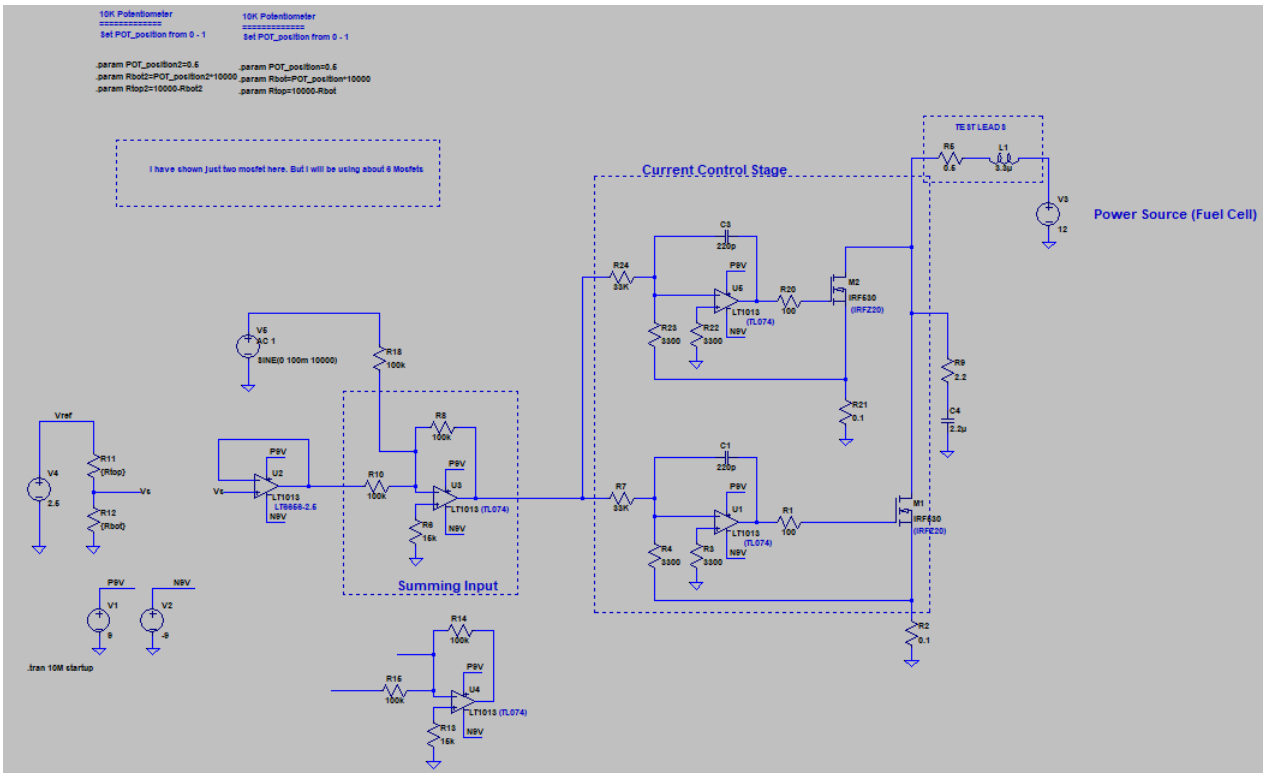

Fig. A.2: SPICE schematic for the key parts of the active load design.

It consists majorly of a summing and MOSFET current control stage. The summing stage consists of the DC and sinusoidal signals which serve as control signal to the control circuitry. The Control circuitry is a PI control (2 shown in parallel here) that helps to control the current by switching the MOSFET appropriately.

A.2 Control Circuitry

From op-amp theory,

$$v_0 = A(v^+ - v^-)$$

from the Fig. 5.6; $v_0 = 0$, therefore the above reduces to;

$$v_0 = -Av^- \tag{A.1}$$

Also from the circuit,

$$\frac{v_i - v^-}{R_1} = \frac{v^- - v_0}{Z_f}$$

where Z_f is $R_f \| C_f$. This Results in;

$$v^- = \frac{v_{in} Z_f + v_0 R_1}{R_1 + Z_f}$$

substituting for v^- as in (A.1);

$$v_0 = -\frac{A(v_{in} Z_f + v_0 R_1)}{R_1 + Z_f}$$

$$\frac{v_0}{v_{in}} = -\frac{AZ_f}{R_1 + Z_f + AR_1}$$

since $A \gg R_1 + Z_f$, the above reduces to;

$$\approx -\frac{Z_f}{R_1}$$

but Z_f is;

$$= \frac{R_f}{R_f S C_f + 1}$$

which implies:

$$\frac{v_0}{v_{in}} = \frac{\frac{R_f}{R_f S C_f + 1}}{R_i}$$

At low frequencies, $S = j\omega \to 0$, therefore;

$$\frac{v_0}{v_{in}} \approx -\frac{R_f}{R_1}$$

A.3 Code Snippets

A.3.1 Crest-Factor Optimisation

```
function err = simple_fitness( x, freq_array, amp, Fs,
    period, n_period )

```

```
%opt = stepDataOptions('InputOffset',0, 'StepAmplitude',1);

[~, y] = draw_multisine_(freq_array,x,amp,Fs,period,n_period);
err = reshape(peak2rms(y, 2), [], 1);
end

function [ t, y ] = draw_multisine( freqs, phases, amp, sampling_freq,...
    period, n_period )

% convenience in case I have to change the frequency
% so I don't have to change the phase too

if isempty(phases)
    phases = zeros(1, length(freqs));
end

t = 0:1/sampling_freq:n_period*period;
y = sum(amp*sin(2 * pi * freqs' * t + phases(1:length(freqs))'), 1);

end

objective = @(x)simple_fitness(x, freq_array, amp, Fs, period, n_period);
nvars = length(freq_array);
lb = zeros(1, nvars) - pi*2;
ub = zeros(1, nvars) + pi*2;
opts = optimoptions(@ga,'PlotFcn',{@gaplotbestf, @gaplotstopping});
opts = optimoptions(opts,'UseVectorized',true);

n = 1;
err = zeros(n,1);
pred = zeros(n, length(freq_array));
for i = 1:n
    [x,fval] = ga(objective, nvars, [], [], [], [], lb, ub,[], opts);
    pred(i, :) = x;
    err(i, 1) = fval;
end
```

A.3.2 Single-Sine Impedance Implementation

```
function [z_mag, z_ph, z_re, z_im, thd_v, ...
    thd_i, freq_array, v_mag, i_mag] = get_imp(volt, curr, freq,...
                                                Fs, n_period)

% This function returns the complex impedance from voltage and current
% input
% volt:     voltage signal in time domain
```

```
8  % curr:      current signal in time domain
9  % freq:      frequency of the signals
10 % FS:        sampling frequecny for clocking calculation
11 % the impedance type may be specified as an optional
       argument
12
13 %% imp_type = 'nyq';   % sets the default data type
       generated to nyquist
14 %%
15 %% if nargin > 3, imp_type = varargin{1}; end
16
17 % clean and orient input data
18 if size(volt, 2) > 1
19     volt = volt';   % make column vector
20 end
21
22 if size(curr, 2) > 1
23     curr = curr';   % make column vector
24 end
25
26 % remove DC component from signal
27 volt = volt - mean(volt);
28 curr = curr - mean(curr);
29
30 t_period = 1/freq; % signal period
31 n_samp_period = t_period*Fs; % sample period of signal (
       samples in one period)
32 %N = 3 * n_samp_period; % this is confusing and redundant
       here
33 %N = int64(n_samp_period*n_period);
34 N = n_samp_period * n_period;
35 n = double(N); % maybe not needed
36 % get signal length
37 %% N = length(volt);
38
39 % fft of signals
40 % todo vectorize as in https://www.mathworks.com/help/matlab
       /ref/fft.html
41 v_fft = fft(volt, N);
42 i_fft = fft(curr, N);
43
44 % Frequency Mapping for first half of signal
45 freq_array = Fs * (0:(N/2))/N;
46 %[~, freq_indx] = find(freq_array == freq);   % index of req
       'd freq in array
47 %[~, freq_ind_v] = max(abs(v_fft));
48 %[~, freq_ind_c] = max(abs(i_fft));
49 %% special arrangement for bode plot
50
51 % Getting the magnitudes
52 v_mag = abs(v_fft/n);
53 i_mag = abs(i_fft/n);
54
55 % fft rituals
56 v_mag = v_mag(1: N/2+1); % taking the necessary half
57 i_mag = i_mag(1: N/2+1);
58
```

```
59 v_mag(2:end-1) = 2 * v_mag(2:end-1);     % adding up the
       mirrored magnitudes
60 i_mag(2:end-1) = 2 * i_mag(2:end-1);
61
62 figure(3)
63 Fs
64 N
65 freq_array(1:10)
66 plot(freq_array, v_mag);
67
68 figure(4)
69 plot(freq_array, i_mag);
70 %% select the required frequency
71
72 v_resp = v_mag(n_period+1);
73 i_resp = i_mag(n_period+1);
74
75 v_ph = angle(v_fft(n_period+1));
76 i_ph = angle(i_fft(n_period+1));
77
78 %% output results
79
80 % for bode
81 z_mag = v_resp/i_resp;
82 z_ph = (180/pi) * (v_ph - i_ph);
83 z_ph = 180 - z_ph; %new correction
84
85 % for nyquist
86 %[z_re, z_im] = pol2cart((z_ph * pi/180), z_mag);
87
88 imp_cmplx = v_fft(n_period+1)/(i_fft(n_period+1));
89 z_re = -real(imp_cmplx); % the impedance gotten is negative
       (already)
90 z_im = imag(imp_cmplx);
91
92 %% thd
93 harm_freq_indx = 1:n_period:N/2+1; % indices of DC (1) and
       harmonics
94 harm_freq_indx = int32(harm_freq_indx);
95 v_freqs = v_mag(harm_freq_indx);        % gets the harmonic
       values
96 v_fund = v_freqs(2);                    % the fundamental comes
       out in the first harmonic after dc since that is the
       resolution from calc
97 v_harm = v_freqs(3:5);
98
99 thd_v = 100 * sqrt(sum(v_harm.^2))/v_fund;
100
101 i_freqs = i_mag(harm_freq_indx);        % gets the harmonic
       values
102 i_fund = i_freqs(2);
103 i_harm = i_freqs(3:5);
104
105 thd_i = 100 * sqrt(sum(i_harm.^2))/i_fund;
106
107 end
```

A.3.3 Signal Acquisition and Realisation

```
function [ imp_data ] = imp_spec(freqs, ampl, samples,
    n_period)
%This function takes in a list of frequency as arguments
% frequency:    a list of frequencies to be generated
% samples:  the number of samples for a period of the signal
     (granularity)
% n_period: the number of periods to be generated (hence
    also acquired)

% to do
n_freq = length(freqs);

%% initialize output
imp_data = zeros(n_freq, 5);
thd_data = zeros(n_freq, 3);
volt_data = zeros(samples * n_period, n_freq);
curr_data = zeros(samples * n_period, n_freq);
volt_mag_data = zeros(samples*n_period/2+1, n_freq);
curr_mag_data = zeros(samples*n_period/2+1, n_freq);

freq_array_data = zeros(samples*n_period/2+1, n_freq);
%%
for i = 1:n_freq

    freq = freqs(i);
    data = ampl*sin(linspace(0, 2*pi, samples+1))';
    data(end) = [];     % remove the last point to terminate
        period

    %% daq setup

    s = daq.createSession('ni');
    dev = daq.getDevices().ID;
    addAnalogOutputChannel(s, dev, 'ao0','Voltage');
    addAnalogInputChannel(s, dev, 'ai0', 'Voltage');
    addAnalogInputChannel(s, dev, 'ai1', 'Voltage'); %
       current
    s.Rate = freq * samples;    % gets the required rate for
        a given freq
    %Fs = s.Rate;
    %todo uncomment below and clear above
    Fs = freq * samples;
    queueOutputData(s, repmat(data, n_period, 1));    %
       queue n_periods of data

    % start activity
    dt_out = s.startForeground();
    size(dt_out);

    figure(1)
    plot(dt_out(1:end, 1))

    figure(2)
    plot(dt_out(1:end, 2))
    %% calulate impedance
```

```
49
50      [z_mag, z_ph, z_re, z_im, ...
51          thd_v, thd_i, freq_array, v_mag, i_mag] = get_imp(
                dt_out(1:end, 1), ...
52                                                  dt_out(1:end, 2),
                                                        ...
53                                                  freq, Fs, n_period)
                                                        ;
54
55      imp_data(i, 1:end) = [freq, z_mag, z_ph, z_re, z_im];
56      thd_data(i, 1:end) = [freq, thd_v, thd_i];
57
58      volt_data(1:end, i) = dt_out(:, 1);
59      curr_data(1:end, i) = dt_out(:, 2);
60
61      volt_mag_data(1:end, i) = v_mag';
62      curr_mag_data(1:end, i) = i_mag';
63
64      freq_array_data(1:end, i) = freq_array';
65      % pause iteration
66      %pause(10);
67  end
68  % write impedance to csv
69  time = datestr(datetime);
70  time = strrep(time, ':', '-');
71  filename = strcat(time, string(-ampl), string(-n_period), '.
        csv');
72  csvwrite(filename, imp_data);
```

A.3.4 Non-linearity Test

```
1   def non_lin_sys(sig_input, rms_noise=0.1, poly_coeff=[25e-3,
        1, 6e-1, -1e-3, 5e-6, 1e-5]):
2       """weakly non-linear system takes in sig_input signal
        and returns an output signal"""
3
4
5
6       order = len(poly_coeff) - 1  # minus DC point
7       sig_input_length = len(sig_input)
8
9       noise_sig_input = rms_noise * rng.normal(loc=0, scale=1,
            size=sig_input_length)
10      noisy_sig_input = sig_input + noise_sig_input
11
12      #poly_coeff.reverse()  # very problematic
13      output = np.polyval(poly_coeff[::-1], noisy_sig_input)
14
15      return output
```